NASA CR - 134755

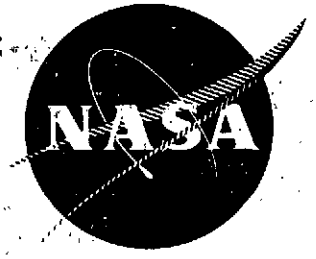

# 15 CM DIAMETER ION THRUSTER RESEARCH

PREPARED FOR
LEWIS RESEARCH CENTER
NATIONAL AERONAUTICS AND SPACE ADMINISTRATION

GRANT NGR-06-002-112




Annual Report
December 1974

Paul J. Wilbur
Department of Mechanical Engineering
Colorado State University
Fort Collins, Colorado

| 1. Report No. | 2. Government Accession No. | 3. Recipient's Catalog No. |
|---|---|---|
| NASA CR-134755 | | |

| 4. Title and Subtitle | 5. Report Date |
|---|---|
| 15 cm Diameter Ion Thruster Research | December 1974 |
| | 6. Performing Organization Code |

| 7. Author(s) | 8. Performing Organization Report No. |
|---|---|
| Paul J. Wilbur | |
| | 10. Work Unit No. |

| 9. Performing Organization Name and Address | 11. Contract or Grant No. |
|---|---|
| Department of Mechanical Engineering<br>Colorado State University<br>Fort Collins, Colorado 80523 | NGR-06-002-112 |
| | 13. Type of Report and Period Covered<br>Contractor Report<br>Dec. 1, 1973 - Dec. 1, 1974 |
| 12. Sponsoring Agency Name and Address | 14. Sponsoring Agency Code |
| National Aeronautics and Space Administration<br>Washington, D. C. 20546 | |

15. Supplementary Notes

Grant Monitor, William Kerslake
Spacecraft Technology Div.
NASA Lewis Research Center
Cleveland, Ohio 44135

16. Abstract

The startup reliability of a 15 cm diam. mercury bombardment ion thruster which employes a pulsed high voltage tickler electrode on both the main and neutralizer cathodes is examined. Startup of the thruster is achieved in five or fewer attempts 100% of the time on the main cathode and 98.7% of the time on the neutralizer cathode over a 3640 cycle test. Cold thruster startup tests which demonstrate that a 15 cm diam. thruster can be started from a 20°C initial condition in less than 4 minutes are discussed. Tests in which this thruster started from a cold condition, operated for an hour at a 600 mA beam current and then shut down are discussed and the thruster is observed to achieve an energy efficiency of about 75% and a propellant utilization efficiency of about 77% over the complete cycle. The effect of single cusp magnetic field thruster length on its performance is discussed and results which show an ion beam flatness parameter of 0.9 at the grids of this thruster are presented. Several guidelines for the shaping of magnetic field lines in thrusters are formulated from test results obtained with this thruster. A model describing double ion production in mercury discharges is presented and the dominant production route is shown to occur through the single ionic ground state. Photographs of the interior of an operating hollow cathode are presented and they show a cathode spot is present if the cathode is free of low work-function surfaces and that the spot is not observed if a low work-function oxide coating is applied to the cathode insert. A test which suggests low work-function oxide coatings tend to migrate during thruster operation is discussed.

| 17. Key Words (Suggested by Author(s)) | 18. Distribution Statement |
|---|---|
| Electrostatic Thruster | Unclassified - Unlimited |

| 19. Security Classif. (of this report) | 20. Security Classif. (of this page) | 21. No. of Pages | 22. Price* |
|---|---|---|---|
| Unclassified | Unclassified | 96 | $3.00 |

* For sale by the National Technical Information Service, Springfield, Virginia 22151

TABLE OF CONTENTS

# PULSED IGNITION STARTUP STUDIES

## Introduction

Appreciable cost or weight savings can be achieved in synchronous orbit satellite systems if ion thrusters are used to produce the associated North-South stationkeeping requirement instead of a chemical propellant thruster[1]. For a typical synchronous communication satellite having a mass of 700 kg, the 46 m/sec annual North-South stationkeeping velocity increment can be met by a mercury ion thruster operating at a 600 mA beam current level and 1000 volt thruster potential on a duty cycle of 230 hours per year. Assuming 60% overall electrical efficiency, the thruster could satisfy this requirement by operating for 230 one hour intervals from a 1 kilowatt-hour battery which could be charged continuously from a small solar array ($\sim$ 30 watt output). For such a thruster system to perform effectively however it must be capable of repeated startup which is both rapid and reliable and be able to produce a 600 mA ion beam at 1000 volts thruster potential with acceptable propellant utilization and electrical efficiencies. Electron bombardment ion thruster startup has required resistance heating of the hollow cathode tip to a sufficiently high temperature to permit spontaneous ignition of the keeper discharge. This mode of startup is frequently unreliable because the cathode tip temperatures and the times which are required to start the discharge tend to vary with the history of the cathode. Wintucky[2] has demonstrated that cathodes can be started using a high voltage discharge between a tickler electrode and the cathode to produce sufficient electrons to facilitate an arc discharge between a thruster cathode and keeper. Subsequent testing[3,4] has shown that rapid, reliable startup can be achieved utilizing this concept without propellant overflow or high cathode tip temperatures.

A 15 cm diameter mercury bombardment thruster with a dished grid system was equipped with tickler electrodes to initiate both the main and neutralizer cathode discharges. The ticklers are 1 mm dia, 1% thoriated tungsten wires sharpened to points and installed with their axes 0.5 mm from and parallel to the faces of the cathodes. The thruster and high voltage ignition system are described in more detail in Reference 4.

Repetitive Startup Cycle Tests

In order to demonstrate the suitability of the thruster and ignition system to the type of operation that might be encountered on a ten year mission in the periodic mode of operation (e.g. one hour/day) an accelerated test of the effect of startup and shutdown cycles on the system was conducted. New cathodes, which contained rolled 0.01 mm thick tantalum foil inserts that had been dipped into chemical R-500 prior to insertion into the cathode tube, were used in this test. The test involved establishment of the main, cathode and neutralizer flow rates at approximately 700 mA, 30 mA and 40 mA respectively. The main and neutralizer tip temperatures were raised to 500°C and 750°C respectively and the main and neutralizer keeper potentials were set at approximately 200 V. The arc power supply was adjusted to limit the arc current to about 4 A. The subsequent events, shown graphically in Figure 1, included initiation of the neutralizer discharge using spark ignition, adjustment of neutralizer keeper current to 0.2 A, spark initiation of the main keeper and arc discharges, adjustment of the main keeper current to a 0.3 A, and application of the high voltages (+1 kV, -.5 kV) to the thruster grids. After data had been recorded, the high voltage, arc, keeper and neutralizer keeper power supplies were turned off and the main and neutralizer cathodes were allowed to cool to near 500°C and 750°C respectively before the startup sequence was repeated. This procedure was repeated until 3640 startup - shutdown cycles had been completed. The test required several days of operation and removal of the thruster from the vacuum chamber on several occasions to correct problems. The startup reliabilities over the 3640 cycle test were as follows:

Table I

Ignition Frequency in "n" Attempts

| Number of high Voltage Sparks Required for Ignition ("n") | 1 | 2 | 3 | 4 | 5 | >5 |
|---|---|---|---|---|---|---|
| Main Cathode | 98.4% | 1.3% | 0.2% | 0.1% | 0 | 0 |
| Neutralizer Cathode | 89.9% | 5.7% | 1.8% | 0.8% | 0.5% | 1.3% |

These data suggest a high reliability for startup of the main cathode discharge and a lower reliability for the neutralizer cathode discharge startup. This tendency is also reflected in Figure 2 which shows the frequency at

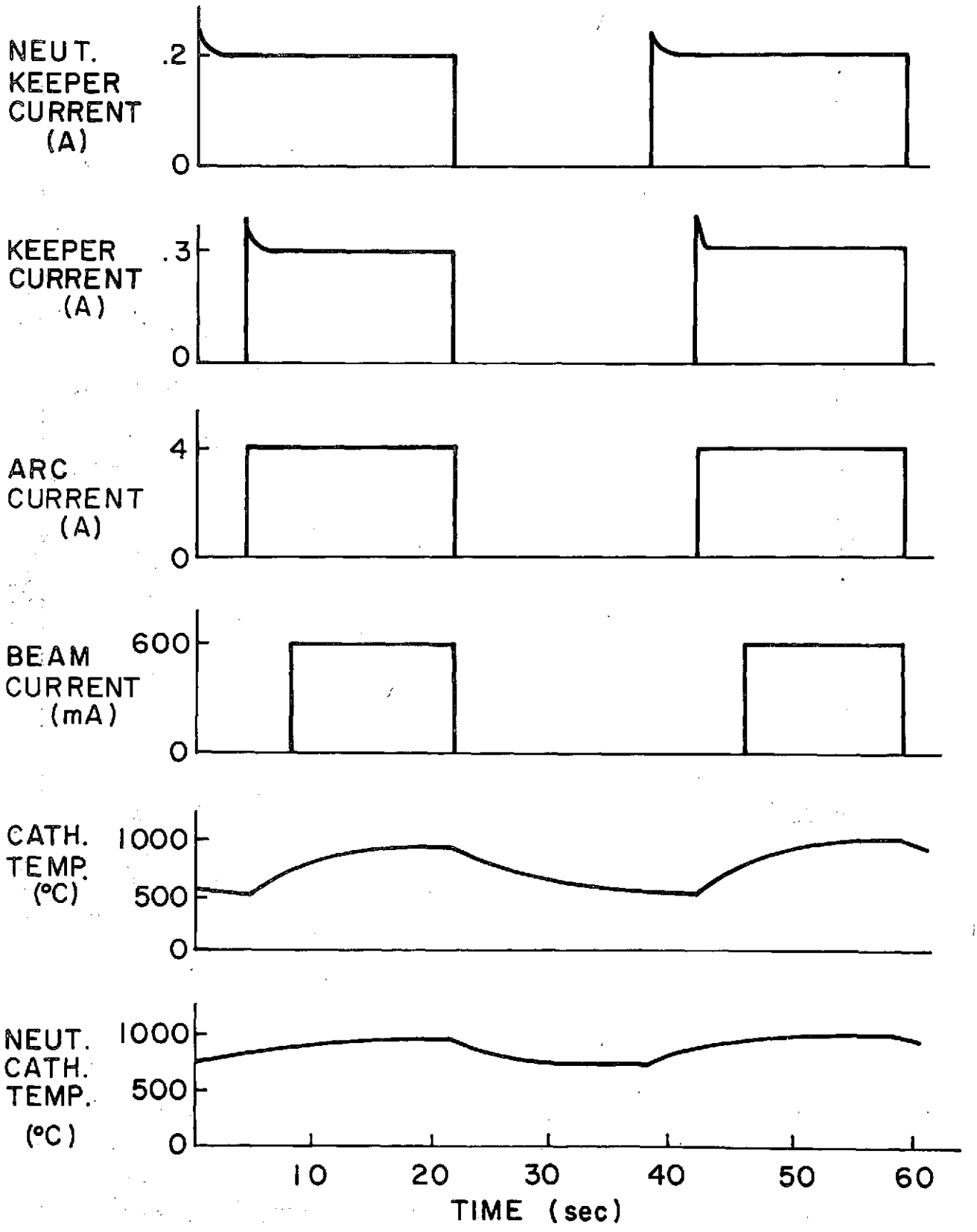


STARTUP - SHUTDOWN TEST SEQUENCE (Typ.)

FIGURE 1

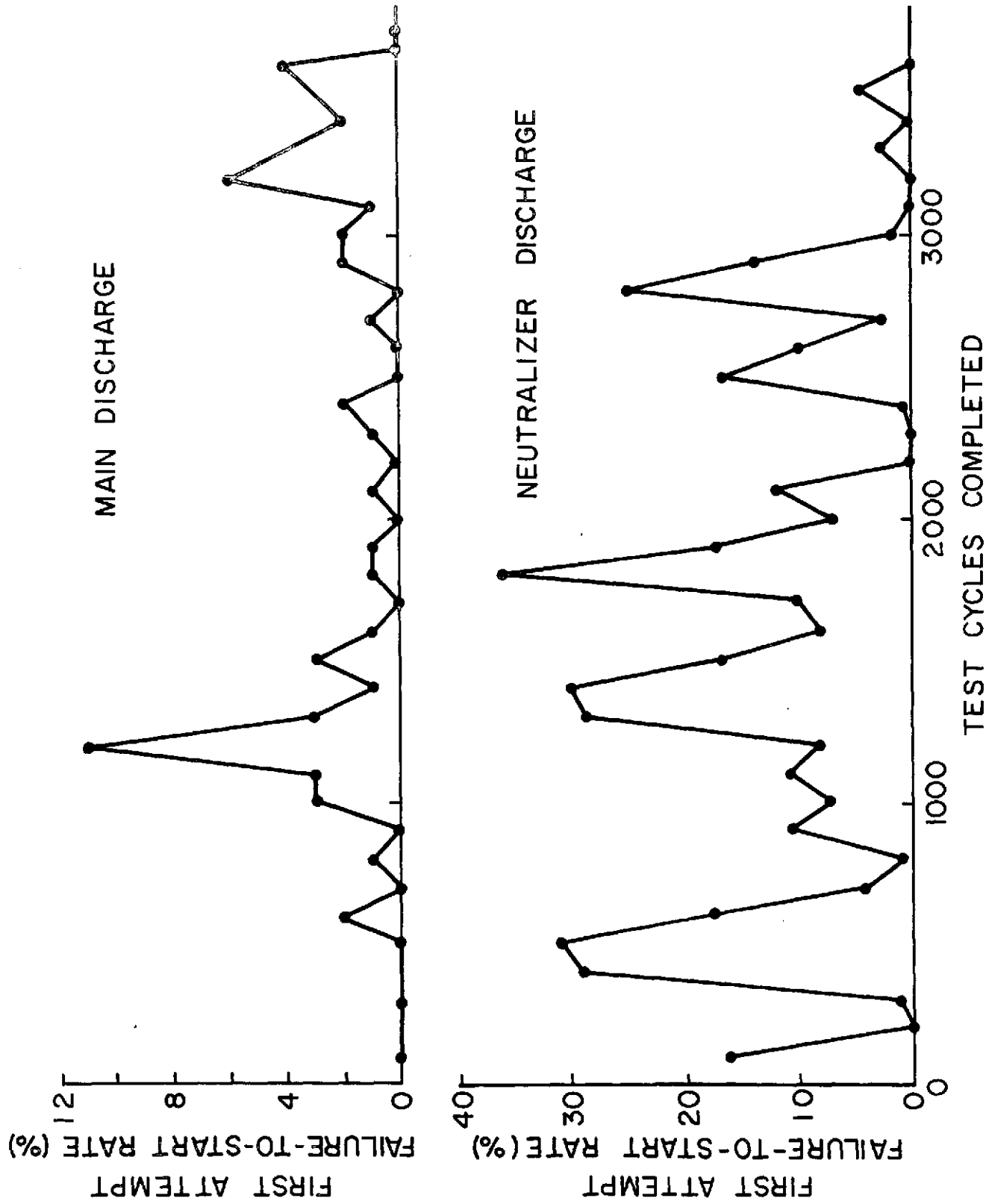


FIRST ATTEMPT FAILURE-TO-START HISTORY

FIGURE 2

which more than one actuation of the startup circuitry was required to initiate the main and neutralizer discharges as a function of the number of test cycles that had been completed. No particular trend is apparent from Figure 2.

Some of the reasons for the lower startup reliability of the neutralizer discharge can be understood by considering Figure 3, which shows the frequency of neutralizer discharge initiation failure as a function of cycles completed. Failure was said to occur when a discharge could not be initiated in five attempts and the test was terminated temporarily until the probable cause of the failure was found and corrected. The cause of the failures which were identified and any corrective action taken are indicated on Figure 3. The failures associated with the battery and sparking are not considered significant as the battery would be replaced by a power supply in the final design and sparking was eliminated by providing adequate insulation for the tickler at all locations except the immediate vicinity of the cathode tip. The increase in failure-to-start rate which can be seen in Figure 3 at about 2500 cycles could not be corrected by component replacements and it was not due to breakdown away from the cathode tip. The spark was in fact observed at the neutralizer cathode with each actuation, but the discharge would not start. This condition was corrected temporarily by increasing the neutralizer tip temperature (from 750°C to 800°C) and then by increasing the neutralizer flow rate. The increased startup reliability achieved by these measures was temporary and on the 2810$^{th}$ start it became necessary to add chemical R-500 emissive mix to the cathode insert. This made it possible to achieve a high startup reliability at any temperature above 700°C for the remainder of the test. This suggests that a degradation of the cathode insert which had been coated with emissive mix at the start of the tests had occurred. The reason for this degradation is not apparent as the cathode tip temperature was maintained below 1000°C throughout the test so significant R-500 boil-off probably did not occur. It is considered possible however that the low work function emissive mix was depleted from the region of the insert closest to the cathode orifice and additional chemical could not migrate into this region because of the short duration of thruster operation which resulted in a low average temperature of the cathode insert.

A. DIODE FAILURE-REPLACED
B. BATTERY DEAD-REPLACED
C. SPARKING AWAY FROM CATHODE TIP ELIMINATED BREAKDOWN PATH
D. NO APPARENT REASON
E. SPARKING AWAY FROM CATHODE TIP- INSTALLED QUARTZ TUBE NEAR TICKLER TIP
F. SPARKING AWAY FROM CATHODE TIP- INSTALLED KAPTON FILM TO ELIMINATE PATH
G. NO APPARENT REASON - INCREASED NEUT. TIP TEMP. TO 800° C AND FLOW RATE TO ~ 50 ma - REWELDED NEUT. INSERT.
H. NO APPARENT REASON - ADDED R-500 TO INSERT- REDUCED TIP TEMP. AND FLOW RATE

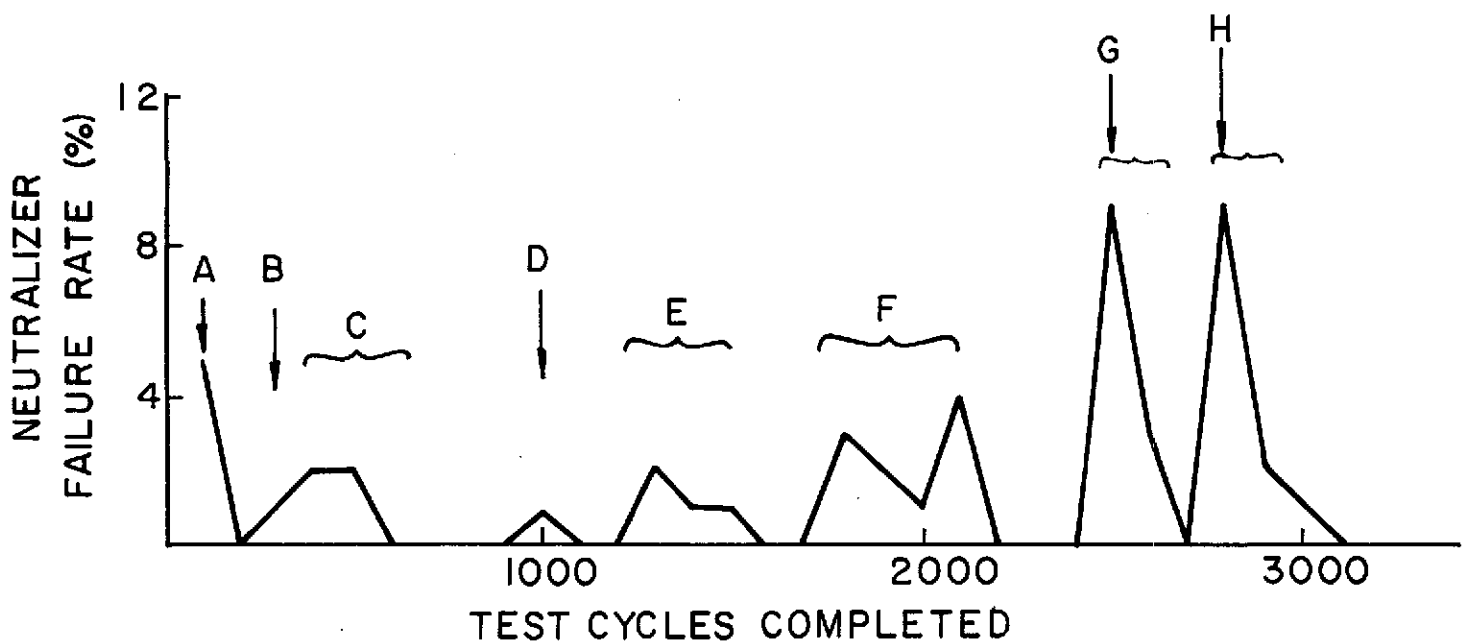


NEUTRALIZER FAILURE-TO-START HISTORY

FIGURE 3

No significant erosion of either cathode was observed during the test. This is illustrated by Figure 4 which shows the condition of each cathode, tickler and keeper before and after the test. The small wires attached to each cathode are thermocouples. The photograph of the neutralizer assembly after the test shows the insulating tube which had to be placed around the tickler to prevent electrical breakdown to points away from the cathode tip.

Rapid Startup and Operation from Ambient Temperatures

If a thruster is to be operated cyclically with a duty cycle of one hour in every twenty-four it is desirable to minimize parasitic energy and neutral propellant losses which could be significant during the startup phase of the thruster operating cycle. The startup times for hollow cathode discharges in ground tests have been somewhat unpredictable but they appear to depend on such events as the frequency of cathode exposure to air and its temperature at the time when it was exposed. Although startup times tend to be more rapid and reliable in space tests[5] than they have been in ground tests, it is desirable to determine what can be done to shorten startup times as well as the power and propellant loss penalties associated with this type of operation. In order to evaluate the magnitudes of the losses a series of tests were run in which a 15 cm diam. mercury ion thruster was started as rapidly as possible from a cold condition, then operated for one hour before power was cut to the vaporizer heaters and the thruster discharge went out. Fifteen such tests were conducted using a SERT II thruster equipped with dished grids and independent main and cathode vaporizers as described in Reference 4. In the first ten of these tests main, cathode and neutralizer vaporizers, the mock isolator heater and the main and neutralizer cathode heaters were all energized simultaneously. When the vaporizer temperatures reached values corresponding to the desired flow rates, keeper and arc voltages were raised to about 225 V and 50 V respectively and the spark ignition system was used to start first the neutralizer and then the main discharge. After the main keeper, neutralizer keeper and arc currents had been adjusted to 0.3 A, 0.2 A, and 4.0 A respectively the high voltages were raised to +1000 V and -500 V. Flow rates were controlled manually by monitoring vaporizer

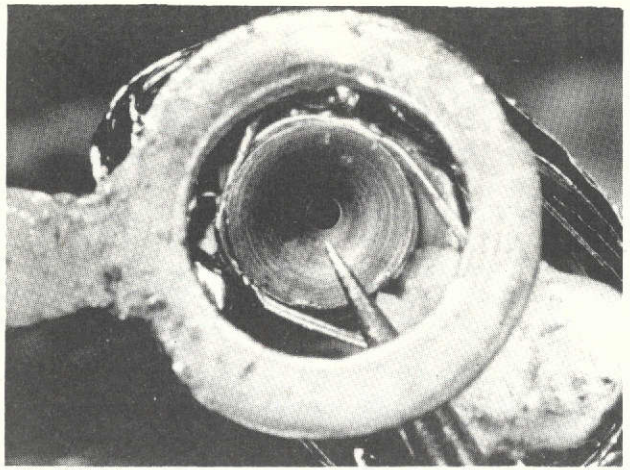

A. PRIOR TO TEST

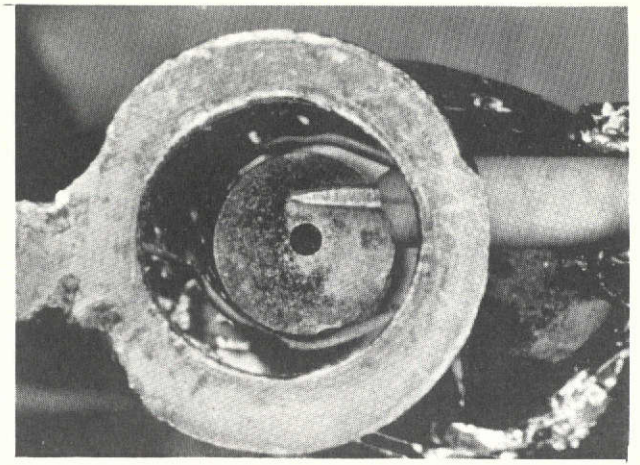

B. AFTER 3640 STARTUP-SHUTDOWN CYCLES

NEUTRALIZER CATHODE ASSEMBLY

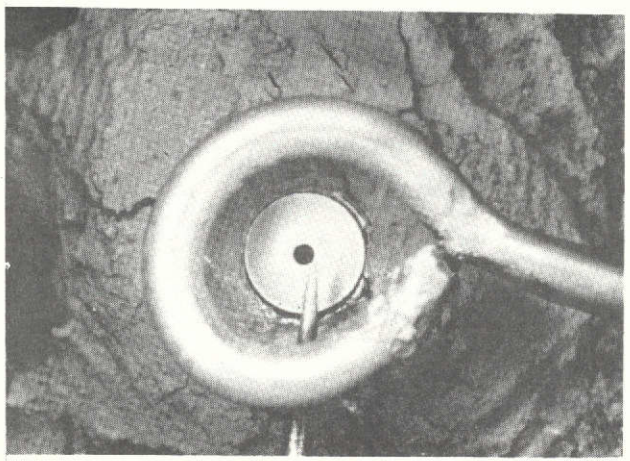

C. PRIOR TO TEST

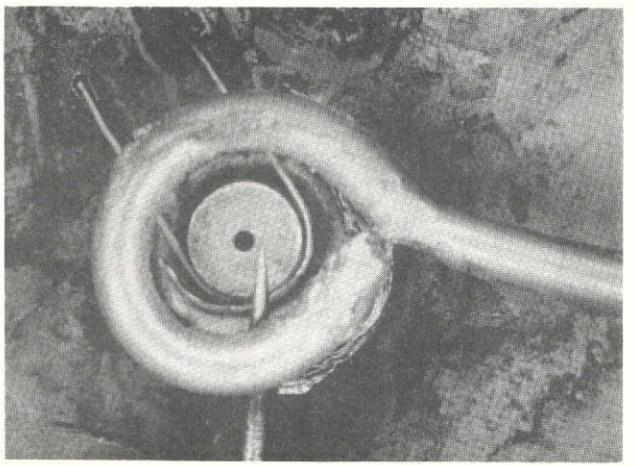

D. AFTER 3640 STARTUP-SHUTDOWN CYCLES

MAIN CATHODE ASSEMBLY

EFFECT OF SPARK IGNITION TEST ON CATHODE COMPONENTS

FIGURE 4

temperatures and in the case of the main flow rate by monitoring thermal flow meter[4] output. Ion beam current remained around 600 mA during the operating period. After one hour of thruster operation the main and cathode vaporizer power was shut off and thruster operation was continued until the arc was extinguished. All power to the thruster was then shut off and it was allowed to cool for at least an hour before the next test was started.

Currents and voltages associated with all heaters and discharges were recorded every three minutes during this test and the energy consumed in each component part of the thruster was subsequently calculated by integrating the component power consumption over the operating time. Neutralizer and cathode propellant consumptions were determined over the operating cycle by measuring the volumes of propellant used. Allowance for thermal contraction and expansion of the mercury was incorporated into these measurements. During these ten tests, propellant consumption through the main vaporizer was determined by integration of the output of the thermal flow meter.

Energy balance data obtained from these test runs are presented in Table II. From these data it is apparent that the major energy losses occur in the arc discharge and vaporizers. The thruster energy efficiency which is the ratio of beam energy to total energy consumed during the test is observed to lie in the range 75 to 76%. The times required to achieve thruster startup are seen to depend on the initial temperature of the thruster. There was a tendency for this time to decrease as experience was acquired operating the thruster in this manner. Propellant mass consumption data although it was recorded from thermal flow meter output is not presented because subsequent experiments showed integrated flow meter output did not agree with volume change measurements.

After several test cycles had been completed it was concluded that propellant was condensing in the lines between the two cathodes and their associated vaporizers and that this was preventing rapid startup of the discharges. For test runs nine and ten a heater was added to heat these sections of line where condensation was suspected and as Table II suggests this did reduce the time required for startup by about one minute. In order to prevent condensation of the main propellant flow stream in the

TABLE II

Energy and Propellant Consumptions for Startup - Operate one hour - Shutdown Tests

15 cm Diam. Thruster - 600 mA Beam Current

| Run | Prop. Mass (coul) | Integ. Beam Current (coul) | Prop. Util. Eff. | Beam Energy (kJ) | Arc Energy (kJ) | Imp. Energy (kJ) | Keeper Energies (Neut & Main) (kJ) | Beam to Neut. Coupling Energy (kJ) | Cathode Heater Energies (Neut & Main) (kJ) | Isolator Heater and Vaporizer Energies (kJoule) | Total Energy (kJoule) | Thruster Energy Eff. | Time To Start (Min.) | Init. Main Vap. Temp (°C) | Preheat |
|---|---|---|---|---|---|---|---|---|---|---|---|---|---|---|---|
| 1 | -- | 2171 | -- | 2171 | 497 | 8 | 23 | 46 | 13 | 119 | 2877 | 75% | 10.5 | 20°C | None |
| 2 | -- | 2055 | -- | 2055 | 501 | 11 | 23 | 42 | 10 | 103 | 2745 | 75% | 7.5 | 90°C | None |
| 3 | -- | 2175 | -- | 2175 | 498 | 8 | 23 | 46 | 9 | 110 | 2870 | 76% | 6.6 | 85°C | None |
| 4 | -- | 2061 | -- | 2061 | 494 | 18 | 22 | 44 | 8 | 109 | 2756 | 75% | 5.9 | 97°C | None |
| 5 | -- | 2097 | -- | 2097 | 510 | 10 | 23 | 45 | 11 | 115 | 2811 | 75% | 9.0 | 20°C | None |
| 6 | -- | 2153 | -- | 2153 | 500 | 10 | 23 | 39 | 8 | 109 | 2842 | 76% | 5.8 | 90°C | None |
| 7 | -- | 2103 | -- | 2103 | 497 | 13 | 23 | 48 | 7 | 108 | 2799 | 75% | 5.4 | 99°C | None |
| 8 | -- | 2202 | -- | 2202 | 504 | 9 | 23 | 45 | 7 | 108 | 2898 | 76% | 5.5 | 98°C | None |
| 9 | -- | 2073 | -- | 2073 | 490 | 13 | 25 | 43 | 13 | 110 | 2767 | 75% | 7.5 | 22°C | None |
| 10 | -- | 2054 | -- | 2054 | 488 | 13 | 25 | 42 | 10 | 110 | 2742 | 75% | 4.7 | 81°C | None |
| 11 | -- | 2120 | -- | 2120 | 487 | 9 | 25 | 43 | 10 | 120 | 2814 | 75% | 4.7 | 82°C | None--Main dist. plenum htr on during operation |
| 12 | -- | 2117 | -- | 2117 | 491 | 9 | 23 | 43 | 13 | 114 | 2810 | 75% | 1.8 | 90°C | Cath tips and main dist. plenum for 6 min. |
| 13 | 2818 | 2217 | 79% | 2217 | 544 | 6 | 24 | 37 | 16 | 117 | 2961 | 76% | 3.8 | 20°C | Cath tips and main dist. plenum for 10 min. |
| 14 | 2378 | 1734 | 73% | 1734 | 528 | 8 | 24 | 28 | 18 | 114 | 2454 | 71% | 1.5 | 20°C | Cath tips and main dist. plenum for 10 min. |
| 15 | 2822 | 2109 | 75% | 2109 | 517 | 5 | 24 | 37 | 14 | 110 | 2816 | 75% | 2.2 | 82°C | Cath tips and main dist. plenum for 6 min. |

main flow distribution plenum a heater was next added to heat it during the startup. This change did not appear to decrease the startup time significantly. It was next decided to preheat the main flow distribution plenum and the region from the main and neutralizer cathode tips to the vaporizers for six minutes prior to energizing the vaporizers. This resulted in more rapid startup (1.8 min) and stabilization of the thruster discharge. None of these additions of heater power resulted in any significant increase in energy consumption.

In order to measure the main propellant consumed during startup for tests eleven through fifteen a pipette was installed which indicated the total volume of mercury consumed during a test cycle. These tests were also conducted differently than the first ten tests in that the cathode tips, sections of feed line between vaporizers and cathodes and the main flow plenum chamber were preheated either six or ten minutes before the vaporizers were energized. This procedure did reduce the time from vaporizer energization to startup significantly as the data of Table II suggest. Propellant utilization efficiencies were calculated as the ratio of integrated beam current to integrated propellant consumption (main, cathode and neutralizer) for these tests and they were found to be 1% to 7% below the steady-state value of 80%. It is interesting to note that the data do not indicate propellant utilizations are higher for short startup times. It appears that flow control during operation has a much greater effect on propellant utilization than does the startup time. In test run fourteen for example, the main and cathode flow rates were inadvertantly controlled low and this resulted in an average beam current below 500 mA and the poorest propellant utilization observed in the tests although the startup time was the shortest observed (1.5 min.).

During tests in which there was no preheat of the feed lines between vaporizers and cathodes and of the main flow plenum, there was a definite mode change in thruster operation which would result in a dramatic increase in the beam current and arc voltage. Figure 5, which shows beam current and arc voltage as a function of time after startup indicates the mode change at 8.5 minutes after startup. The dotted (no preheat) curves in this figure were obtained by averaging beam current and arc voltage data from the first eleven tests runs while the solid curve represents

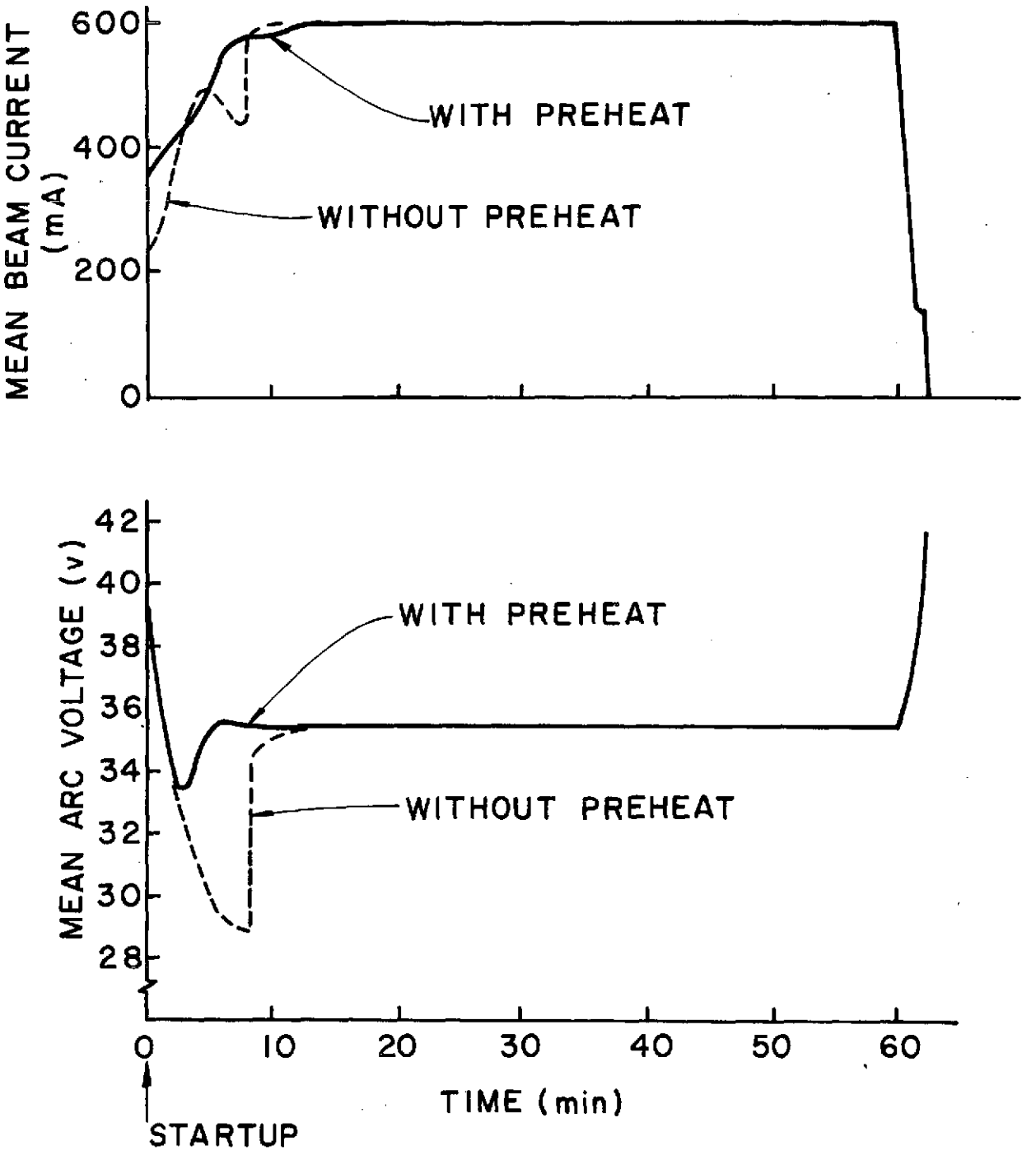


EFFECT OF PREHEAT ON RAPID STARTUP

FIGURE 5

the average of data from runs twelve, thirteen and fifteen which did include preheat. When preheat was applied the transition to the full beam current operating condition was achieved more smoothly and the integrated beam current was increased.

## Conclusions

A high voltage tickler system can be employed to start main and neutralizer discharges at tip temperatures of 500°C and 750°C respectively. The reliability of main cathode startup in five or fewer ignition attempts is 100% while the corresponding neutralizer ignition reliability in five or fewer attempts is 98.7%. Neither cathode showed any significant erosion damage in 3640 startup cycles using a tickler ignition scheme. After about 2500 startup cycles the neutralizer cathode failure-to-start rate began to increase and a low work function mix (R-500) had to be added the cathode insert to achieve acceptable startup reliability.

A modified SERT II (15 cm diam.) thruster can be started from a cold (20°C) initial state in less than four minutes if approximately 10 minutes of preheat is applied to passages that will direct mercury flow into the thruster and through the neutralizer orifice. This preheat also facilitates rapid stabilization of the arc discharge and ion beam current. The overall power efficiency associated with startup, operation for one hour and shutdown is 75 to 76%. The overall propellant utilization efficiency associated with this same cycle appears to be affected less by startup time than by flow control during thruster operation but appears to lie in the range 75% to 79% for this thruster.

# SINGLE CUSP MAGNETIC FIELD THRUSTER

John R. Beattie

## Introduction

The cusped magnetic field discharge chamber geometry has been investigated as a viable approach to achieving a uniform current density in the exhaust beam of an electron-bombardment ion thruster. A highly uniform current density is desirable in order to eliminate localized erosion of the accelerator grid due to charge exchange ion impingement. The charge exchange reaction rate is proportional to the local beam current density and for an accelerator grid of uniform thickness this means the grid will wear through first at the point where the current density is a maximum. For most discharge chambers the point of peak beam current density and maximum wear rate occurs on the thruster centerline.

The importance of achieving a highly uniform beam current density profile can be illustrated mathematically by considering the thrust equation for an electrostatic accelerator. For a given propellant, specific impulse, and thruster diameter the thrust is directly proportional to the average beam current density

$$T \propto J_{ave} \tag{1}$$

where T is the thrust and $J_{ave}$ the average current density. Defining the beam flatness parameter F as the ratio of average to maximum beam current density, the thrust equation can be expressed as

$$T \propto FJ_{max} \tag{2}$$

Assuming the grid lifetime varies inversely as the maximum beam current density then the thrust is seen to be proportional to the beam flatness parameter for a given grid lifetime. Conversely, for a given thrust the grid lifetime is proportional to the flatness parameter.

Experimental studies[6] have shown a high correlation between the beam current density profile existing at the accelerator grid and the ion number density profile existing inside the discharge chamber at the screen

grid. This suggests the beam current density profile can be made more uniform by reducing radial plasma density gradients in the vicinity of the screen grid. The validity of this approach as a means of achieving a highly uniform beam current density profile has been demonstrated by the success of the radial field thruster[7]. This discharge chamber geometry achieved a beam flatness parameter of 0.67 compared to about 0.4 for the SERT II thruster. For comparison the flatness parameter for a cosine distribution is 0.46 while a perfectly uniform profile has a value of 1.0.

The cusped magnetic field concept is based on a neutral residence time criterion which states that the time a neutral atom spends in the ionizing region defined by the critical field line[8] and the accelerator system should be at least as great as the characteristic time for ionization by primary electrons. This approach requires the distance L between the upstream primary electron boundary and the accelerator system satisfy the expression

$$L > \frac{\bar{V}_o}{n_p \sigma_o^+ V_p} \tag{3}$$

where $\bar{V}_o$ is the neutral particle speed, $n_p$ is the primary electron number density, $\sigma_o^+$ is the ionization cross section, and $V_p$ is the speed of the primary electron. Representative values of these quantities for the SERT II discharge chamber are: $n_p = 2 \times 10^{16}$ m$^{-3}$, $\bar{V}_o = 230$ m/sec, $V_p = 3.25 \times 10^6$ m/sec (30 eV), and $\sigma_o^+ = 5 \times 10^{-20}$ m$^2$. Substituting these values into Equation 3 yields a numerical value for the design criterion

$$L > 70 \text{ mm} \quad . \tag{4}$$

For the SERT II divergent field geometry shown in Figure 6A the distance between the critical field line and the screen grid is approximately 8 mm. One would therefore expect a significant neutral loss at the thruster periphery and, as a consequence, a non-uniform ion density profile. One approach to increasing the neutral residence time at the

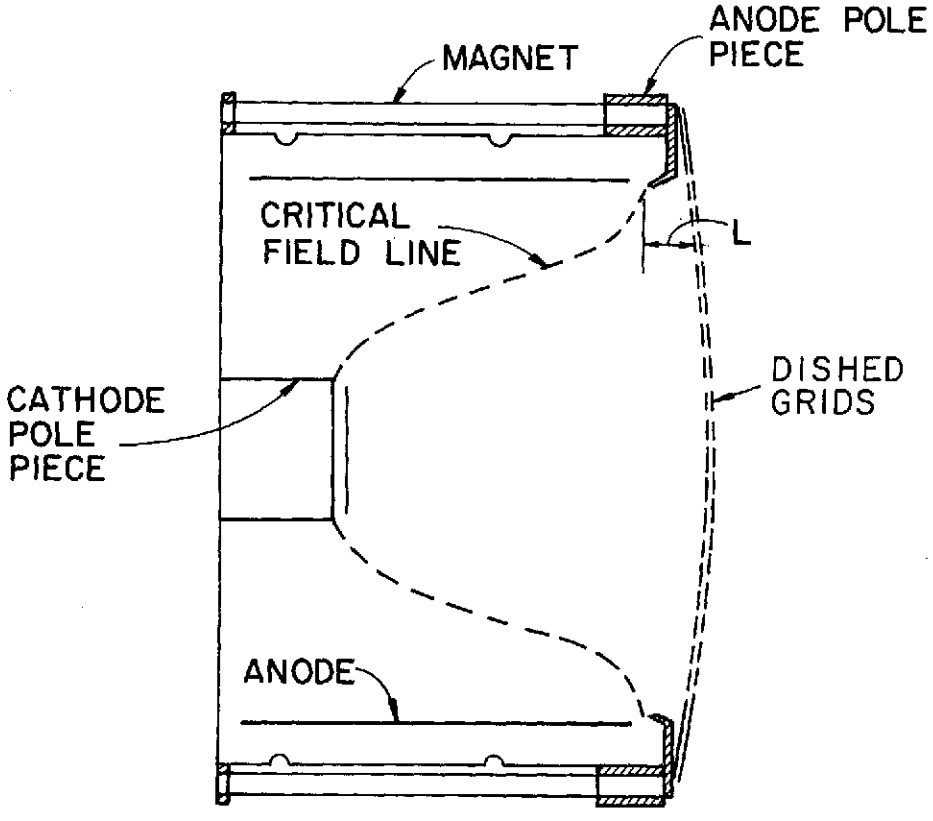


SERT II MAGNETIC FIELD GEOMETRY
FIGURE 6A

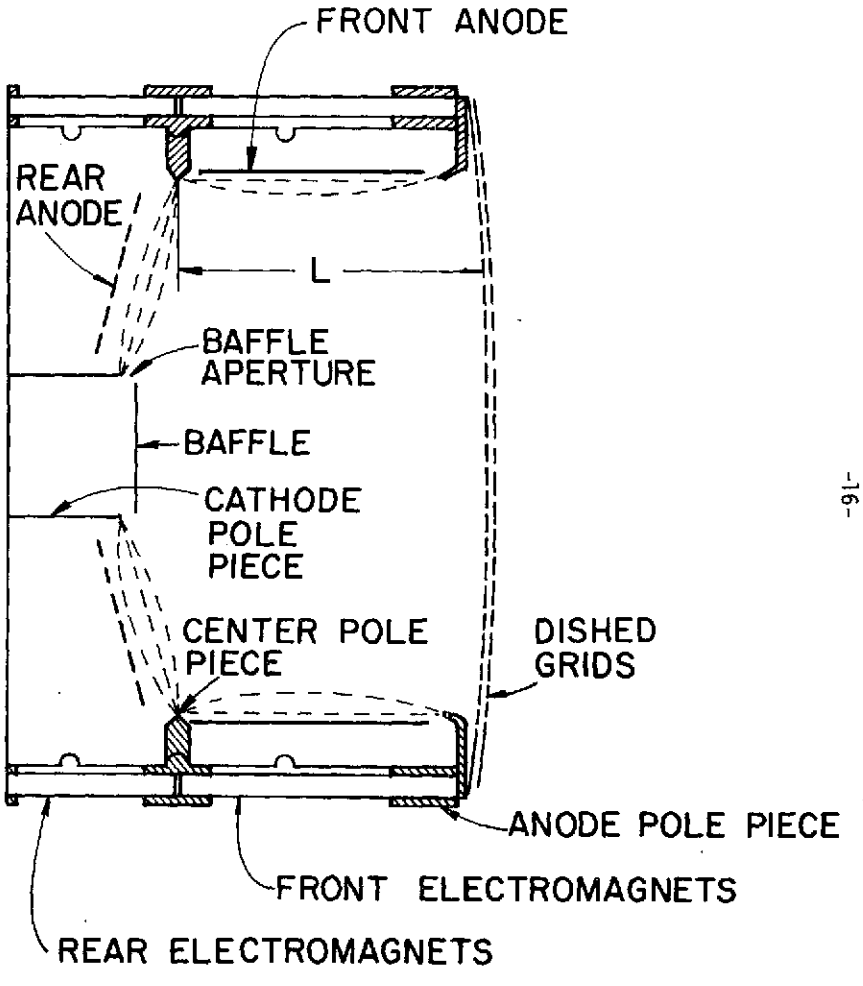


CUSPED MAGNETIC FIELD GEOMETRY
FIGURE 6B

thruster periphery is illustrated by the cusped magnetic field geometry shown in Figure 6B. Assuming uniform plasma properties this geometry should result in a constant neutral residence time throughout the discharge chamber and a value of L which satisfies the design relation presented above. Since the residence time approach does not consider the Maxwellian electron group the design criterion tends to be conservative. Furthermore, one would expect an optimum value of L to exist. That is, very short chambers result in a small residence time and reduced probability of ionization while very long chambers result in a higher probability of ionization but also have a larger wall area on which ions could be lost due to recombination.

Apparatus

The cusped magnetic field geometry illustrated in Figure 6B was achieved by modification of a SERT II discharge chamber. These changes consisted of the addition of a center magnet pole piece, a reduction in the SERT II anode length, and the installation of a rear anode in the upstream end of the discharge chamber. The rear anode was perforated to facilitate a uniform distribution of neutral flow and later in the program the anode was segmented so the current to each segment could be monitored. Additional modifications included the replacement of the SERT II permanent magnets with independent front and rear electromagnets and the installation of a variable magnetic baffle[9] and an uncompensated dished grid optical system. The SERT II propellant feed system was replaced by separate main and hollow cathode vaporizers; a modification which permitted individual control of main and cathode propellant flow rates. A 0.5 mm diameter orifice hollow cathode was installed to facilitate sustained thruster operation at the high beam currents characteristic of dished grids. During the test period the SERT II neutralizer cathode (0.25 mm diameter orifice) was replaced with a 0.5 mm diameter orifice cathode and this modification eliminated an instability which had been observed with the smaller orifice cathode at high beam currents. With the larger neutralizer cathode orifice, emission currents in excess of 0.5 A were drawn for an indefinite time while the discharge operated stably in the plume mode.

During the course of the experiments the SERT II soft iron main flow distributor was replaced with an assembly constructed of non-magnetic aluminum. The purpose of this modification was to insure the minimum magnetic flux path length through the plasma was between the center and cathode pole pieces. This modification reduced the axial component of the magnetic field in this region and resulted in a more uniform distribution of current to the rear anode.

Unless otherwise stated, all data presented in this section were obtained at +1 kV and -0.5 kV screen and accelerator grid potentials and 0.3 A cathode keeper current. Solid symbols have been used on performance curves to indicate the 37 V arc voltage condition. Discharge power calculations include the keeper discharge loss.

Magnetic Bottle Experiments

Early studies conducted on the cusped magnetic field (CMF) thruster indicated the absence of the typical performance curve "knee" under some operating conditions and propellant utilizations of over 100% were frequently observed. Since the flow rate measurements were considered accurate to within a few percent, this latter observation suggested the presence of a large double ion population in the discharge chamber. These observations led to the development of a discharge chamber model based on the existence of a magnetic bottle in the region between the center and cathode pole pieces as suggested by Figure 6B. From this model a rather comprehensive discharge chamber theory[4] was postulated to explain the performance characteristics and ion beam profile achieved with the CMF thruster design. The theory predicts primary electrons leaving the baffle aperture are trapped in the magnetic bottle producing a localized ionizing region in the upstream end of the discharge chamber. The ions produced in this region drift through the chamber and are lost by one of the following means: (1) recombination on the thruster walls, (2) extraction by the accelerating system, or (3) double ionization as a result of electron impact. The first and third loss mechanisms can be used to explain the observed performance characteristics of this thruster and suggest modifications which should improve the performance and flatten the beam profile. Since the model was based on the existence

of a magnetic bottle region in the upstream end of the discharge chamber, Langmuir probe measurements were made in an attempt to verify the bottle concept experimentally. Langmuir probe data presented in this section were analyzed by the numerical procedure presented in Appendix A.

The results of these measurements are presented in Figure 7 which indicates the variation of the plasma properties with axial position at a radial location which was 67% of the chamber radius. These data confirm the presence of a high energy density zone at an axial position roughly corresponding to the location of the center magnet pole piece. Plasma property variations at different radial locations exhibit the same trends evident in Figure 7.

Reductions in Discharge Chamber Length

The physical model of the cusped field discharge chamber suggests the ion beam profile can be flattened by reducing the length of the chamber. This would result from the achievement of a more uniform ion density profile inside the chamber due to a reduction in wall losses. That is, with a shorter chamber ions produced in the upstream end would have less probability of being lost to the thruster walls. In addition, the double ion population which distorts the measured beam profile should be reduced since single ions would have a smaller chance of becoming doubly ionized in a shorter chamber. The model also predicts a reduction in baseline discharge losses resulting from the decrease in wall area. Even for discharge chambers which are modeled as having uniform plasma properties, the theoretically predicted double ion population and baseline discharge losses are shown to be strongly dependent on the discharge chamber length[4].

The cusped magnetic field thruster was operated at three different length to diameter ratios corresponding to an overall thruster length of 100%, 75%, and 63% of the SERT II thruster length. The ion beam current density profiles measured 5 cm downstream of the accelerator grid are presented in Figure 8 for the SERT II and cusped field configurations. These data were normalized such that the integrated beam current is the same for each profile. When normalized in this manner, the profile having the lowest peak current density yields the highest flatness parameter

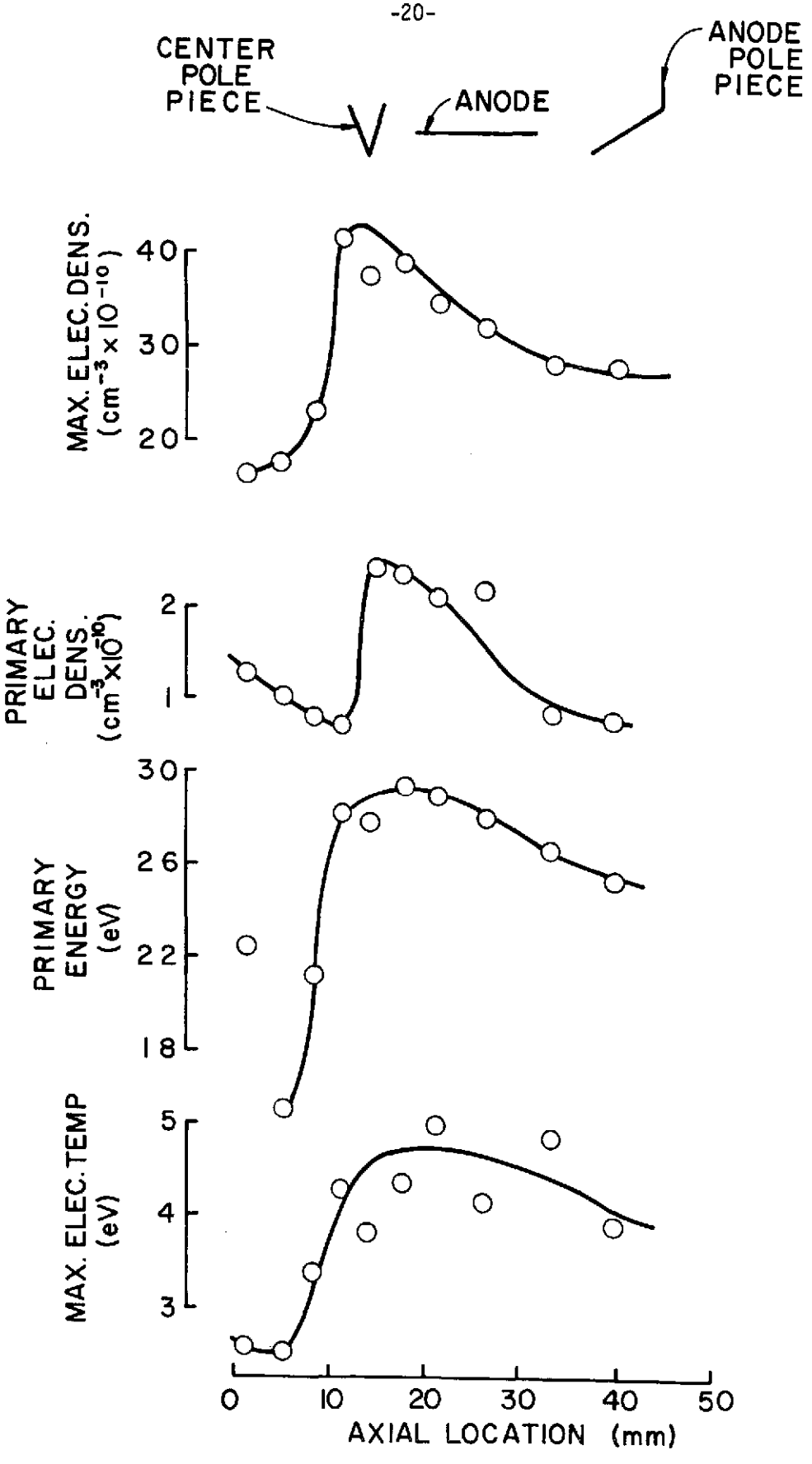


PLASMA PROPERTY VARIATION AT 67% OF THE CHAMBER RADIUS

FIGURE 7

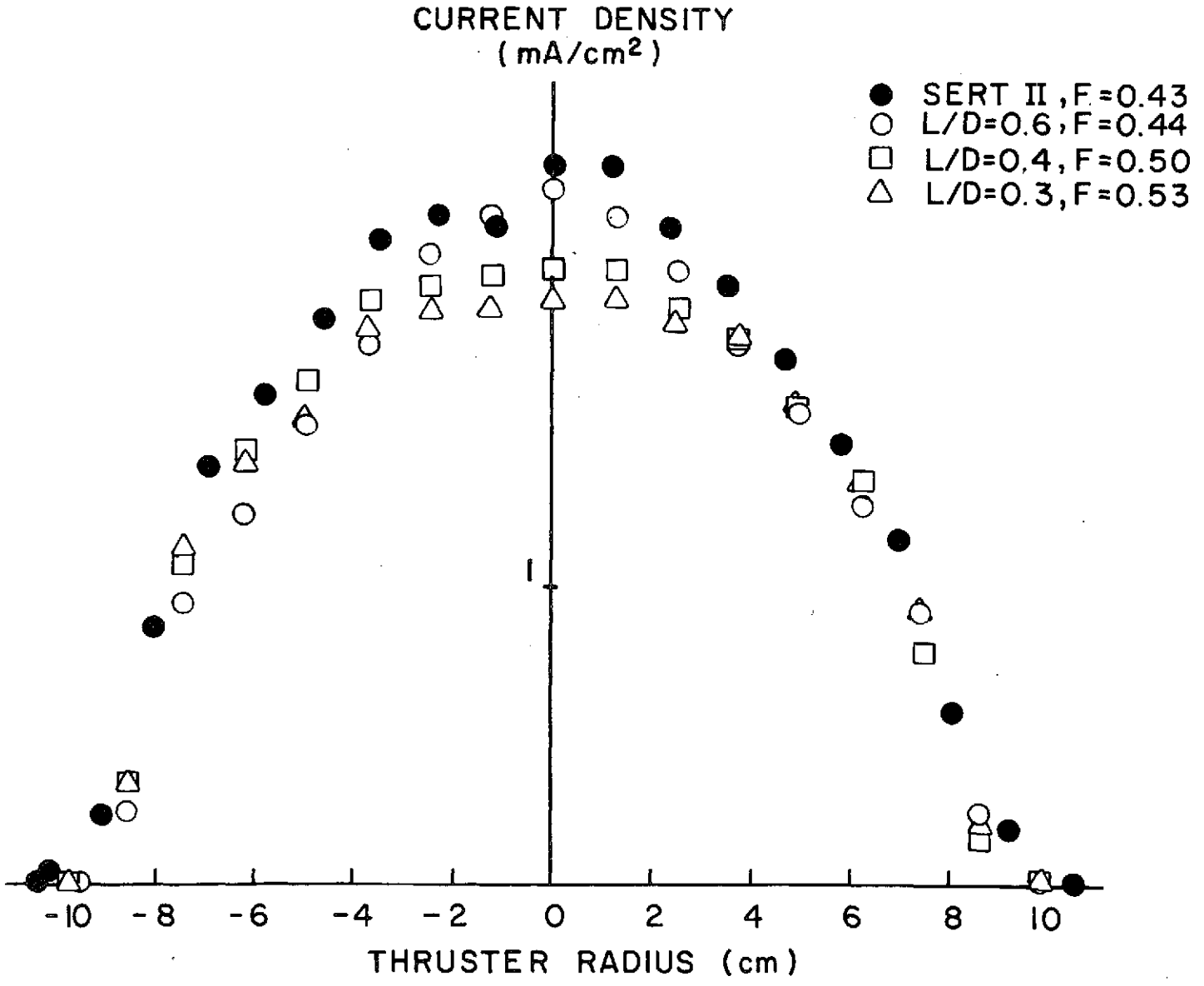


NORMALIZED BEAM CURRENT DENSITY PROFILES

FIGURE 8

providing the beam radius is the same for each profile. The data of Figure 8 indicate a significant flattening of the profile was realized as a result of shortening the discharge chamber. The flatness parameter corresponding to a chamber length to diameter ratio of 0.3 indicates a 25% increase over the SERT II value.

Langmuir probe data were recorded at various radial locations close to the screen grid and the ion density profiles calculated from these measurements are presented in Figure 9. Qualitatively these data confirm the theory that the ion beam profile can be flattened by flattening the ion number density profile at the screen grid.

The variation of the axial magnetic field strength with radial distance from the thruster centerline is presented in Figure 10 for the three different length to diameter ratios investigated. These data were obtained from gaussmeter measurements taken at an axial location midway between the center and front magnet pole pieces. Figure 10 indicates that as the length to diameter ratio was decreased the axial magnetic field was confined to a region progressively closer to the front anode. The achievement of a relatively field-free region over the bulk of the discharge chamber would be expected to result in a more uniform ion beam profile and improved thruster performance. The existence of this region is further illustrated by the iron filings map of Figure 11.

Discharge loss data are presented in Figure 12 for the modified SERT II and cusped field configurations. These data indicate a substantial reduction in baseline discharge losses was realized as the chamber length was decreased. Since the maximum and minimum L/D data both indicate propellant utilization efficiencies in excess of 100% it is difficult to infer any trends relating the double ion content of the beam to the chamber length. Direct measurements of the double ion content of the beam have not been made at the time of this writing due to lack of the necessary measuring equipment. However, a mass spectrometer will be acquired in the near future and when operational will be used to determine the double ion content of the exhaust beam as a function of chamber length.

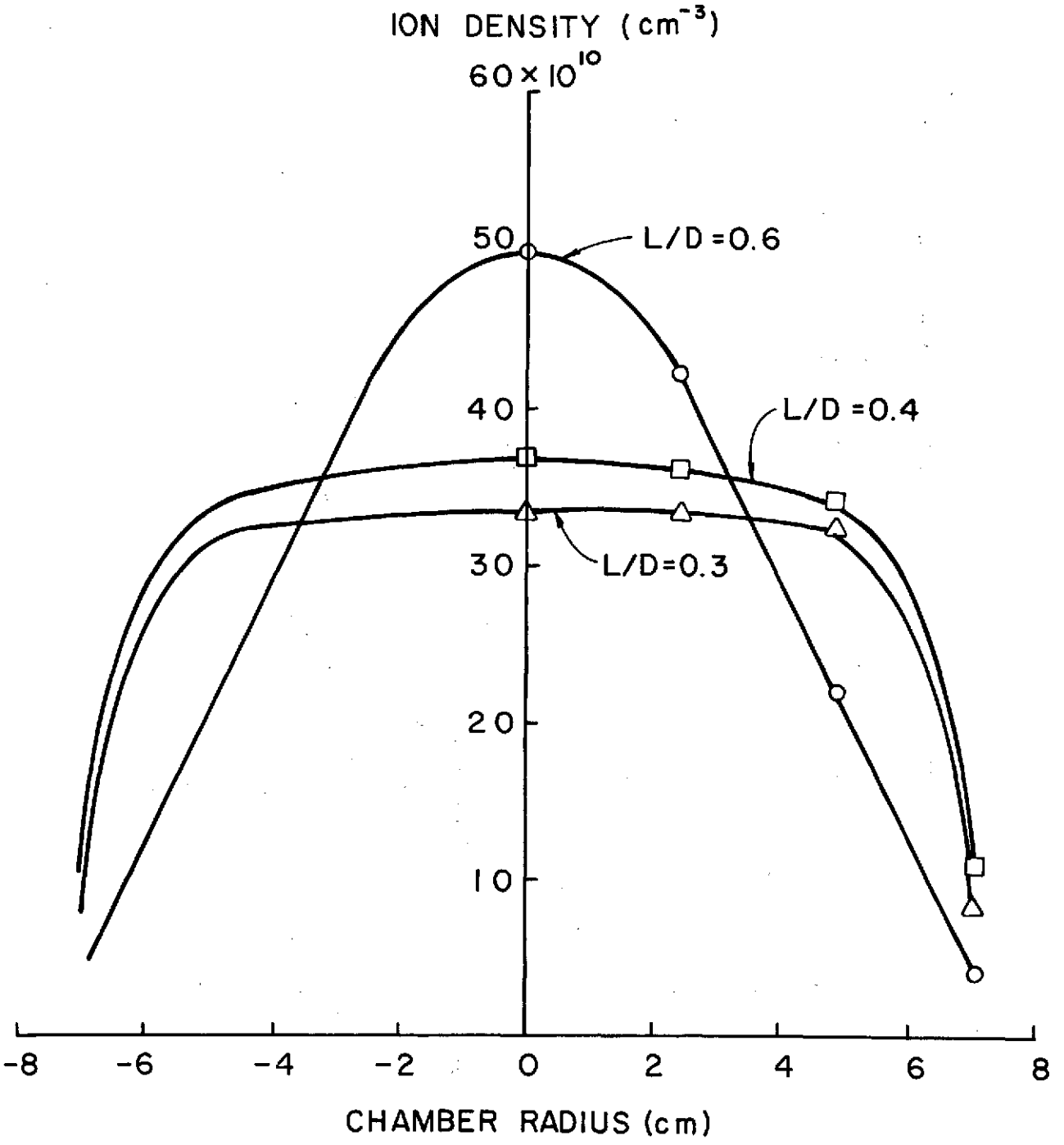


ION NUMBER DENSITY PROFILES

FIGURE 9

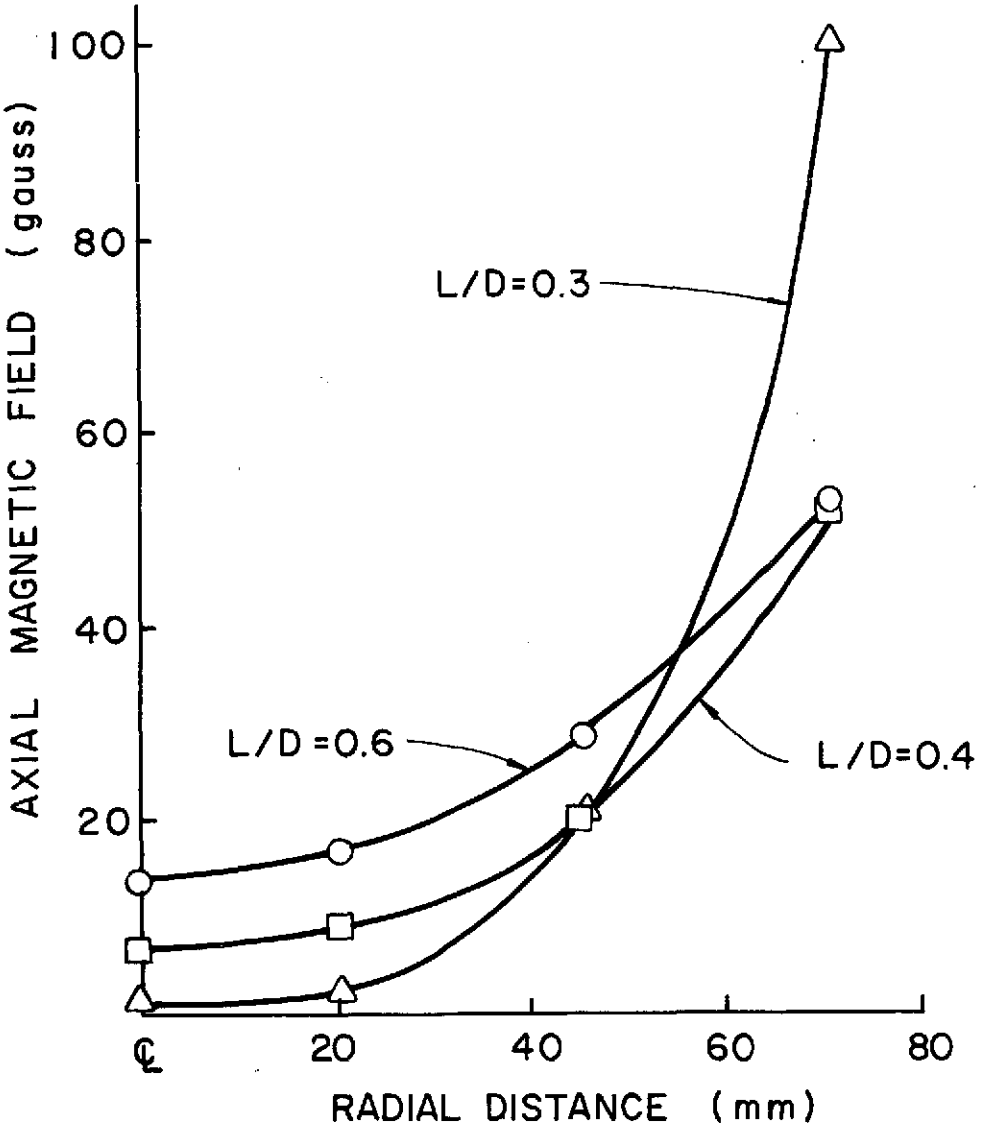


MAGNETIC FIELD VARIATION AT AN AXIAL LOCATION CORRESPONDING TO L/2

FIGURE 10

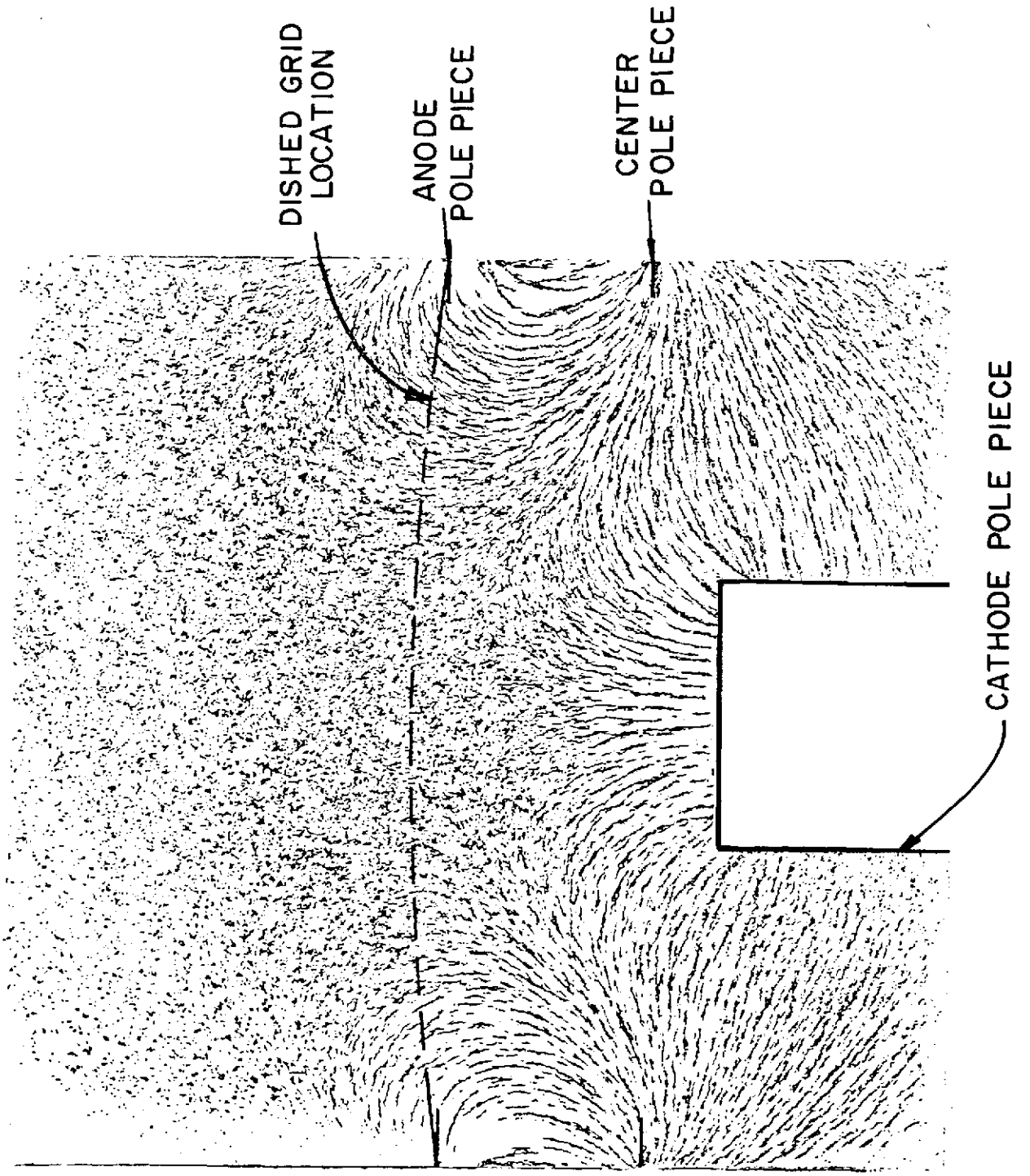


IRON FILINGS MAP (L/D = 0.3)

FIGURE 11

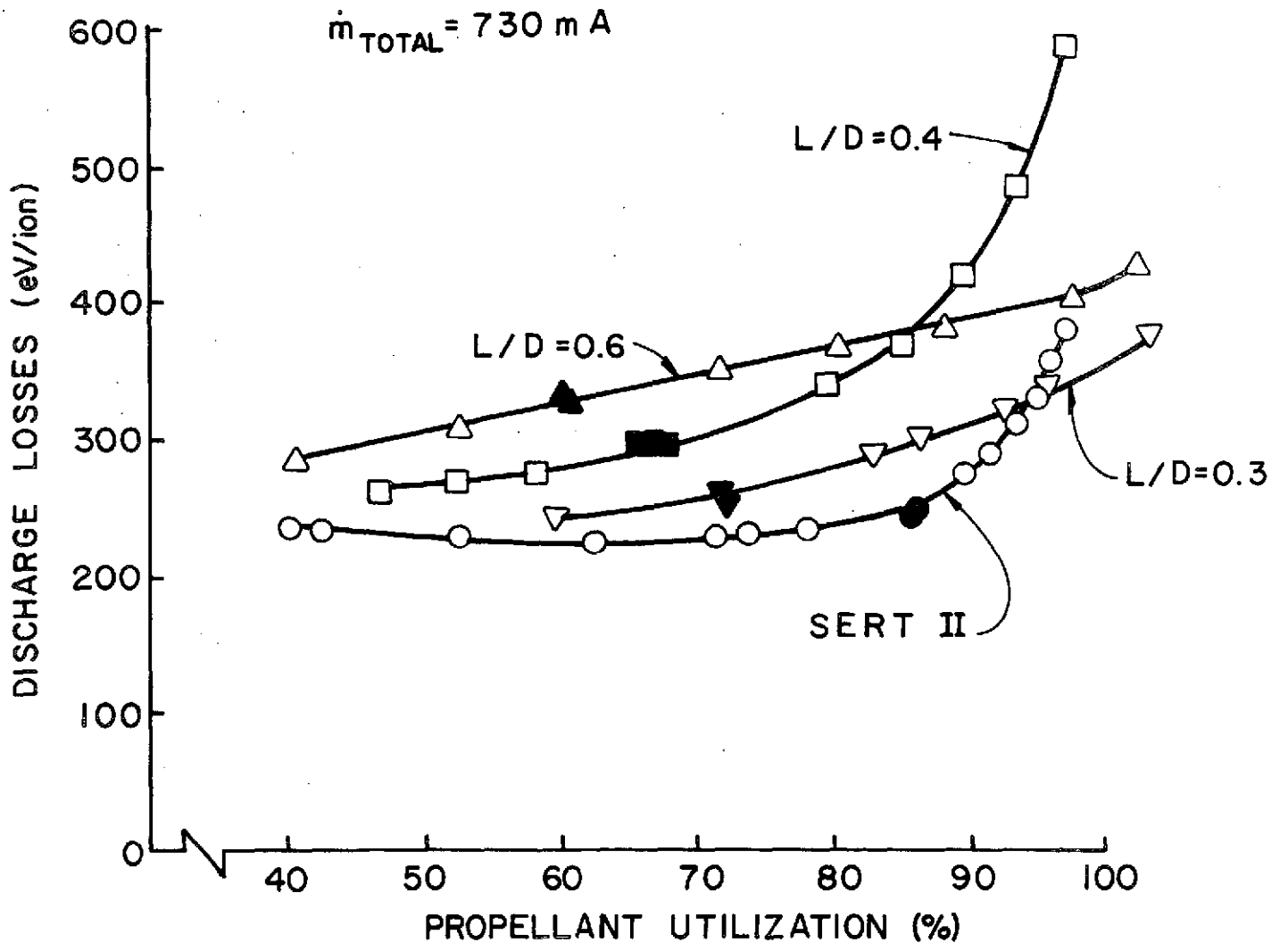


THRUSTER PERFORMANCE COMPARISON

FIGURE 12

Throttling Experiments

The effect of varying the propellant flow rate on the beam profile and performance curve was investigated with the discharge chamber corresponding to an L/D of 0.3. Beam profiles measured 5 cm downstream of the accelerator grid are presented in Figure 13 and indicate the beam flatness parameter is essentially constant over a flow rate range of 400-700 mA. Throttled performance data were obtained over a 500 mA range in total propellant flow rate and are presented in Figure 14. These data indicate the same general trends which had been observed with the original CMF chamber length (L/D = 0.6), and suggest the thruster performance is essentially independent of total flow rate in the 680-900 mA range.

Radial Field Thruster

The discharge chamber length to diameter ratio was reduced to zero by removing the front anode and center pole piece as illustrated in Figure 15. This modification resulted in an overall thruster length which was 38% of the SERT II design and a magnetic field geometry which was predominantly radial. The measured beam profile achieved with this configuration was found to be very peaked and the maximum propellant utilization was quite low. Iron filings maps of the magnetic field existing in the discharge chamber revealed the fact that the field lines leaving the baffle aperture region intercept the screen grid at a small fraction of the thruster radius. It was also determined that the point of interception was a function of the magnetic baffle diameter and that the shape of the beam profile was strongly influenced by the radial location of the interception point. These observations are illustrated in Figures 16 and 17. The reason for the peaked beam profile and low propellant utilization is apparent by considering Figure 16. The volume defined by the magnetic field line emanating from the tip of the cathode pole piece and the screen grid is confined to a small region near the thruster centerline. Primary electrons are injected directly into this central region and are reflected from the screen grid and baffle by the strong electric fields which exist there. Primaries escape this region by collisions with neutrals and expend some of their energy in doing so.

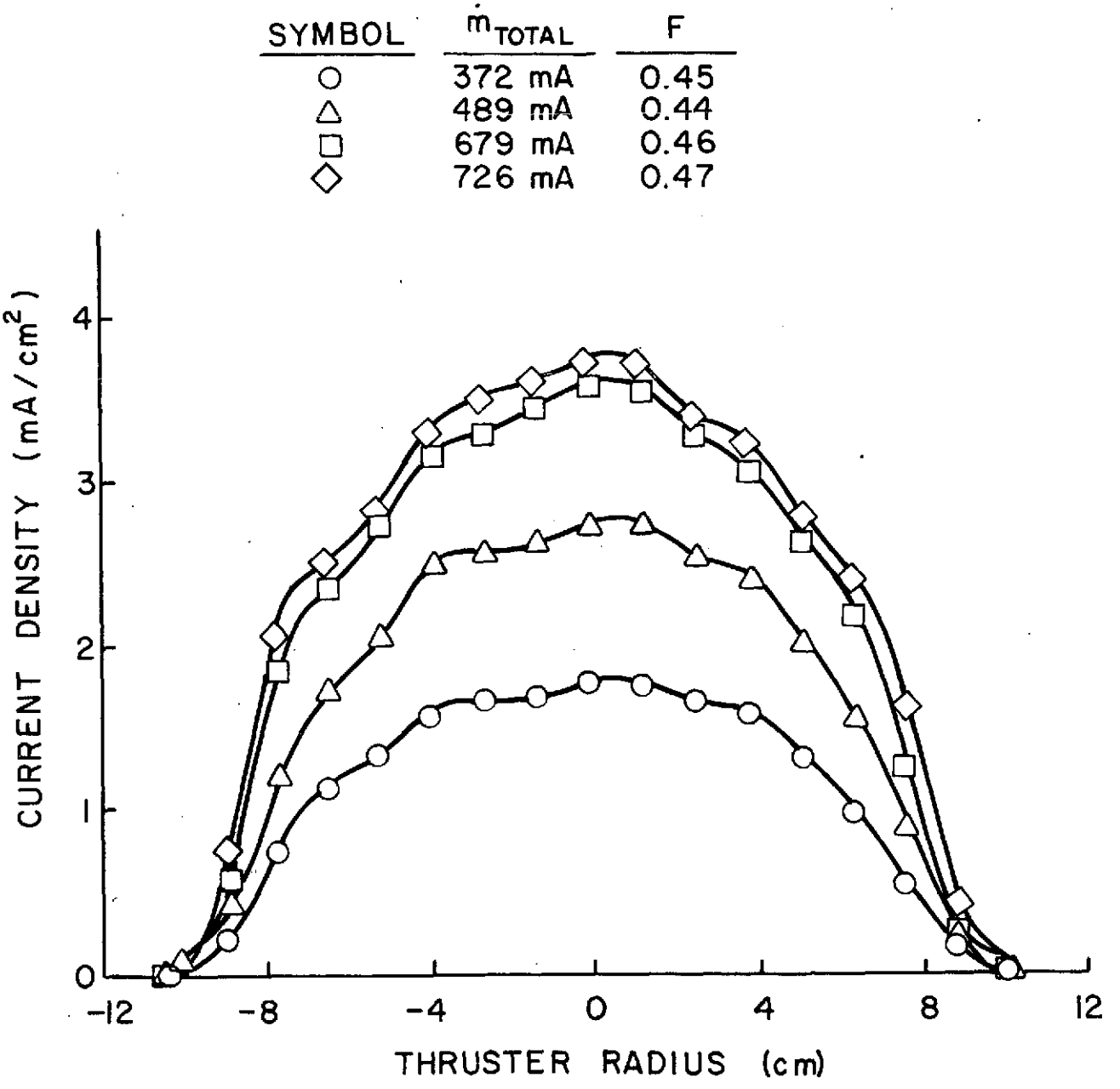


EFFECT OF TOTAL PROPELLANT FLOW RATE ON BEAM PROFILE

FIGURE 13

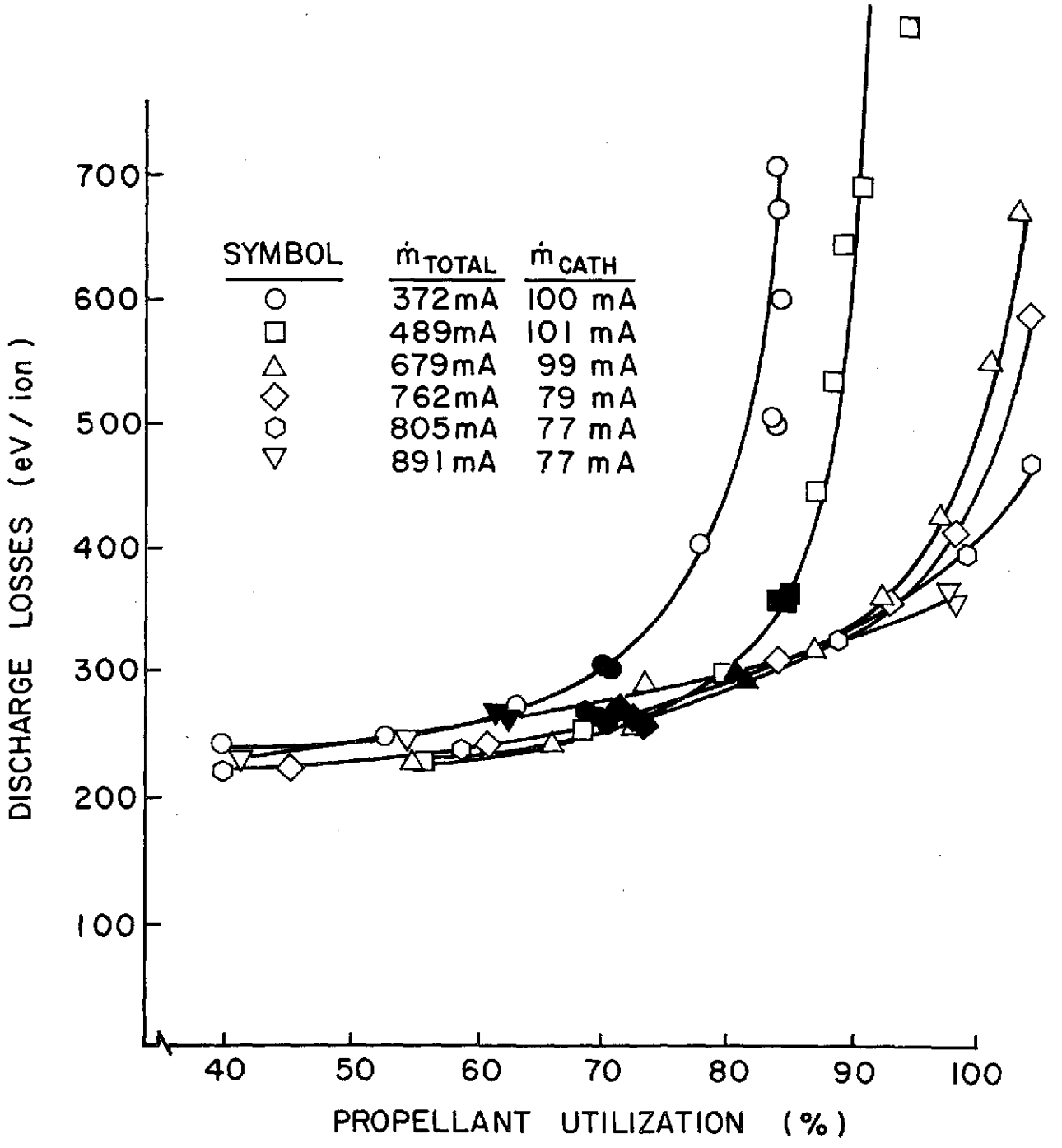


EFFECT OF TOTAL PROPELLANT FLOW RATE ON PERFORMANCE

FIGURE 14

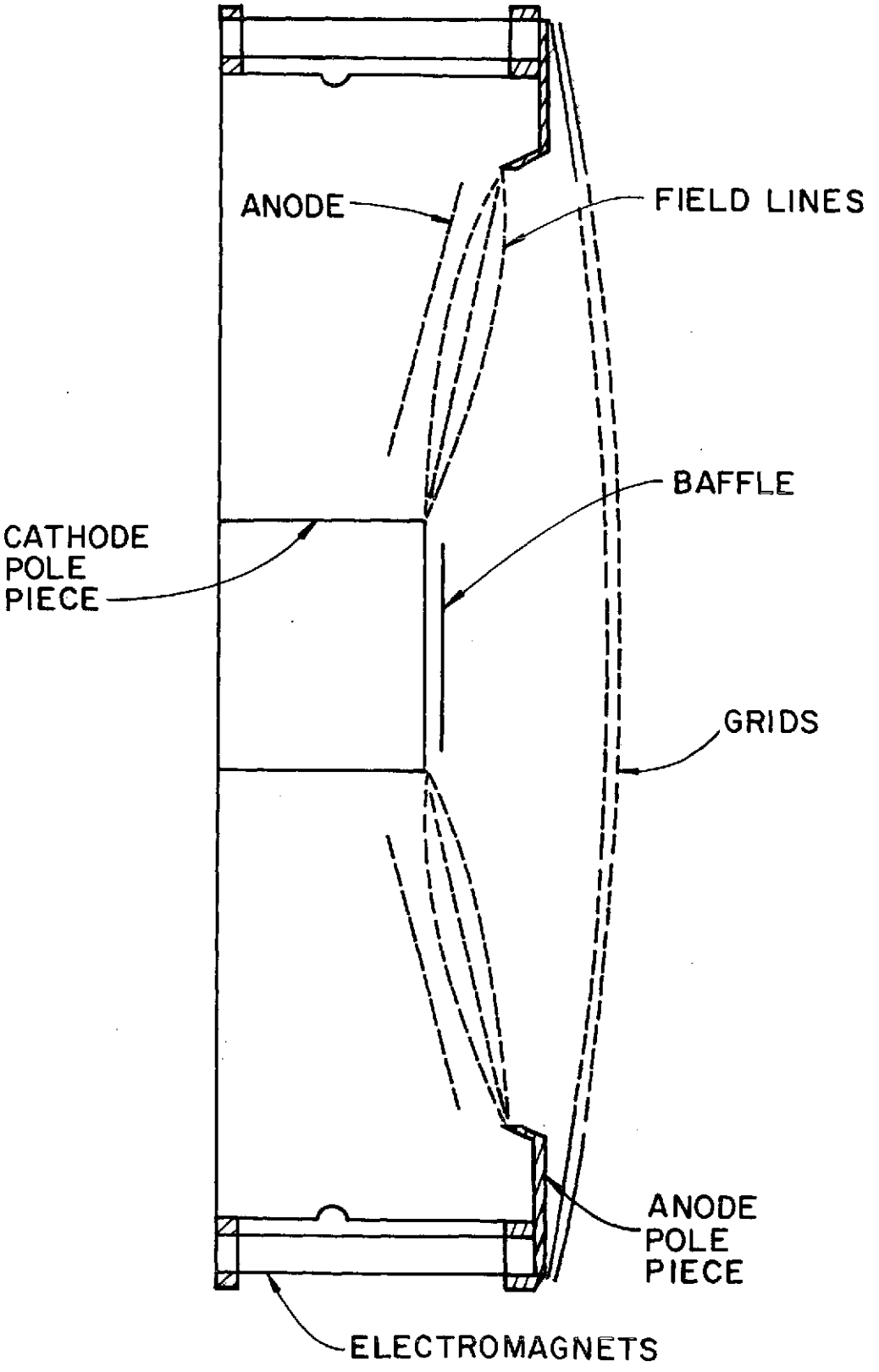


RADIAL FIELD THRUSTER

FIGURE 15

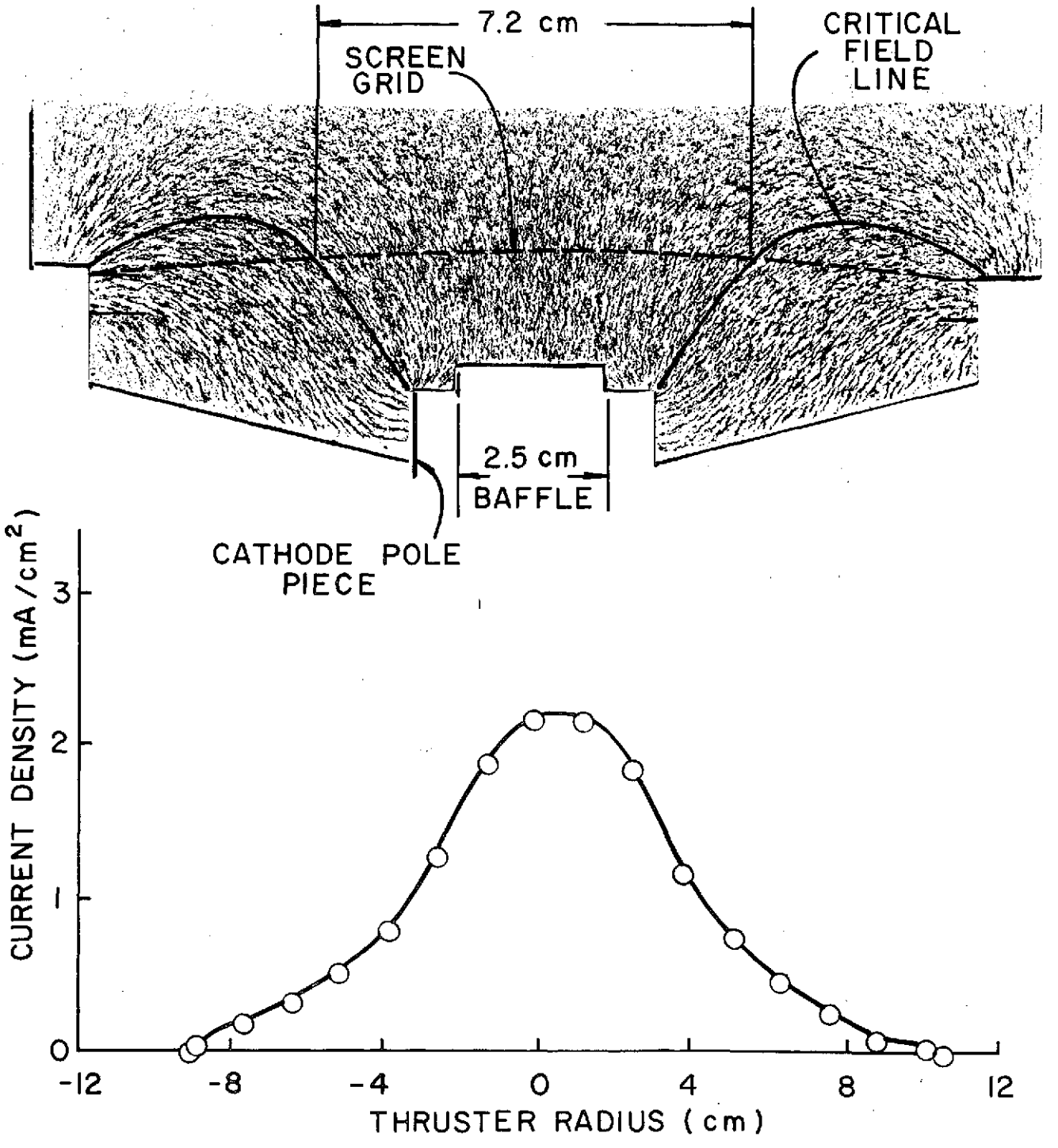


MAGNETIC FIELD GEOMETRY AND BEAM CURRENT DENSITY PROFILE - SMALL BAFFLE

FIGURE 16

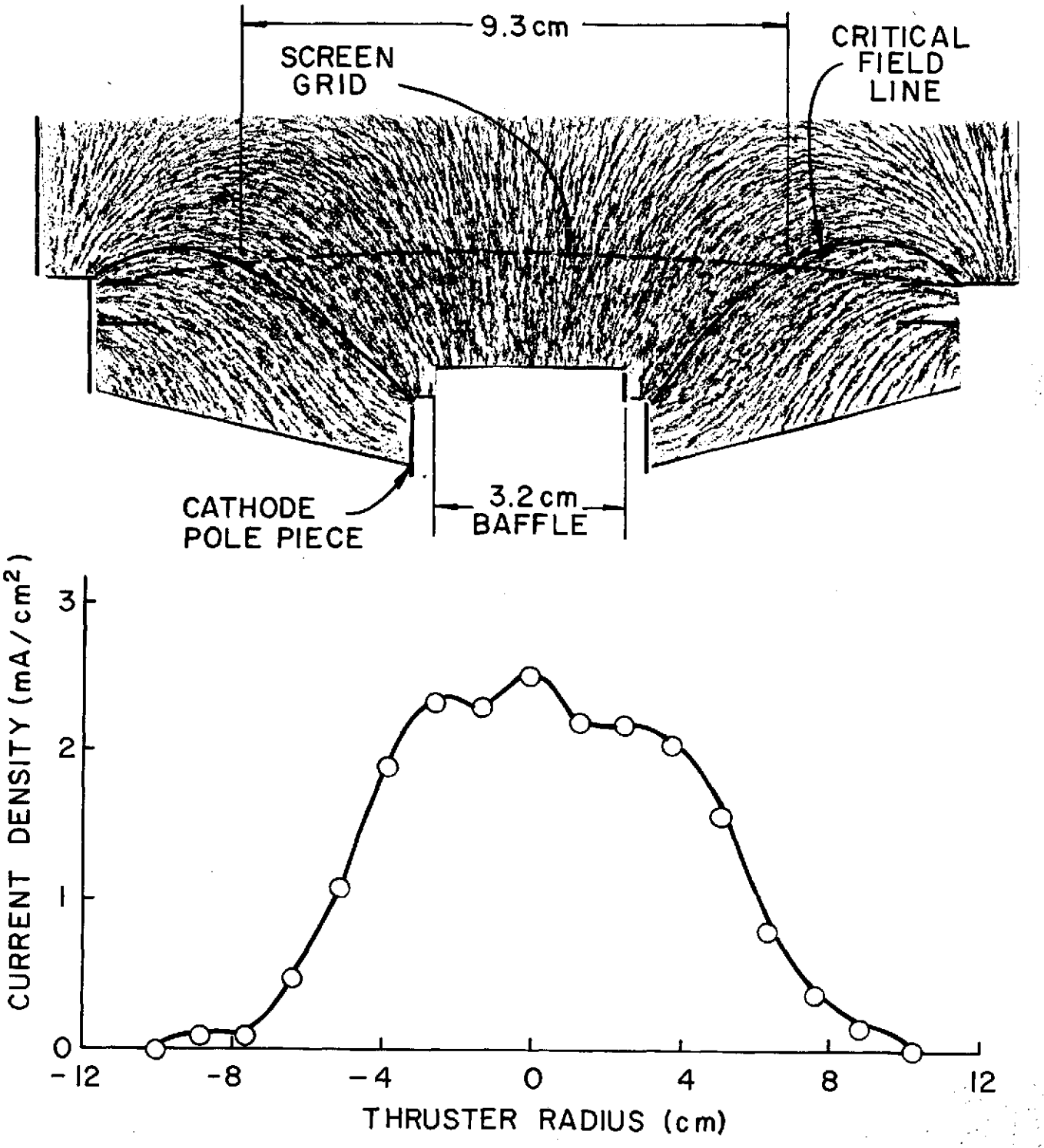


MAGNETIC FIELD GEOMETRY AND BEAM CURRENT DENSITY PROFILE - LARGE BAFFLE

FIGURE 17

Hence one would expect most of the ionizing collisions to occur near the thruster centerline and fewer, less productive collisions to occur outside this central volume. This theory explains the peaked beam profiles and high neutral loss rates observed with the radial field geometry of Figure 15.

In order to verify the theory presented above, the grid system was moved downstream a distance of approximately 3 cm. This discharge chamber geometry, shown in Figure 18, was derived from the cusped field geometry having an L/D value of 0.3 simply by removing the front electromagnets. An iron filings map indicating the location of the grids with respect to the magnetic field lines leaving the baffle aperture region is presented in Figure 19. This shows the volume defined by the magnetic field line leaving the tip of the cathode pole piece and the screen grid has been expanded to cover the entire cross section of the discharge chamber. In addition, the neutral residence time in the primary electron volume has been increased considerably. This modification resulted in a significant flattening of the ion beam profile as the theory predicted. A comparison of the beam current density profiles for the upstream and downstream grid locations is presented in Figure 19. These data show the beam flatness parameter was doubled when the grids were moved downstream. Performance data for the two configurations are presented in Figure 20 which indicates the maximum propellant utilization was increased by a factor of almost two when the accelerator system was positioned downstream. The baseline discharge losses are seen to be about the same for both configurations even though the chamber wall area on which ion recombination could occur was considerably smaller for the upstream grid location. This fact suggests the ratio of primary electron region total surface area to effective grid open area remained constant as the grids were moved downstream. This conclusion is based on the analysis presented in Reference 10 which relates the baseline beam ion production cost to the ratio of total to open area of the primary electron region.

Segmented Anode Studies

Based on the critical field line concept it was predicted that most of the arc current going to the rear anode would be drawn at a radial

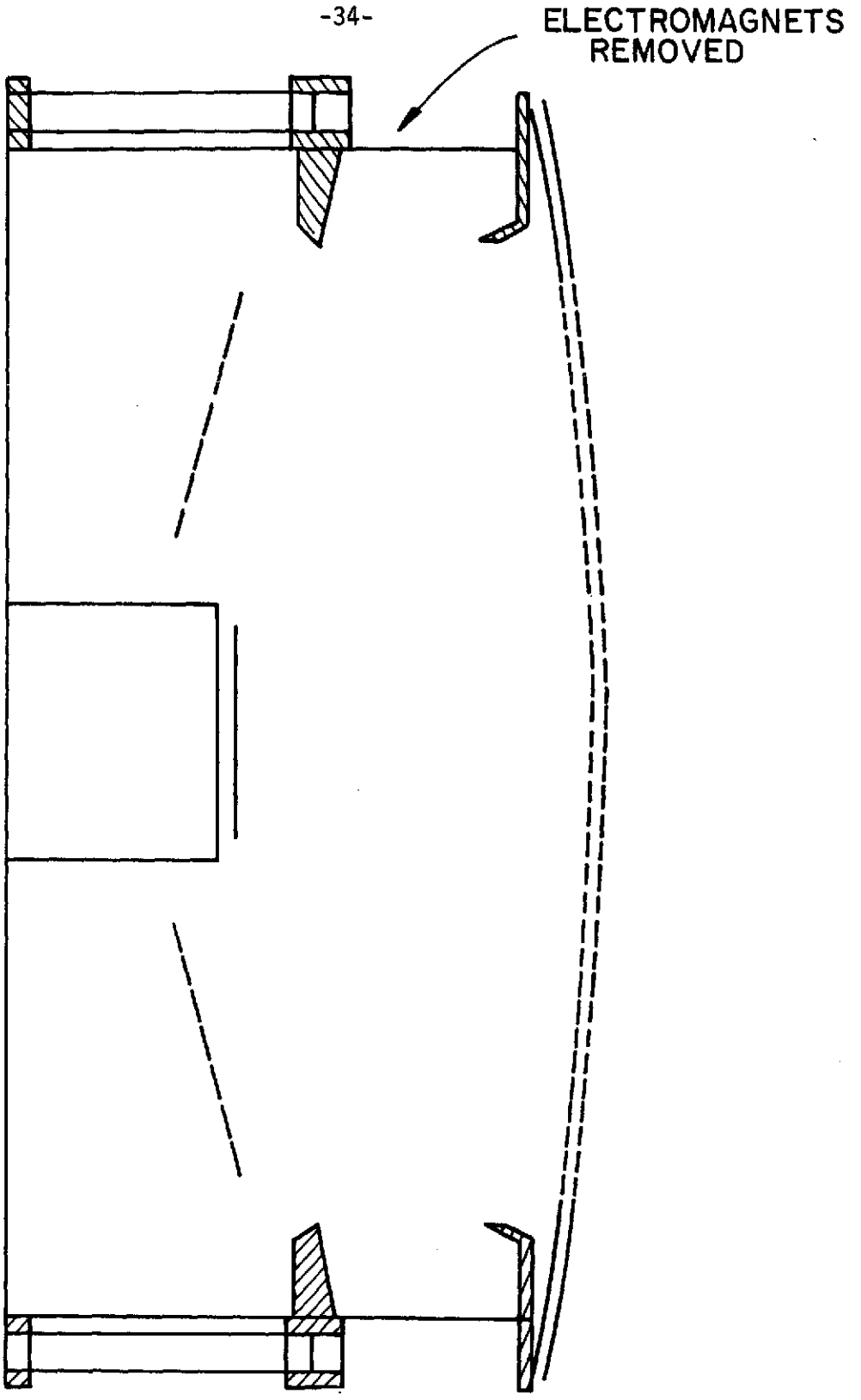


RADIAL FIELD THRUSTER WITH GRIDS RELOCATED DOWNSTREAM

FIGURE 18

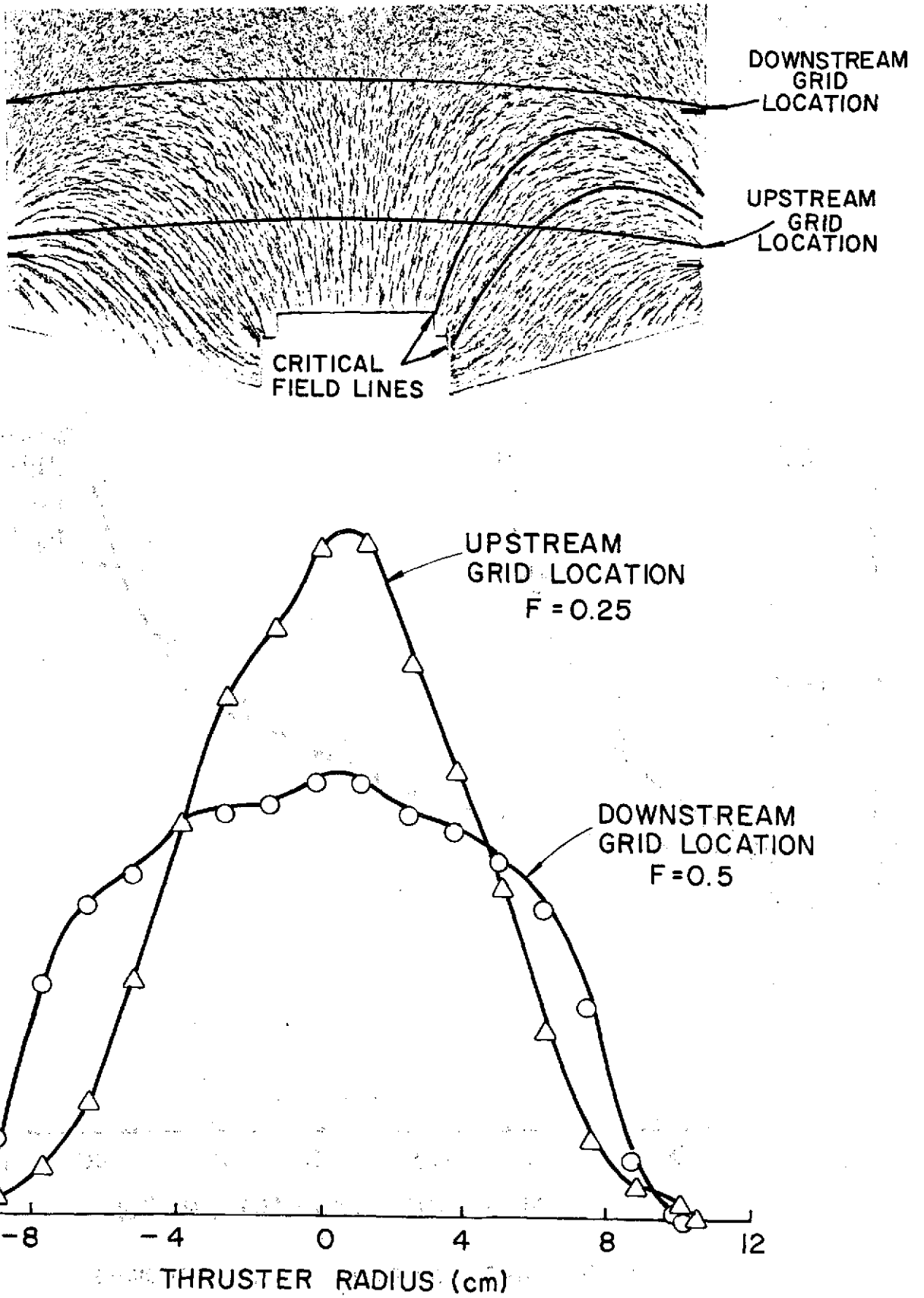


GRID LOCATION AND BEAM CURRENT DENSITY PROFILE COMPARISON

FIGURE 19

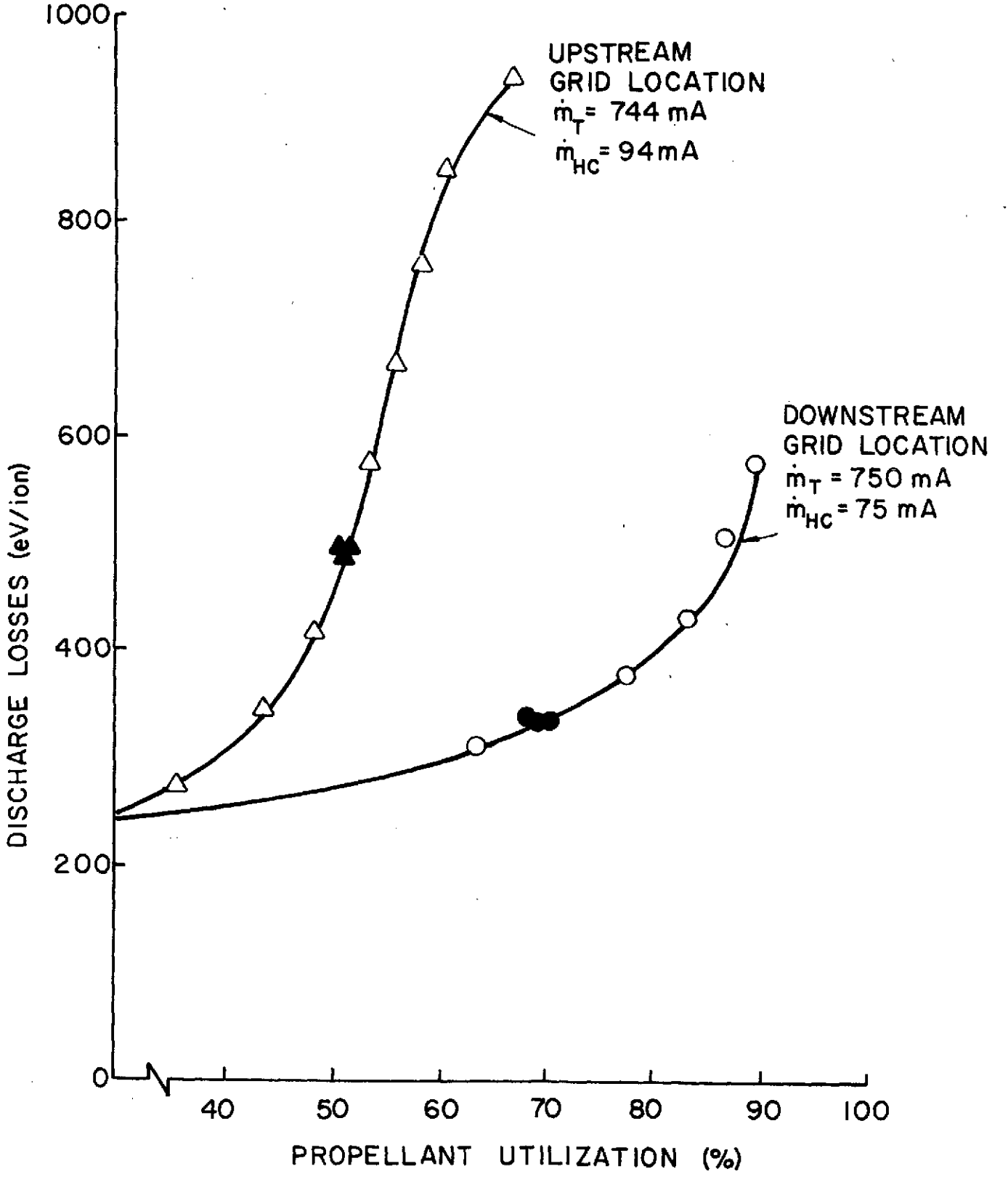


EFFECT OF GRID LOCATION ON THRUSTER PERFORMANCE

FIGURE 20

location close to the thruster centerline. This argument is based on the fact that an electron proceeding from the primary electron region will go to the anode along the first magnetic field line that intercepts the anode. The iron filings map presented in Figure 21 indicates the innermost field line which intercepts the rear anode does so at the inner edge of the anode. In order to verify this theory the rear anode was segmented to form two concentric annular anodes. This modification was found to have no effect on the thruster performance or beam profile. The current to each rear anode segment was measured and it was found that 95% of the total rear anode current was drawn by the inner segment as theory predicted.

It was believed electron current was being drawn predominately to the inner edge of the anode because of the large axial component of the magnetic field in the vicinity of the rear anode. The reason for this large axial field component is apparent if the relative lengths of the magnetic flux paths labeled $L_1$ and $L_2$ in Figure 21 are considered. This figure shows that $L_1 < L_2$ and that a large fraction of the magnetic flux therefore travels along the path of lower reluctance ($L_1$) to the soft iron flow distributor. In order to achieve a more radial field in the region between the center and cathode pole pieces, the SERT II flow distributor which served as the upstream boundary of the discharge chamber was replaced by a non-magnetic aluminum one. This modification insured the shortest flux path was between the pole pieces and produced a predominantly radial magnetic field in the vicinity of the rear anode as illustred in Figure 11. The measured ratio of inner to outer segment arc current was found to decrease by about 2:1; however, the performance and beam profile were essentially unchanged by this modification.

Electron Injection Studies

In order to investigate the effects of injecting electrons into the relatively field-free region in the vicinity of the accelerator system, a moveable non-magnetic sleeve and baffle assembly was installed inside the soft iron cathode pole piece. With this arrangement the point of electron injection relative to the magnetic field geometry could be varied

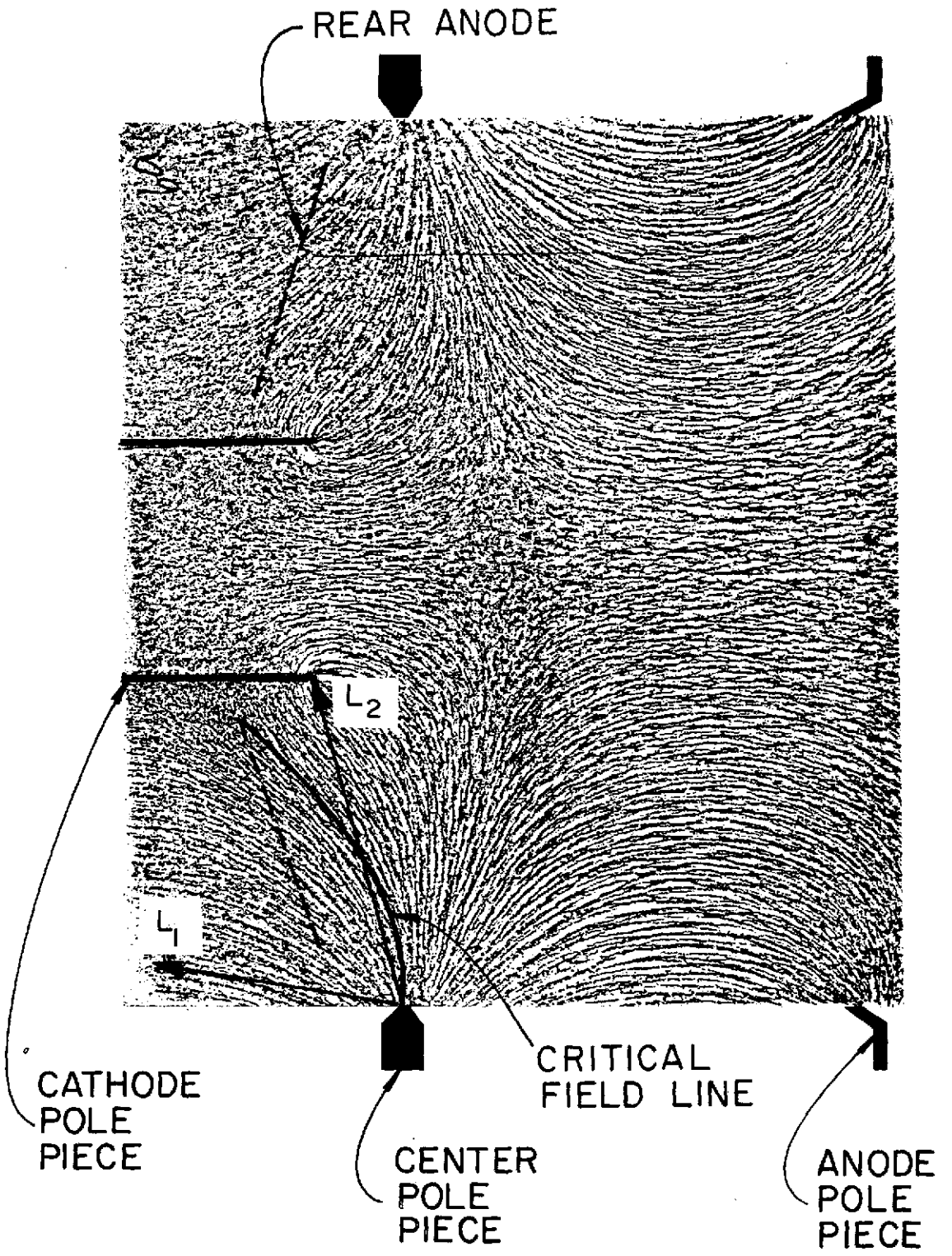


IRON FILINGS MAP (L/D = 0.6)

FIGURE 21

while the thruster was operating. The location of the baffle aperture with respect to the cathode pole piece and magnetic field lines is illustrated in Figure 22 for the fully extended sleeve position. For these experiments the variable magnetic baffle was removed and the arc voltage was controlled by the cathode flow rate. The total flow rate, magnet currents, and baffle aperture area were held constant.

The beam profiles measured at a distance of 5 cm downstream of the accelerator system indicated only a slight increase in the flatness parameter as the point of electron injection was moved closer to the screen grid. The flatness parameter at this downstream position of the probe was typically 0.51.

Performance data for the three axial positions of the baffle aperture are presented in Figure 22. These data indicate about a 25 eV/ion increase in baseline discharge losses occurred as the sleeve assembly was extended into the discharge chamber. The performance curves for the intermediate and fully extended positions are identical up to about 90% utilization. At this point the two curves diverge and the flatter curve in attributed to the existence of a significant double ion population at the higher arc voltage measured with the sleeve extended 21.3 mm. The reason for the arc voltage difference as the sleeve is moved out is not understood.

Beam Profile Extrapolation Studies

Several methods of determining the value of the beam profile flatness parameter at the plane of the accelerator grid were investigated during the electron injection studies described in the previous section. The following procedures were used to determine the beam flatness parameter:

a. The peak current density was measured at several axial locations and the value at the plane of the accelerator grid was determined by extapolation of these data. The flatness parameter at the grids was then calculated from the extrapolated peak current density and the average current density determined from the metered beam current and the cross sectional area of the beam.

b. Current density profiles were measured at four axial locations and the current densities at a given radial

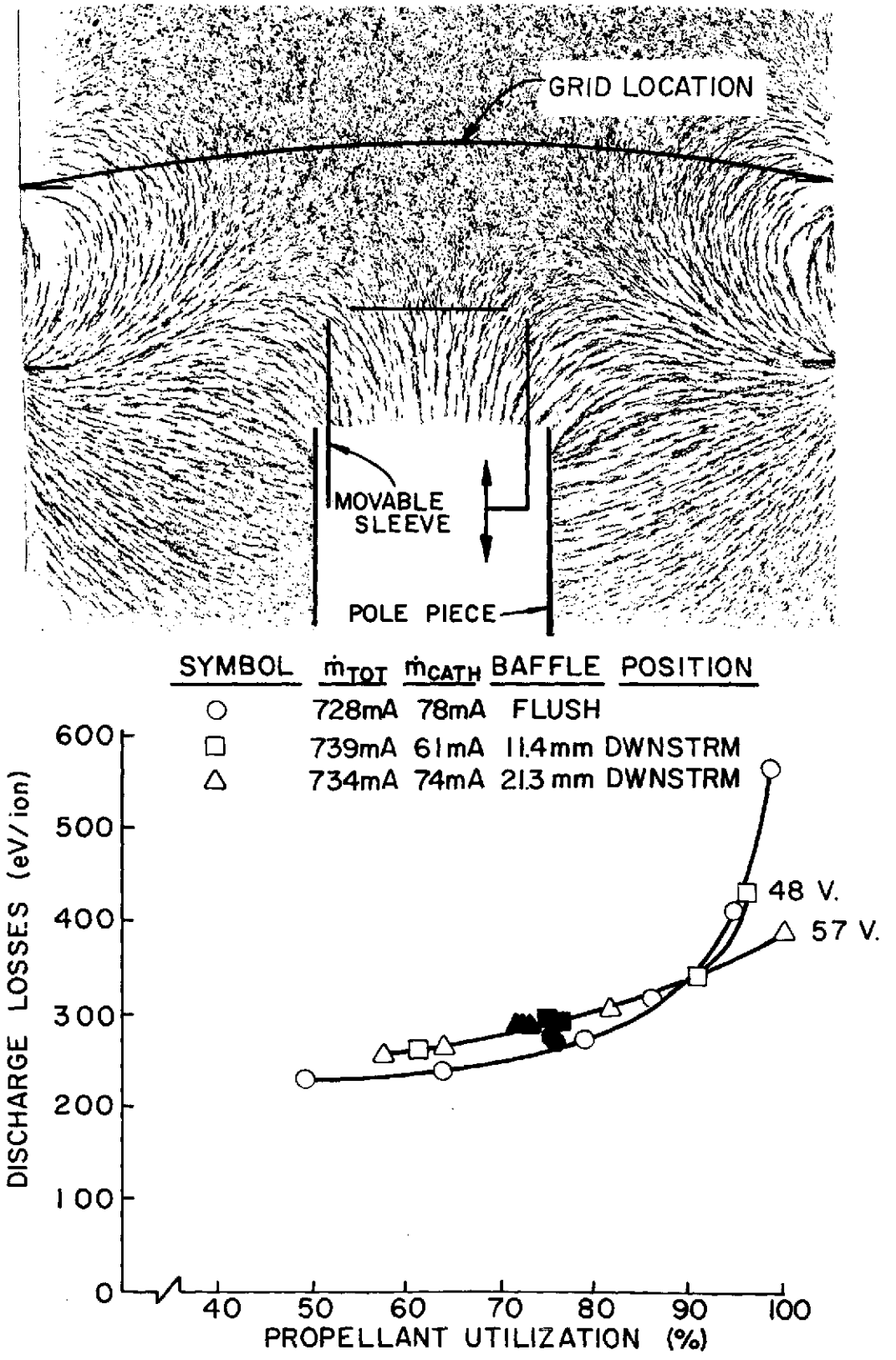


ELECTRON INJECTION GEOMETRY AND THE EFFECT OF BAFFLE POSITION ON THRUSTER PERFORMANCE

FIGURE 22

location were extrapolated to determine the corresponding current densities at the grids. The flatness parameter was then found by taking the ratio of average to peak current densities determined from this extrapolated profile.

c. The beam profiles were measured at three axial locations and a flatness parameter calculated for each profile. The flatness parameter at the accelerator grid was found by extrapolation of the calculated flatness parameters.

The beam flatness parameters obtained by these methods are presented in Figure 23. The abscissa represents the axial location (relative to the downstream edge of the cathode pole piece) of the point of injection of electrons into the discharge chamber. Although the flatness parameters determined by each method do not agree exactly, it is apparent from Figure 23 that flatness parameters of the order of 0.7 to 0.8 are being achieved with the cusped magnetic field geometry. Since method "a" outlined above involves less extrapolation, analysis, and measurement and accounts for both the curvature of the grids and beam divergence, this procedure is considered most accurate. This suggests beam flatness parameters as high as 0.9 are being realized with the cusped field thruster. Figure 24 presents a typical beam profile determined by the procedure described in "b" above.

## Conclusions

A SERT II-type divergent field thruster was modified to produce a cusped magnetic field geometry. The distance between the front and center magnet pole pieces, which determines the primary electron region length to diameter ratio (L/D), was varied over a range from 0.0 to 0.6. The beam profile flatness was found to increase with decreasing L/D in agreement with theory. For an L/D value of 0.3 the flatness parameter at a distance of 5 cm downstream of the accelerator grid was about 25% higher than the SERT II value. For a given propellant, specific impulse, and accelerator grid this implies a 25% increase in time integrated thrust. Based on reductions in maximum beam current density this implies a 15% increase in grid lifetime for a given thrust. The increase in beam profile

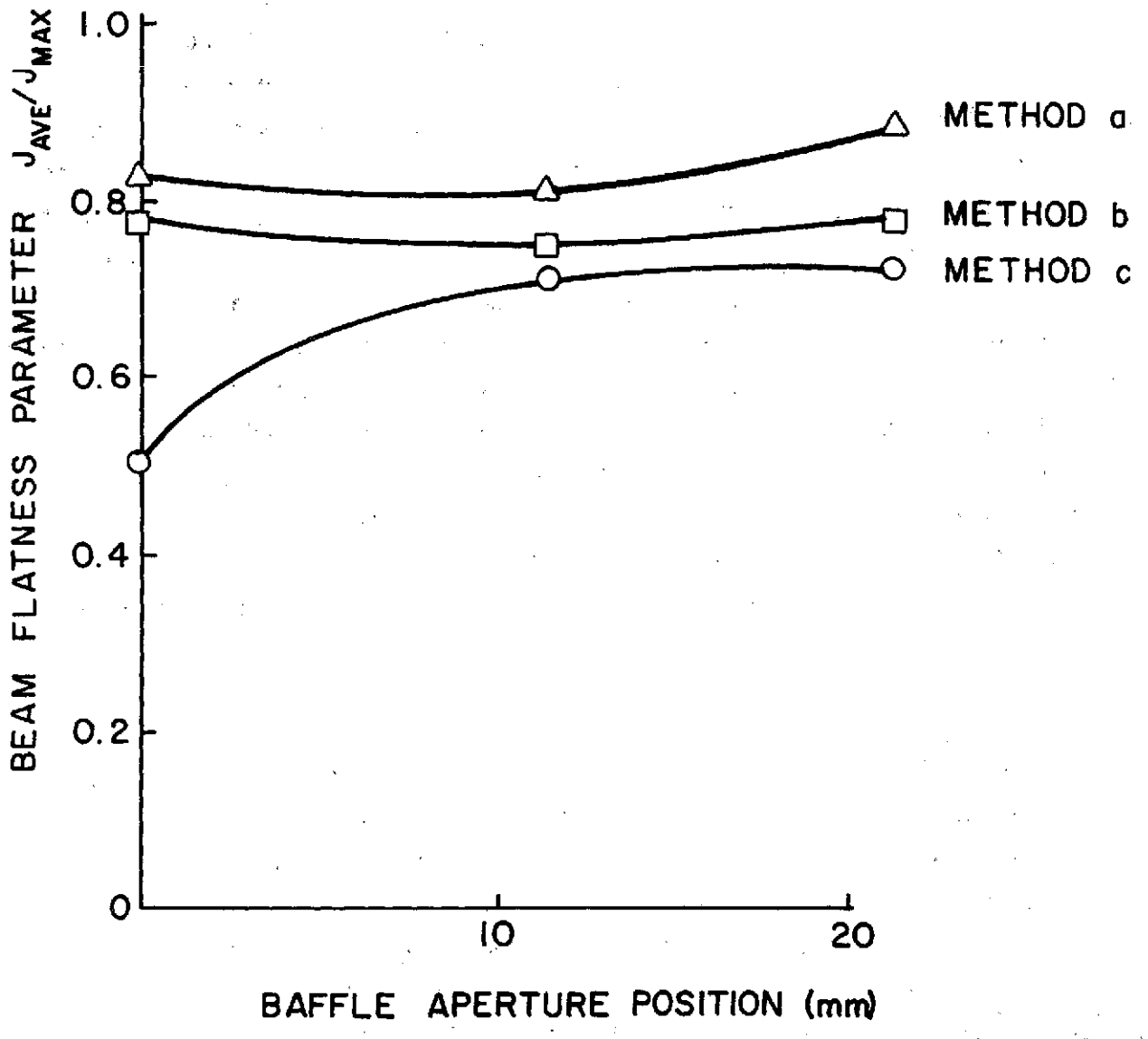


EXTRAPOLATED BEAM FLATNESS PARAMETERS

FIGURE 23

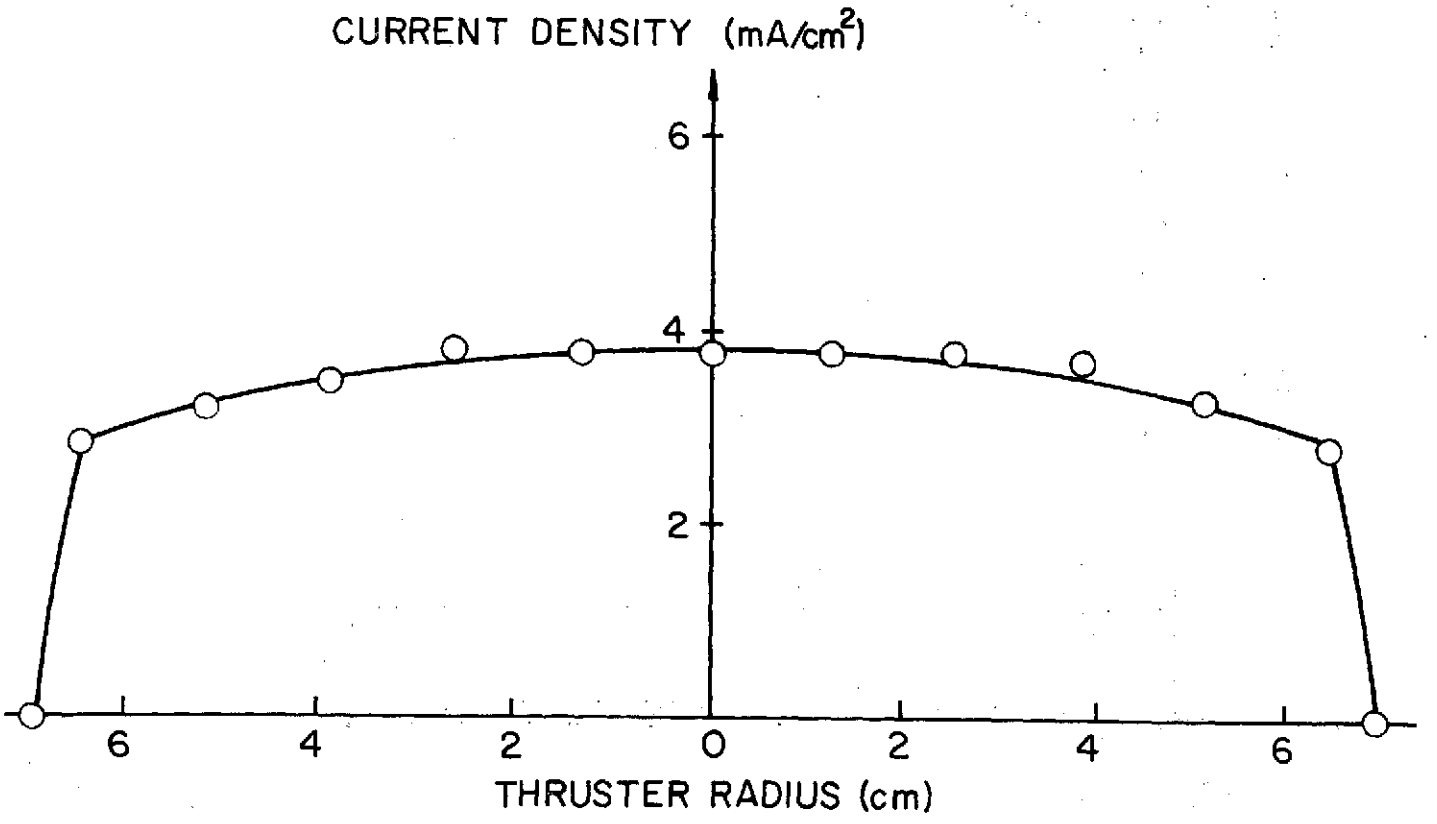


EXTRAPOLATED BEAM CURRENT DENSITY PROFILE

FIGURE 24

uniformity is due to an increase in neutral residence time at the thruster periphery and a reduction in the radial plasma density gradient at the screen grid resulting from the axial magnetic field being confined to the region close to the front anode. Extrapolation of beam profile data to determine the flatness parameter at the accelerator grid has been tried by several different procedures. Although the results are not always unique, each method determines flatness parameters which are typically greater than 0.7. The procedure considered most accurate gives flatness parameters at the accelerator grid as high as 0.9.

Decreasing the length to diameter ratio resulted in a baseline discharge loss reduction of 85 eV/ion. The baseline performance of the chamber having an L/D value of 0.3 was comparable to the SERT II thruster. Stable operation of all thruster configurations investigated was observed over a wide range of flow rate and propellant utilization. In some cases a propellant utilization efficiency in excess of 100% was calculated. This anomaly is attributed to the existence of double ions. However, the discharge chamber double ion content has not been measured at the present time.

# DOUBLE ION PRODUCTION IN MERCURY DISCHARGES

Ralph R. Peters

## Introduction

As a result of operation of an electrostatic thruster at conditions which yield good performance some mercury double ions are produced. These double ions are undesirable because they result in a thrust degradation and an increase in sputtering damage to the thruster discharge chamber. This section describes a theoretical model of the reactions occurring in a mercury discharge and is designed to facilitate an understanding of processes important to the production of single and double mercury ions and to show how variation of the plasma parameters affect the concentrations of these ions. With an understanding of how the different plasma parameters affect these two ion concentrations it should be possible to design and operate a thruster in such a way as to minimize the double ion concentration while maintaining an acceptable single ion concentration in the discharge chamber.

## Theoretical Model

The model used is an extension of that of Reference 4. It simplifies the reactions and conditions inside a thruster chamber by assuming uniform plasma properties over the discharge region and considering only the reactions shown in Figure 25. The symbols used in Figure 25 represent the following species:

$Hg^{o}$ -- neutral ground state mercury
$Hg^{m}$ -- metastable neutral mercury ($6^3P_0$ and $6^3P_2$ states)
$Hg^{r}$ -- resonance state neutral mercury ($6^3P_1$ and $6^1P_1$ states)
$Hg^{+}$ -- singly ionized ground state mercury
$Hg^{m+}$ -- singly ionized metastable mercury ($6^2D_{3/2}$ and $6^2D_{5/2}$ states)
$Hg^{++}$ -- doubly ionized ground state mercury

The intermediate resonance and metastable states used in the analysis were selected because they had significant electron impact cross sections over the electron energy range of interest. The cross sections for the reactions of Figure 25 are presented along with references indicating their origin in Figure 26. Where possible these cross sections were selected from published experimental data. If experimental data were not

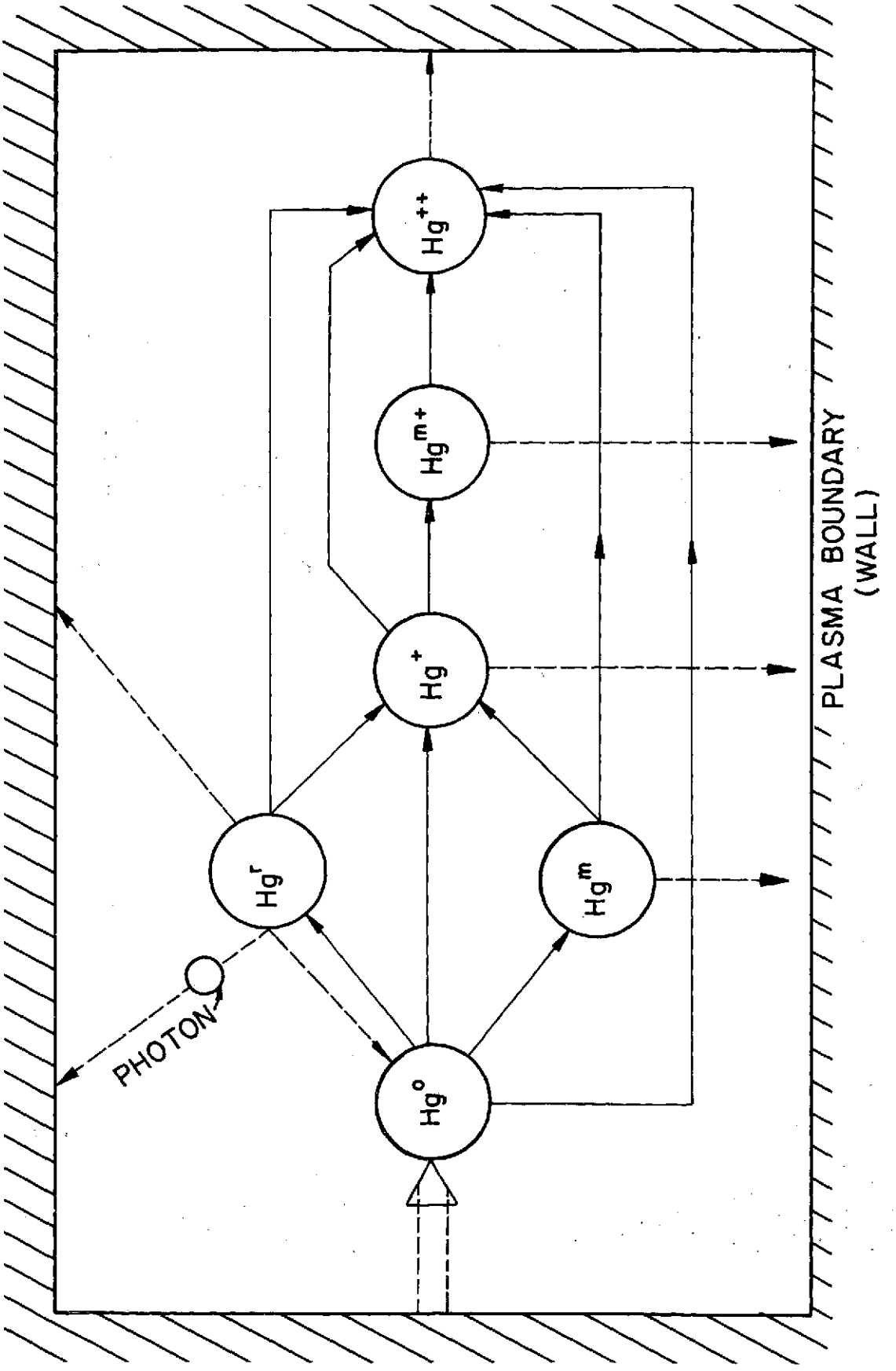


DOUBLE ION PRODUCTION SCHEMATIC

FIGURE 25

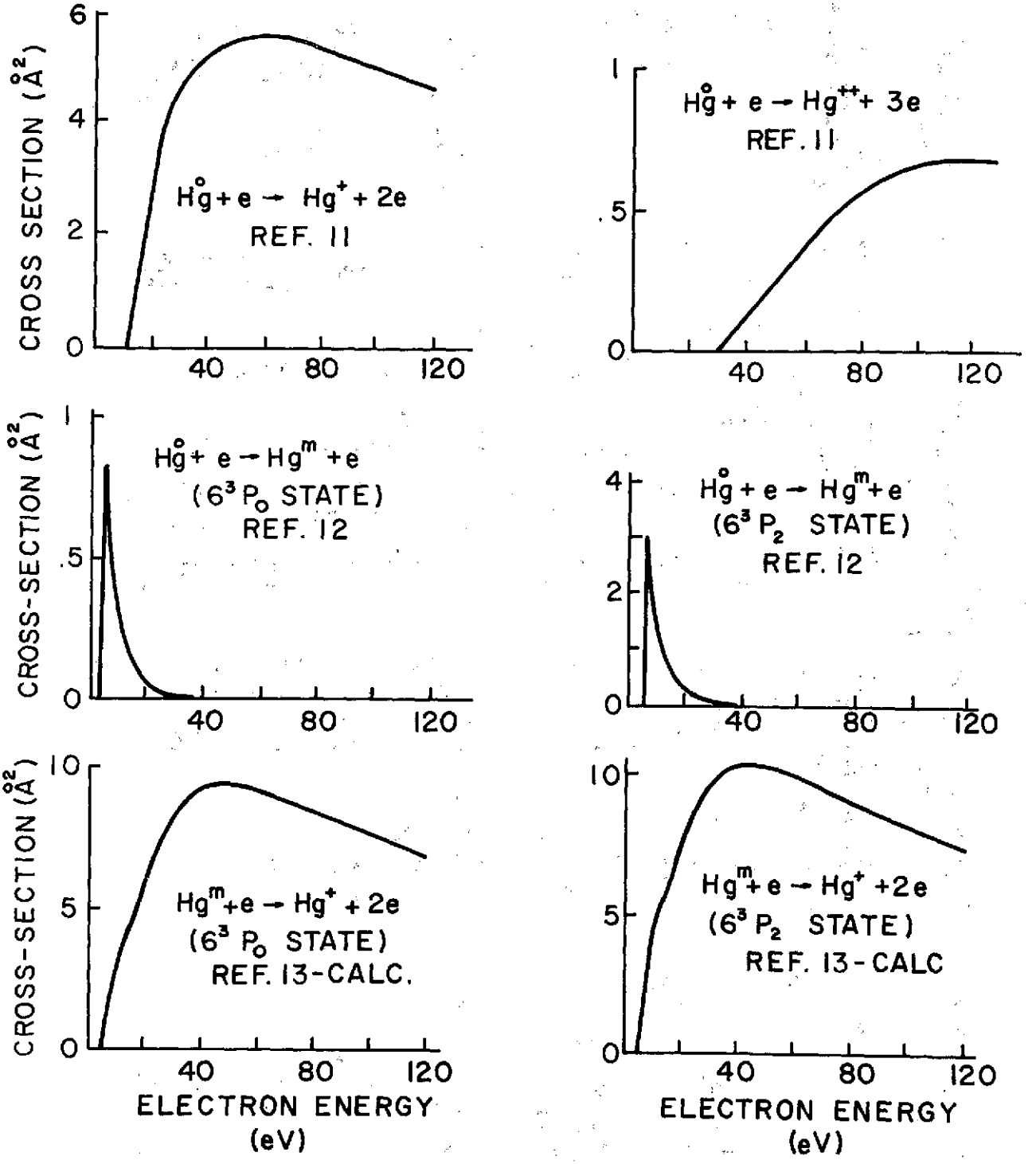


MERCURY CROSS SECTIONS

FIGURE 26

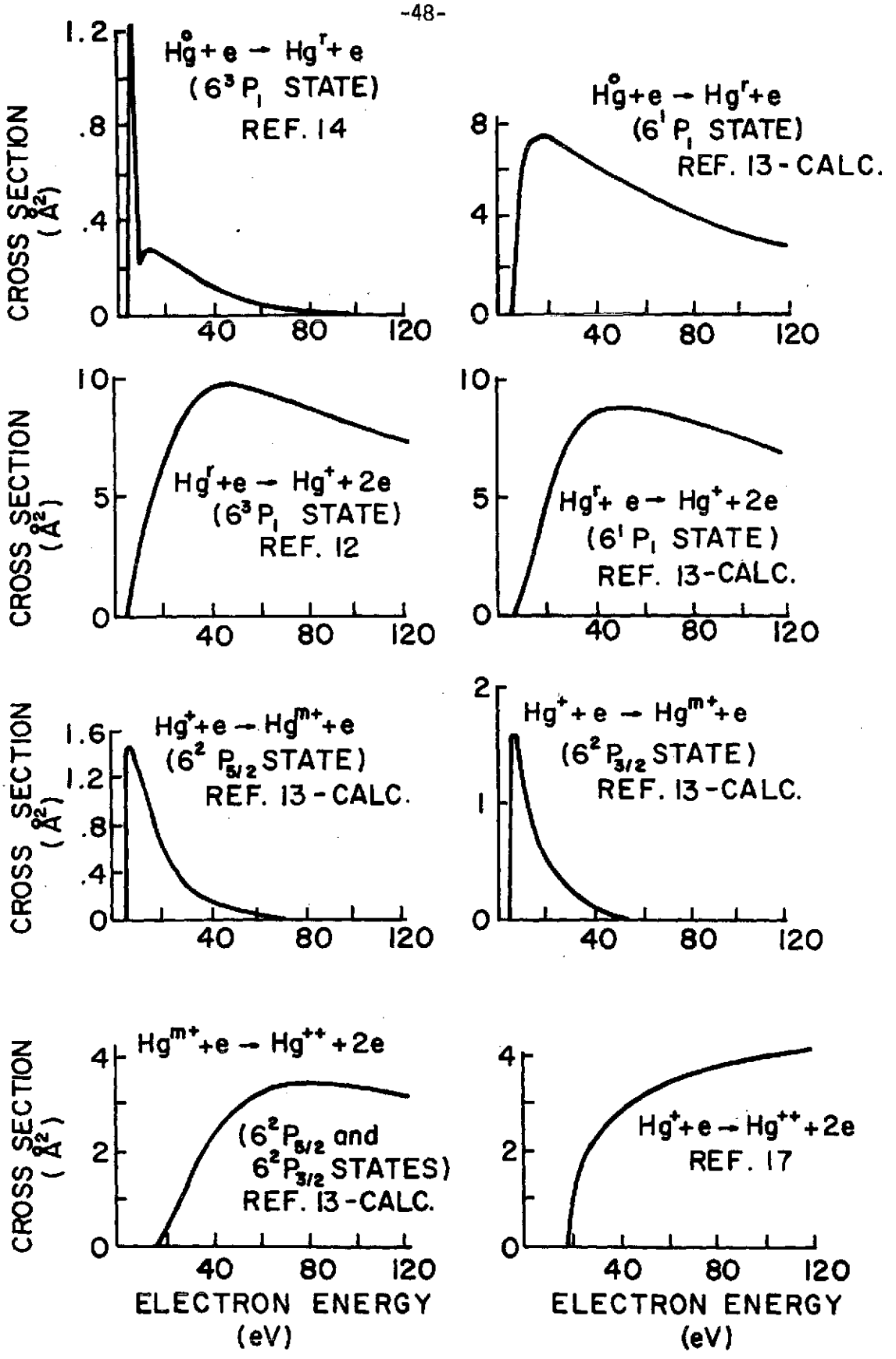


MERCURY CROSS SECTIONS

FIGURE 26 (cont.)

available the cross sections were calculated using the Gryzinski approximation[13], and curves so calculated are annotated to indicate this. The Gryzinski method was modified for the cases of metastable single ion production cross sections to reflect the significant value of these cross sections at threshold.

The arrows on Figure 25 show the various routes considered in this analysis. It shows for example that ground state single ions can be produced from neutral ground state, resonance state and metastable state atoms and that they can be lost as a result of single ion migration to the plasma boundary and production of metastable single ions and double ions. All reactions except those occurring at the plasma boundary are considered to be induced by electron bombardment, and the rate of production of any Specie $\gamma$ from Specie $\alpha$ (and hence loss rate of Specie $\alpha$ due to this reaction) is given by:

$$R_\alpha^\gamma = \int_{\text{all electron energies}} n_{Hg}^\alpha \; \sigma_\alpha^\gamma(E) \; V_e \; dn_e(E)$$

where $n_{Hg}^\alpha$ is the density of Specie $\alpha$, $\sigma_\alpha^\gamma(E)$ is the cross section for the production of $\gamma$ from $\alpha$ at energy E (velocity $V_e$), and $dn_e(E)$ is the density of electrons having energies between E and E + dE. The distribution of electrons over the energy spectrum of an ion thruster is assumed to be composed of a group with a Maxwellian distribution plus a monenergetic group (primary electrons) at a specified energy (primary energy). The Maxwellian electron group is described by the Maxwellian temperature ($T_e$ -- eV) and Maxwellian electron density ($n_m$ -- $m^{-3}$). The primary electrons are described by their energy ($\xi_p$ -- eV) and density ($n_p$ -- $m^{-3}$).

In going to the plasma boundary an atom or ion could be going to a discharge chamber wall in which case it would be neutralized and returned to the discharge or it could be going through a grid aperture in which case it would be extracted from the discharge. In either case this process represents a loss rate for any of the excited states. These reactions are indicated in Figure 25 by the dotted lines to the wall of the chamber and then a large arrow back to the neutral atomic state. The equation for the plasma boundary loss rate of a Specie $\alpha$ per unit volume is given by:

$$R_{\ell\alpha} = \frac{n_\alpha V_\alpha A}{\forall} = \frac{n_\alpha V_\alpha}{\forall/A} \tag{6}$$

where $n_\alpha$ is the density of Specie A, $V_\alpha$ is its average velocity toward the plasma boundary, A is the surface area of this boundary, and $\forall$ is its volume. For neutral particles the average velocity toward the boundary is equal to one-fourth of the thermal velocity. For charged particles the velocity is determined by the Bohm criterion[15,4] with

$$V_\alpha = \sqrt{\frac{T_e q}{m_i}\ (1 + n_p/n_m)} \tag{7}$$

where q is the ion charge (coul) for $T_e$ in eV and $m_i$, the ion mass, in kg.

The equation for the loss rate was written in the second form to show the origin of the plasma parameter $\forall/A$ which appears in the results. If this parameter is large an ion or excited neutral must, on the average, travel great distances to reach the plasma boundary, and therefore the loss rate of these species to the boundary per unit volume is small. If $\forall/A$ is small the ions and atoms are all very near to the boundary and this allows them to reach it quickly causing a large loss rate per unit volume.

A third type of reaction shown in Figure 25 is relevant only to the two resonance states. The resonance states differ from metastable states in that they have very short lifetimes and they de-excite spontaneously shortly after formation by emitting a photon of light. The energy of this photon is such that it is readily reabsorbed by a nearby neutral ground state atom in a resonance absorption reaction which produces another resonance state atom. Eventually the photon can diffuse to a boundary where it is lost and hence in effect a resonance state atom is lost. This loss mechanism is represented in Figure 25 by a line conveying a photon to the boundary and a branching line going from the resonance atom to the neutral ground state atom. From diffusion theory the rate of photon loss across any plasma boundary is given by the equation:

$$R_{\ell r} = D \nabla n_n \Big|_{\text{evaluated at the boundary}} \tag{8}$$

where $n_n$ is the photon density, D is the diffusion coefficient $\left(\frac{1}{3\tau(n_o\sigma_c)^2}\right)$

$\tau$ is the average lifetime of the resonant state, $n_o$ is the density of neutral ground state atoms and $\sigma_c$ is the cross section for absorption of photons by neutral ground state atoms[16].

One can approximate the actual distribution by the approximate linear distribution shown in Figure 27. This yields the following conservative estimate for resonance state atom loss

$$R_{\ell r} = D \nabla n_n \simeq D \frac{\Delta n_n}{\Delta S} = \frac{D n_n}{\ell_F} \tag{9}$$

where $\ell_F$ is the mean free path for photon absorption $(\frac{1}{n_o \sigma_c})$. This approximation is valid when the photon mean free path is much less than the characteristic dimension of the plasma, a condition that is readily satisfied for this case where the photon mean free path is very small.

Since the neutral density is uniform over the discharge region the photon density profile is similar to the resonant atom density profile and the following approximation between photon and resonant atom density at any location in the plasma applies:

$$n_n = n_r \beta \tag{10}$$

where $\beta$ is a constant equal to the photon to resonance atom density ratio. The constant $\beta$ is also equal to the ratio of photon lifetime $(1/c\, n_o\, \sigma_c)$ to resonance atom lifetime $(\tau)$ and is therefore given by:

$$\beta = \frac{1}{c\tau\, n_o\, \sigma_c} \tag{11}$$

where c is the speed of light and the other quantities have already been defined. Combining equations 9, 10 and 11 one obtains an equation for the loss rate of photons and hence of resonance atoms due to photon diffusion:

$$R_{\ell_r} = \frac{n_r}{3c} \left(\frac{1}{\tau\, n_o\, \sigma_c}\right)^2 \tag{12}$$

The steady state density of any specie can be calculated now by equating the total production rate to the total loss rate of that specie. The $6^3P_o$ metastable atom density is determined for example by equating the

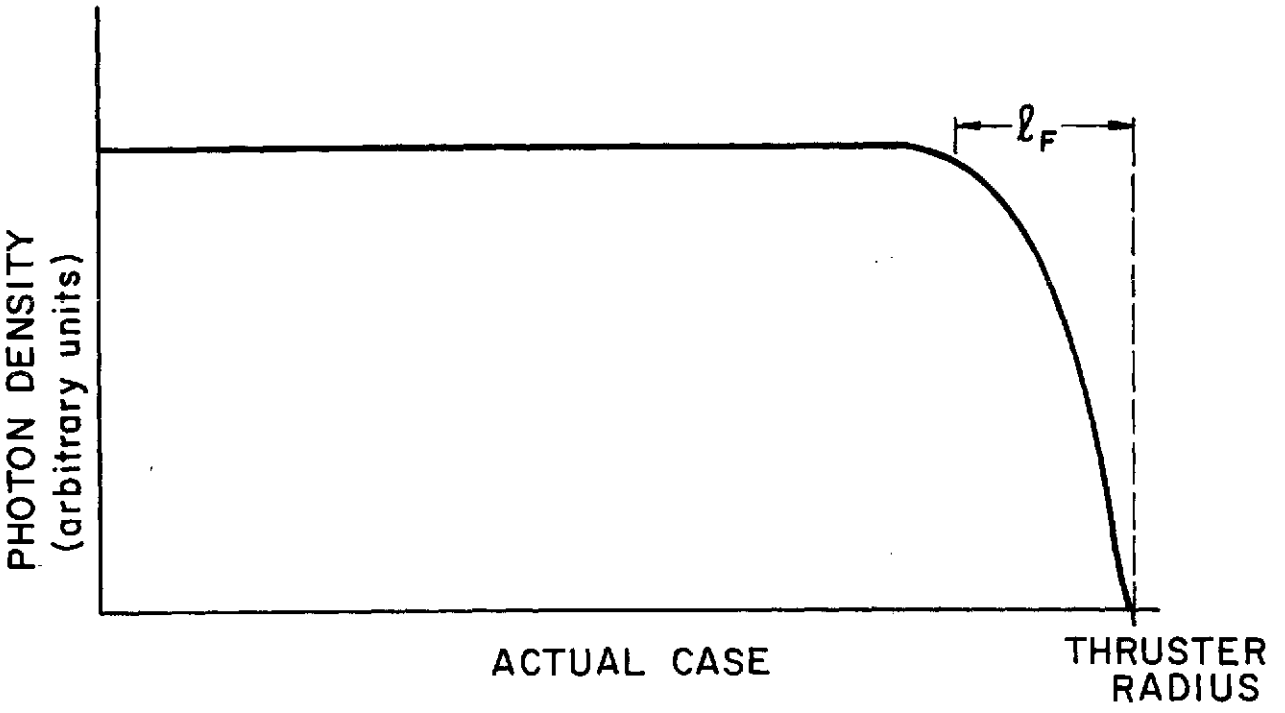


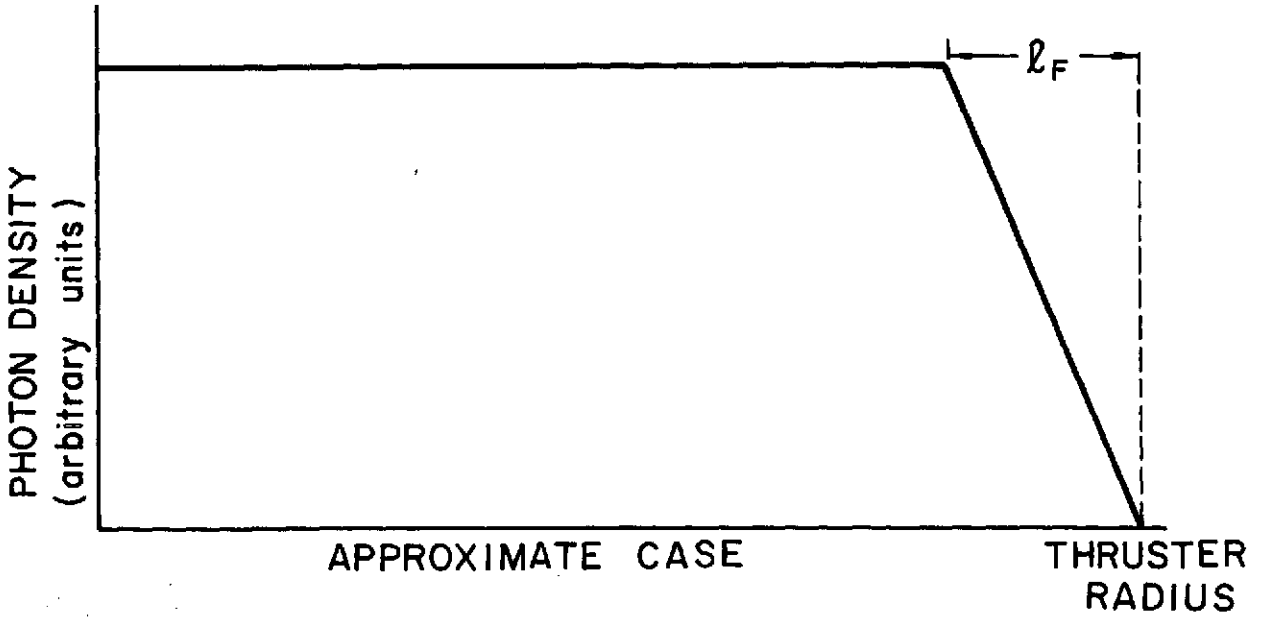


PHOTON DENSITY PROFILES

FIGURE 27

the production rate of these metastable atoms from neutral ground state mercury atoms to the sum of loss rates due to 1) metastable migration to the walls, 2) production of single ions from metastable neutrals, and 3) production of double ions from metastable neutrals. That is:

$$\int_E^{n_o} \sigma_o^m V_e dn_e = \frac{V_o n_{m^*}}{\Psi/A} + \int_E^{n_{m^*}} \sigma_m^+ V_e dn_e + \int_E^{n_{m^*}} \sigma_m^{++} V_e dn_e \,. \tag{13}$$

One can manipulate this to yield

$$\frac{n_{m^*}}{n_o} = \frac{\int_E \sigma_o^m V_e dn_e}{\frac{V_o}{\Psi/A} + \int_E \sigma_m^+ V_e dn_e + \int_E \sigma_m^{++} V_e dn_e} \,. \tag{14}$$

Using this equation together with the cross sections of Figure 26 the ratio of $6^3P_o$ metastable to neutral ground state densities can be calculated for specified values of primary electron density and energy, Maxwellian electron density and temperature and the volume to surface area ratio of the plasma discharge region. Equations similar to (14) for other species can also be obtained and solved. Since electron density was specified to solve the problem and since charge neutrality is required, a conservation of charge equation can be written. This equation and equations similar to (14) for single and double ion to neutral atom density ratios can then be solved simultaneously for the neutral atom density. Once this is known the densities of each of the other species can be determined. It should be mentioned that some iteration is required because the resonance state loss rate due to photon diffusion (Equation 12) is dependent on ground state neutral atom density.

Results

The equations for the ratios of the various excited state densities to the neutral ground state density were solved using a computer to integrate the product of the cross section and the electron density as a function of energy numerically. Table III shows results obtained for the volume to area ratio of a 30 cm diameter thruster and at the typical plasma

TABLE III

Relative Concentration of the Various Species in Ion Thruster Plasma and their Production and Loss Paths

Plasma Parameter

$\frac{\text{Plasma Volume}}{\text{Surface Area}} \equiv \forall/A = .033$ m

Maxwellian Electron Temperature = $T_e = 5$ eV

Electron Density $\equiv n_e = 3 \times 10^{17}$ m$^{-3}$

$\frac{\text{Primary Electron density}}{\text{Maxwellian Electron density}} \equiv n_p/n_m = 0.1$

Primary Electron Energy $\equiv \xi_p = 35$ eV

| | | |
|---|---|---|
| **Neutral Metastable States** | | |
| $6^3P_0$ state | $\frac{\text{Metastable atom density}}{\text{Ground state atom density}}$ | = 5.5% |
| Production: | From Neutral Ground State | 100% |
| Losses: | To the plasma boundary | 7.0% |
| | Converted into $Hg^+$ ion | 92.7% |
| | Converted into $Hg^{++}$ ion | .3% |
| | | 100.0% |
| $6^3P_2$ state | $\frac{\text{Metastable atom density}}{\text{Ground state atom density}}$ | = 5.8% |
| Production: | From Neutral Ground State | 100% |
| Losses: | To the plasma boundary | 7.0% |
| | Converted into $Hg^+_{++}$ | 92.7% |
| | Converted into Hg | .3% |
| | | 100.0% |
| **Neutral Resonance States** | | |
| $6^3P_1$ state | $\frac{\text{Resonance atom density}}{\text{Ground state atom density}}$ | = 5.0% |
| Photon mean free path = 2.66 cm | | |
| Production: | From neutral ground state | 100% |
| Losses: | To the plasma boundary | 7.6% |
| | Via Photon diffusion | 8.9% |
| | Converted to $Hg^+$ | 83.2% |
| | Converted to $Hg^{++}$ | .3% |
| | | 100.0% |
| $6^1P_1$ state | $\frac{\text{Resonance atom density}}{\text{Ground state atom density}}$ | = 65% |
| Photon mean free path = .083 cm | | |
| Production: | From neutral ground state | 100% |
| Losses: | To the plasma boundary | 5.9% |
| | Photon losses | 46.1% |
| | Converted to $Hg^+$ | 47.8% |
| | Converted to $Hg^{++}$ | .2% |
| | | 100.0% |

| | | |
|---|---|---|
| **$Hg^+$ ionic state** | | |
| | $\frac{\text{Single ion density}}{\text{Ground state atom density}}$ | = 38.9% |
| Production: | From neutral ground state | 35.6% |
| | From neutral metastable states | 20.1% |
| | From neutral resonance states | 44.3% |
| Losses: | To the plasma boundary | 83.2% |
| | Converted to ionic metastable states | 11.3% |
| | Converted to $Hg^{++}$ | 5.5% |
| | | 100.0% |
| **Ionic Metastable states** | | |
| $6^2D_{5/2}$ state | $\frac{\text{Metastable ion density}}{\text{Ground state atom density}}$ | = 2.9% |
| Production: | From $Hg^+$ ion | 100% |
| Losses: | To the plasma boundary | 96.1% |
| | Converted into $Hg^{++}$ | 3.9% |
| $6^2D_{3/2}$ state | $\frac{\text{Metastable ion density}}{\text{Ground state atom density}}$ | = 2.2% |
| Production: | From $Hg^+$ ions | 100% |
| Losses: | To the plasma boundary | 96.1% |
| | Converted into $Hg^{++}$ | 3.9% |
| **$Hg^{++}$ ionic state** | $\frac{\text{Double ion density}}{\text{Ground state atom density}}$ | = .022 |
| Production: | From neutral ground state | 4.6% |
| | From neutral metastable states | 1.0% |
| | From neutral resonance states | 3.2% |
| | From $Hg^+$ ionic state | 84.5% |
| | From ionic metastable states | 6.7% |
| | | 100.0% |
| Losses: | To the plasma boundary | 100% |

conditions listed at the top of the table. The table shows the relative densities of each of the species in the plasma. It also indicates what percentage of the total production of a given specie comes from each of the possible routes and what percentage of the total loss of that specie goes out through each of the possible routes. For example 100% of the $6^3P_0$ neutral metastable atoms come from electron bombardment of neutral ground state atoms and 92.7% of these metastables are subsequently converted to singly charged ground state mercury ions.

Several observations can be made from the data of Table III. These include the fact that a relatively large number of neutrals exist in the $6^1P_1$ resonance state which has a density that is about 65% of the neutral ground state atom density. This occurs because this resonance state has a large production cross section and a relatively low velocity toward the walls which results in a very small wall loss rate. This resonance state is a significant source of single ions because of its large density and rather large cross section for production of single ions at energies in the range where there are high Maxwellian electron densities. The neutral metastable states with their lower densities yield a proportionately smaller contribution to the production of single ions.

One important point should be made about the ratio of single ions to neutral ground state atoms, which at first glance seems large (38.9%). When one measures the ratio of single ions to neutral atoms in a thruster the quantity "neutral atoms" includes resonance, metastable and ground state neutral atoms. If the ratio of single ions to all neutral atoms is calculated one obtains the more logical value of 20%. The data on single ions and that on neutral atoms shows the loss rate to the plasma boundary is a much larger fraction for the ionic states. This occurs because the velocity for a single ion (determined by the Bohm criterion) is approximately 7 times the average velocity of a neutral atom (thermal) toward the boundary.

Table III also shows that the majority of double ions are produced from single ions ($\sim$ 85% in this case). The production of double ions via a two step process including the single ionic state appears to dominate in general because of the large cross section for production of double ions from this intermediate state. This indicates to the designer that the large single

ion densities required for proper thruster operation will invariably result in significant double ion densities. Figure 28, presents the variations in total neutral density (including resonance and mestastable states) to single ion density ratio as a function of the various parameters of the problem, and Figures 29 and 30 show the variations in double ion density to single ion density ratio as a function of these parameters. The single ion density has been used to normalize the neutral and double ion densities in these figures because each curve corresponds to a constant electron density which implies an approximately constant single ion density for low double ion concentrations.

Figure 28 shows how neutral density in a discharge chamber must vary to produce a given single ion density as the primary electron energy and other parameters are varied. The curve labelled $\forall/A$ = 0.0166 m corresponds to a smaller (15 cm diam.) thruster and shows the need for higher neutral densities to sustain a specified single ion density. This result can be understood if one remembers that a low value of volume to surface area ratio ($\forall/A$) implies a high loss rate of single ions per unit volume, thus necessitating a higher production rate. For a given set of plasma conditions this higher production rate can be achieved only by increasing the neutral atom density.

The shape and placement of the other curves result from the shape of cross sections for production of single ions. As the electron energy increases the cross sections generally increase. Therefore if one increases the number of high energy electrons (curves where $n_p/n_m$ = 0.15 and $T_e$ = 7.5 eV) the number of neutral atoms required to produce a given number of ions is reduced. Since a high single ion to neutral atom ratio implies a high propellant utilization these curves indicate increases in the values of all the plasma parameters effect improved propellant utilization.

Figure 29 shows the variation of the ratio of double ions to single ions with primary electron energy for various values of the parameters of the problem. Comparison of the curve where $\forall/A$ = .0166 m and the standard curve shows the double ion concentration might be expected to almost double as the volume to surface area of a thruster is doubled. The reason for the difference in these two curves can best be understood by recalling the possible reactions presented in Figure 25. There is a high probability

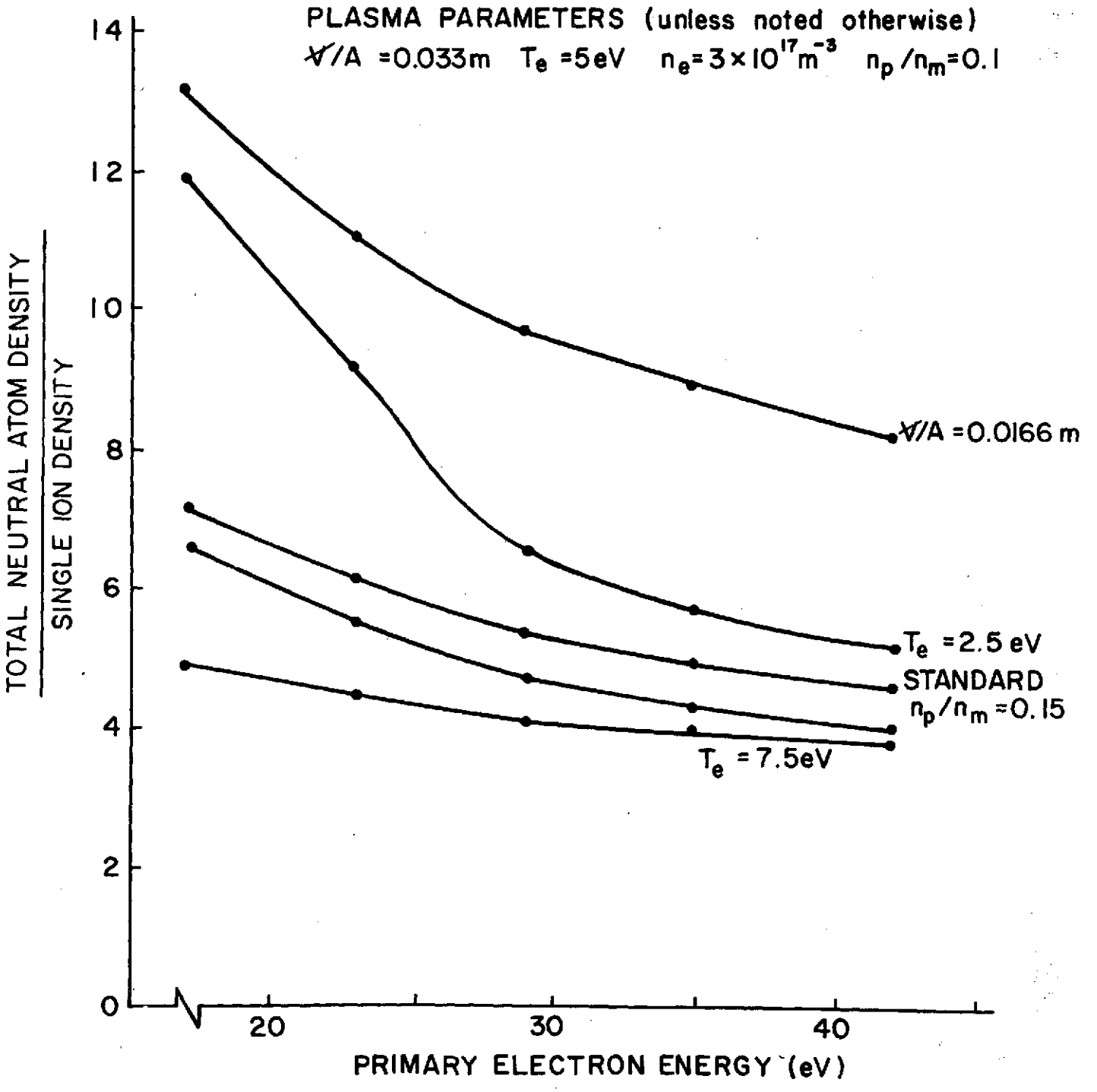


EFFECT OF PLASMA PROPERTIES ON NEUTRAL TO SINGLE ION DENSITY RATIO

FIGURE 28

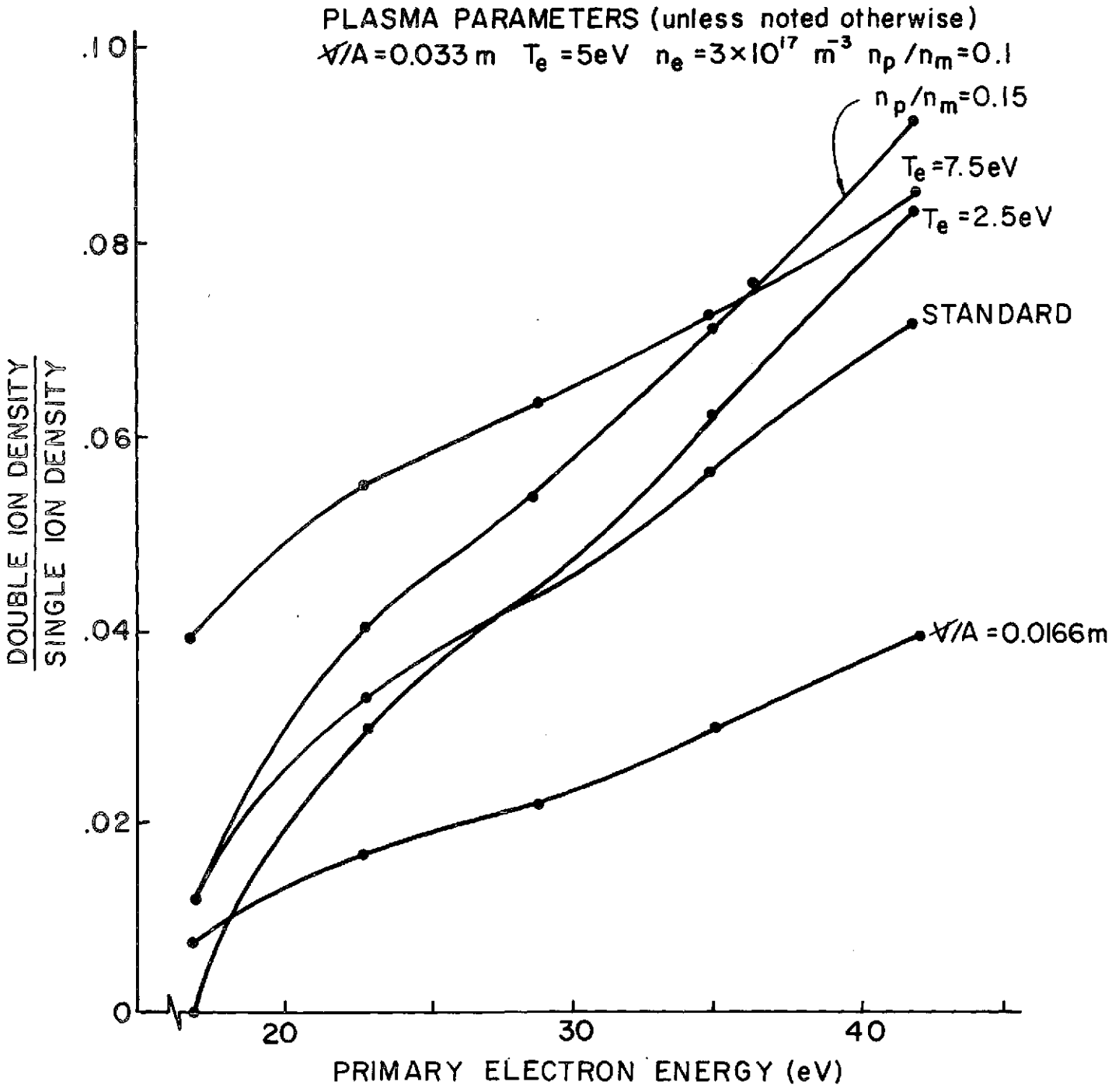


EFFECT OF PLASMA PROPERTIES ON DOUBLE TO SINGLE ION DENSITY RATIO

FIGURE 29

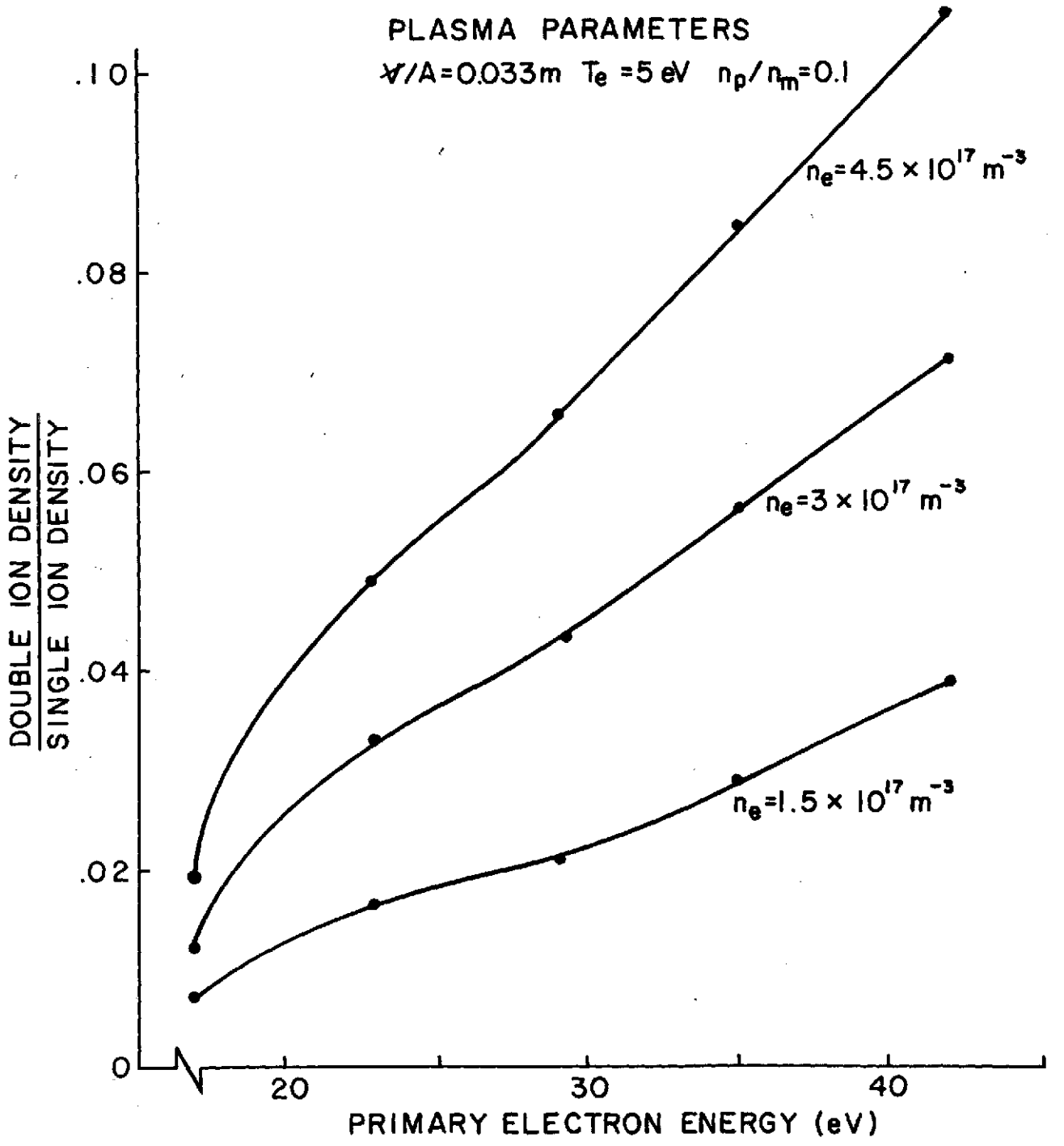


EFFECT OF ELECTRON DENSITY ON DOUBLE TO SINGLE ION DENSITY RATIO

FIGURE 30

that a single ion will go to the plasma boundary and recombine or be extracted rather than becoming doubly ionized. If the volume to surface area of the discharge chamber is decreased the loss rate of double ions to the boundary increases and at the same time the probability of single ions reaching a boundary increases and so the rate of production of double ions decreases. These two effects act together to cause a decrease in the steady state density ratio of double to single ions as the size of a discharge chamber is reduced.

The two curves in Figure 29 for which electron temperature was varied from the standard condition show an unexpected cross-over behavior. For an electron temperature of 7.5 eV the double ion density is quite high over the primary electron energy range because of the significant number of electrons in the Maxwellian "tail" which can ionize single ions to form double ions. In comparison when the electron temperature is 2.5 eV, there are fewer high energy Maxwellian electrons and at primary electron energies below the threshold for double ion production very few double ions are formed. The greater slope of the 2.5 eV electron temperature curve is caused by the lower loss rate of double ions which is proportional to the square root of electron temperature. This lower wall loss rate causes the double ion concentration to rise quickly as primary electron energy increases. Increasing the primary to Maxwellian electron density ratio effects the expected increase in double ion fraction as primary energy increases because there are more primary electrons available to create double ions.

The curves in Figure 30 show the ratio of double to single ions increases as the magnitude of the electron and hence ion density increases. This result can be explained by recognizing most double ions are produced by electron bombardment of single ions. The rate of production of double ions is then given approximately by:

$$R_+^{++} \simeq n_p\, n_+\, \sigma_+^{++}(\xi_p) + \int_E n_+\, \sigma_+^{++}\, V_m\, dn_m$$
$$\simeq n_e^2 \left\{ \frac{n_p}{n_e}\, \sigma_+^{++}(\xi_p) + \frac{n_m}{n_e} \int_E \sigma_+^{++}\, f(E)\, V_e\, dE \right\} \qquad (15)$$

where f(E) is the Maxwellian distribution function. The loss rate of double ions is given by:

$$R_{\ell ++} = \frac{n_{++} V_{++}}{\Psi/A} \tag{16}$$

which can be equated to Equation (15) to yield the following approximate result:

$$\frac{n_{++}}{n_+} \approx \frac{n_{++}}{n_e} = n_e \left\{ \frac{\Psi}{AV_{++}} \left[ \left( \frac{n_p}{n_e} \right) V_p \sigma_+^{++} + \frac{n_m}{n_e} \int \sigma_+^{++} f(E) V_m dE \right] \right\} \tag{17}$$

The terms in the brackets of Equation (17) are not functions of electron density so the double to single ion density ratio is seen to be directly proportional to the electron density.

Conclusions

Double ions are produced in mercury ion thruster discharge chambers primarily as a result of a two-step process involving the single ionic state as the intermediate step. Metastable and resonance states do not contribute directly in any significant way to the production of double ions except as the contribute to the production of singly charged ions. The $6^1P_1$ resonance state should become heavily populated under thruster operating conditions and this should represent an important intermediate step for the production singly charged ions. The ratio of double ion density to single ion density should almost double as the volume to surface area ratio of the discharge chamber is doubled and this ratio should also increase almost linearly with single ion density in the discharge chamber.

# OBSERVATIONS OF AN OPERATING HOLLOW CATHODE

James E. Graf

## Introduction

Much work has been conducted on the physical characteristics of an operating ion thruster and its components. In particular, the hollow cathode has been examined to determine the effects of cathode temperature and mass flow rate on voltage-current characteristics of the keeper and arc discharges. The effect of low work function materials in the cathode has been considered but there is little understanding of the actual electron emission mechanism or the role that the dual alkaline-carbonate coating (R-500)* plays in cathode operation.

In an attempt to understand these areas better, an experiment was conducted in which the interior of an operating hollow cathode was monitored photographically over a range of operating conditions. The photographic equipment used included two types of motion picture cameras--high speed (up to 5000 frames/sec) and normal speed (24 frames/sec), a streak camera (up to 1500 inches/sec) and a 35 mm still camera which could be fitted with various filters. These filters, which passed only radiation from a selected frequency band, were used to determine the location and effects of the various materials in the cathode.

It was hoped that this study would facilitate an understanding of the electron emission mechanism which could include simple thermionic emission, field enhanced thermionic emission and/or a mechanism wherein metastable mercury atoms collide with the low work-function alkaline oxide molecules causing them to emit an electron. Each of these mechanisms could be enhanced by a cathode spot - a small region of intense heating and hence high temperature which generally moves rapidly over the cathode face or cathode insert. The spot has been observed in the mercury arc of electron tubes but has not, up to this point, been observed in ion thruster hollow cathodes.

---

* J. T. Baker Chemical Co., Phillipsburg, New Jersey

The low work-function carbonate (emissive mix) coating supplied to most thruster cathodes contains $BaCO_3$ and $SrCO_3$ which after activation of the cathode are converted to BaO and SrO. At high preheat temperatures and after discharge initiation, the coating will sublimate to a vapor containing BaO, $BaO_2$, and to a lesser extent Sr-SrO has not been observed[18,19]. Although the exact role of this vapor is not known it has been suggested that it will:

1) Interact in the plasma itself, i.e. with the electrons and mercury atoms, ions and metastables and
2) Condense on the cathode surfaces creating a larger area covered with a low work-function material.

If the extent of low work-function surface is extended then there is greater area on which thermionic, field enhanced thermionic and mercury metastable emission mechanisms could operate. The region could also extend onto the backface of the cathode orifice plate which may be a more favorable emission location because of its proximity to the cathode orifice. Evidences of coating migration and coating interactions in the plasma were therefore also sought in the study.

Procedure

The apparatus used in this experiment consisted of a 6.4 mm dia. hollow cathode equipped with a 0.16 mm thick by 1.27 cm diameter quartz window. It was through this window located at the end of the cathode opposite the cathode orifice plate that the insert and back of the orifice plate were photographed (Figure 31). Flow through the cathode orifice was regulated by controlling the current to a standard SERT II vaporizer. The keeper was a wire loop positioned 1.5 mm from the cathode tip. The anode was movable and was generally positioned two to five cm from the cathode orifice plate. Three series of tests were run, the first employing a clean rolled tantalum foil insert inside a virgin cathode, the second using an emissive mix (R-500) coated rolled tantalum foil insert, and the third using a sintered tungsten, carbonate impregnated insert. During each test arc currents, keeper currents and cathode flow rates were controlled over a range of values and still photographs were taken at each operating conditions. High speed and streak photographs were taken at nominal operating conditions for each configuration.

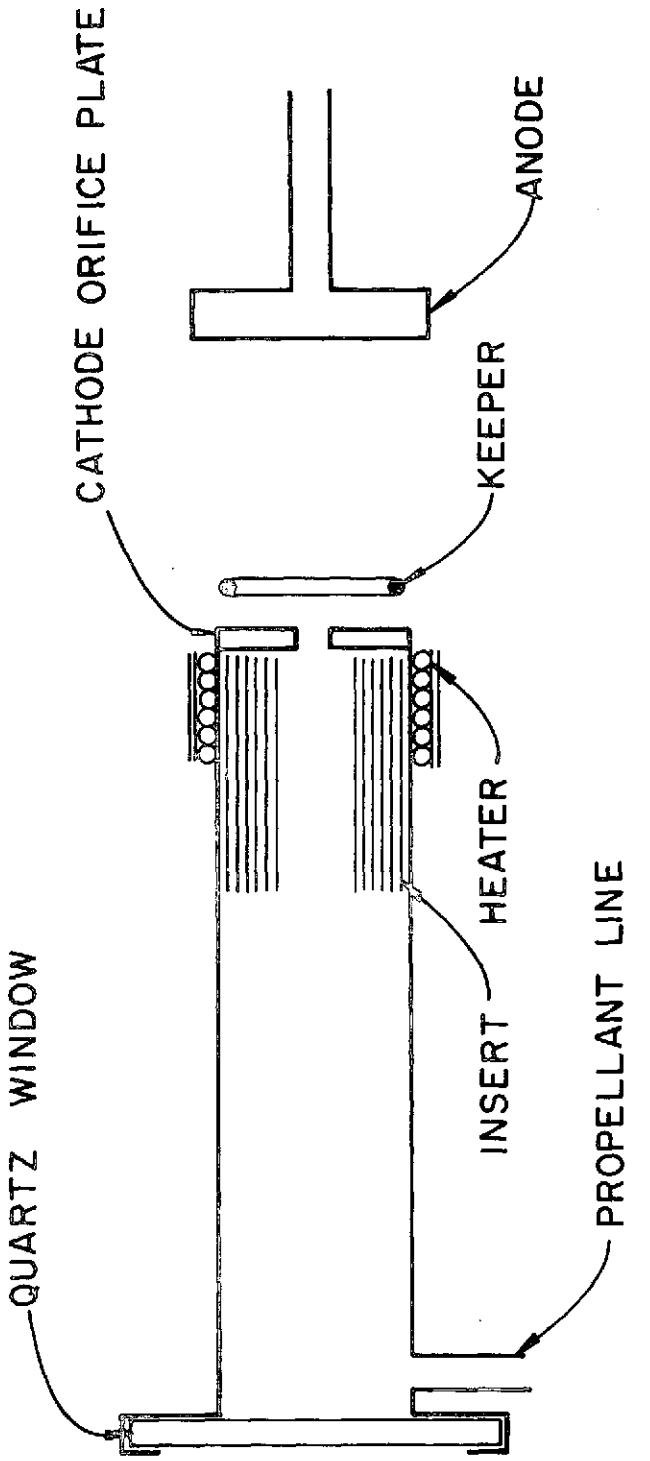


SCHEMATIC OF HOLLOW CATHODE MODIFIED FOR OBSERVATION

FIGURE 31

Results

The photographic study showed that a region of intense luminosity which could be referred to as a cathode spot did exist in cathodes free from any emissive mix. The spot was stationary, affixing itself to a metal protrusion from the rolled foil insert or the cathode tip back face into the cathode plasma. After operation for a period of time with the spot at one location it would move to a different position in the cathode. At different times the spot was observed at the following locations: 1) on the back face of the cathode orifice plate, 2) on the insert at a location near the orifice plate and 3) on the insert at the upstream end of the cathode. Figure 32A is a photograph of the interior of the cathode showing the cathode orifice and a spot on the back face of the orifice plate. The spot is positioned on a metal protrusion which apparently was created during manufacture. Figure 32B is a photograph which shows the spot attached to the rolled foil insert close to the orifice plate and Figure 32C shows it again on the insert but upstream away from the orifice plate. These photographs were taken at the different conditions indicated in Table IV through neutral density filters. Of particular significance it appears is the high keeper voltage (338 V) associated with operation when the spot was attached to the back of the orifice plate (Figure 32A). This suggests a significant emission area must be presented to realize acceptably low operating voltages. The movement of the spot between the locations of Figures 32A, B and C was not rapid and at no time was a constantly moving spot observed with streak, high speed or low speed motion pictures. The spot would frequently remain in one position for days of intermittent running and only a change to a different insert would bring about a relocation of the spot.

Figure 32D is a photograph of the cathode shown in Figure 32C operating at the same conditions as those of Figure 32C but taken through a dark red (Tiffen 29) filter. Since mercury does not have strong lines radiating in the red and the filter stops the characteristic blue-violet radiation of the mercury, Figure 32D shows metal surfaces within the cathode that are sufficiently hot to radiate in the red. Comparison of Figures 32C and D shows very little red radiation from the cathode orifice and the outside edge of the orifice plate. This rather substantial red radiation

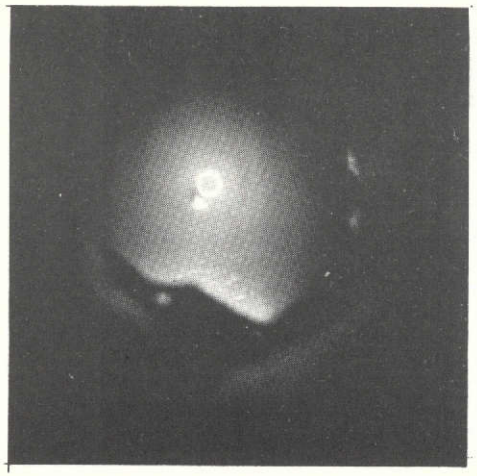

A. VIRGIN FOIL INSERT – NEUT. DENSITY FILTER

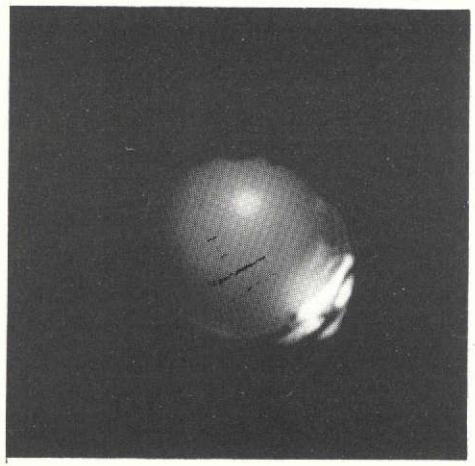

B. VIRGIN FOIL INSERT – NEUT. DENSITY FILTER

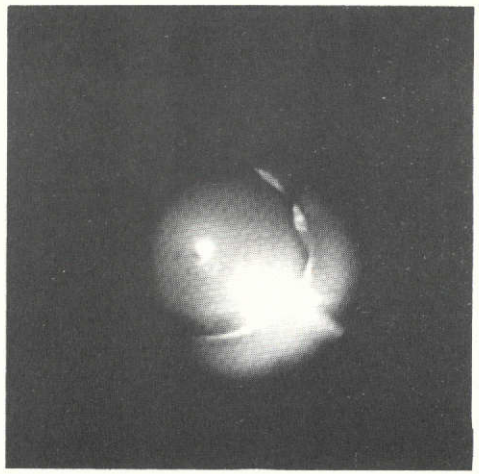

C. VIRGIN FOIL INSERT – NEUT. DENSITY FILTER

D. VIRGIN FOIL INSERT – RED FILTER

HOLLOW CATHODE FREE OF R-500 DURING OPERATION

FIGURE 32

TABLE IV

| Figure | Orifice Plate Temperature (°C) | Keeper Current (A) | Keeper Voltage (V) | Arc Current (A) | Arc Voltage (V) | Mercury Flow Rate (mA) | Camera Lens Opening | Shutter Speed (sec) | Filter | Emissive Mix |
|---|---|---|---|---|---|---|---|---|---|---|
| 32A | 1010 | 0.3 | 338 | 0.8 | 70 | 132 | f 22 | 1/125 | 1% neut. dens. | None |
| 32B | 1120 | 0.3 | 20 | 1.95 | 25 | >340 | f 8 | 1/30 | 0.1% neut. dens. | None |
| 32C | 815 | 0.3 | 19 | 1.5 | 42 | 420 | f 22 | 1/60 | 1% neut. dens. | None |
| 32D | 815 | 0.3 | 19 | 1.5 | 42 | 420 | f 22 | 1/125 | Red (Geletin #29) | None |
| 33A | 915 | 0.3 | 11 | 0.9 | 57 | 141 | f 8 | 1/60 | 1% neut dens. | R-500 |
| 33B | -- | 0.3 | 9 | 1.5 | 40 | -- | f 8 | 1/60 | 1% neut dens. | R-500 |
| 33C | -- | 0.3 | 9 | 1.5 | 40 | -- | f 8 | 1/30 | Red (Geletin #29) | R-500 |
| 33D | 830 | 0.3 | 15 | 1.0 | 87 | 141 | f 8 | 1/60 | 1% neut dens. | R-500 |

from the region of the cathode spot at the upstream end of the cathode insert implies high temperatures at this location.

Although Figures 32A, B and C exhibit a bluish color typical of mercury atom excitation near the cathode tip, the color of light which predominated the window end was not one of blue but of a whitish-cream color. The color was much like the incandescent light emitted by mercury vapor lamps. This light appeared different from light emitted from a cathode supplied with an emissive mix coated insert which had a more uniform blue cast to it.

In order to demonstrate the roll of the emissive mix in thruster operation a virgin cathode like the one shown in Figure 32 was after the initial set of tests, treated with chemical R-500 by simply adding a few drops to the insert. Since the cathode, which was installed with its axis parallel to the earth's surface, was not removed to add the mix, this material coated only the lower part of the insert. Upon initiation a spot was observed where the emissive mix had been added and not where it had been located before the mix was added. The spot, which was not nearly as intense as the one observed without the mix, appeared as shown in Figure 33A through a neutral density filter and is shown in Figure 33B as seen through a red filter. It is apparent from these shots that the edge of the cathode orifice and the spot at the bottom of the insert near the orifice plate were both hot and therefore radiating in the red. Oscillations in both the discharge characteristics and in the light intensity within the cathode were observed during the time when these photographs were made. After roughly fifteen minutes of running time and a shutdown-restart cycle, this spot gradually disappeared and the discharge took the color, intensity and characteristics of a cathode with an insert that had been completely covered with emissive mix. Figure 33C is a photograph taken through a neutral density filter of such a cathode.

At no time was a spot observed, either stationary or moving, in a cathode which employed an insert coated completely with emissive mix. This does not positively preclude the existence of a moving spot since the streak photograph was not used at speeds beyond 1500 inches/sec but the spot would have either had to be moving at speeds beyond about 6000 inches/sec or be moving over very small distances in order to escape

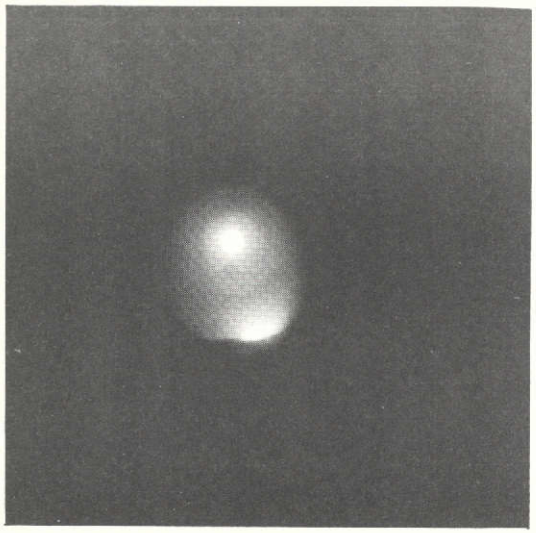

A. R-500 ADDED – NEUT. DENSITY FILTER

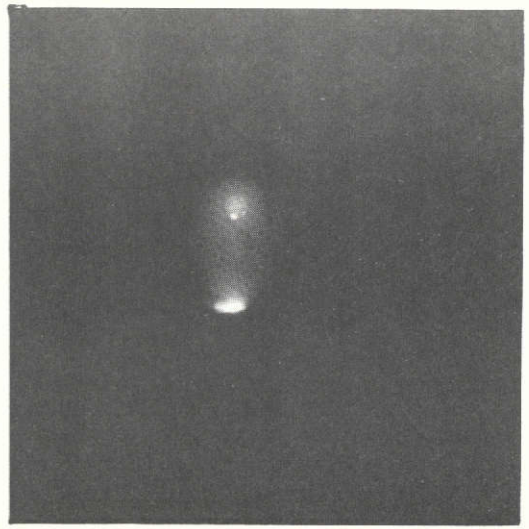

B. R-500 ADDED – RED FILTER

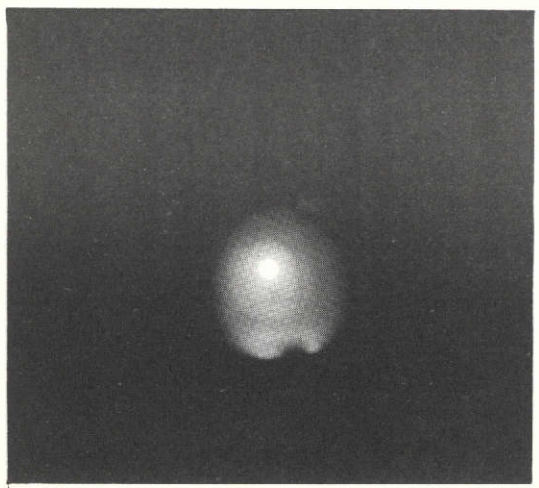

C. AFTER 15 min OPERATION WITH R-500 – NEUT. DENSITY FILTER

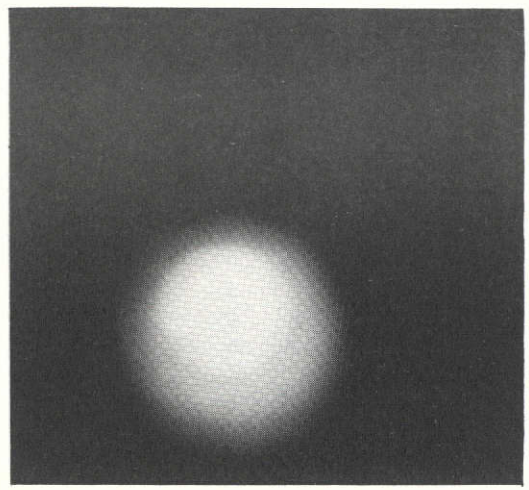

D. POROURS TUNGSTEN R – 500 IMPREGNATED INSERT – NEUT. DENSITY FILTER

HOLLOW CATHODE WITH R-500 DURING OPERATION

FIGURE 33

detection. Photographs taken through a red filter of cathodes treated with emissive mix showed a uniform region of red radiation on the forward edge of the insert and the orifice plate. Such a photograph suggests this is a region of rather uniform temperature.

An additional experiment was conducted using a porous tungsten insert impregnated with emissive mix. Figure 33D shows a photograph of a cathode operating with such an insert. The light radiated from this discharge was similar in color and intensity to that of the emissive mix coated rolled foil insert but it appeared to be more diffuse and uniform over the entire insert. At no time was a spot, either moving or stationary, observed in a cathode utilizing a porous tungsten insert.

Conclusions

The cathode spot is an important electron emission mechanism in a cathode free from low work-function alkaline-earth coatings. Metal surfaces in the cathode and on its insert are hottest at the location of a spot of intense radiation which seems to attach itself to some metal protuberance in the chamber. Cathode spots are not observed in cathodes where adequate emissive mix is applied but a spot might be present in a cathode which has had a large percentage of its emissive mix coating depleted. If this is in fact the case, one might expect to see a discontinuity in the temperature and discharge and keeper characteristics when the spot mechanism appeared. Oxide coatings do appear to migrate within the cathode during operation.

## ADDITIONAL STUDIES

### Thermal Flow Meter

The thermal flow meter[4,10] is a device which can be used to indicate continuously the very low mercury flow rates associated with ion thruster operation. This device was used throughout the report period on the modified SERT II thruster and it proved to be a valuable tool for showing flow rate trends. The main problem with the device has been its tendency to drift with ambient temperature, but it was believed that this could be corrected by using matched thermistors as sensors in the device. Testing revealed that matched thermistors did not correct this tendency to drift.

### Ion Beam Plasma Studies

The ion beam of an operating mecury bombardment thruster was monitored using a Langmuir probe rake. This probe rake was composed of nine cylindrical probes each having a diameter of 0.074 cm and a length of 0.76 cm, and it could be swept through the ion beam during thruster operation. Preliminary analysis showed the plasma sheath around a probe in the ion beam was large compared to the probe diameter and suggested the plasma might contain both monoenergetic and Maxwellian electron groups. This necessitated the development of the thick sheath Langmuir probe analysis presented as Appendix B. Typical Langmuir probe data were collected from 72 locations on a plane 3.2 cm downstream of the thruster accel grid of the modified SERT II thruster operating at a 590 mA beam current. The neutralizer was biased 25 V below tank ground and the screen and accel grid potentials were +1 kV, -0.5 kV respectively. These traces were analyzed using the procedure of Appendix B and the results are presented in the form of constant property lines in Figure 34. The outline of the neutralizer and the beam circumference at the accel grid are indicated on these figures.

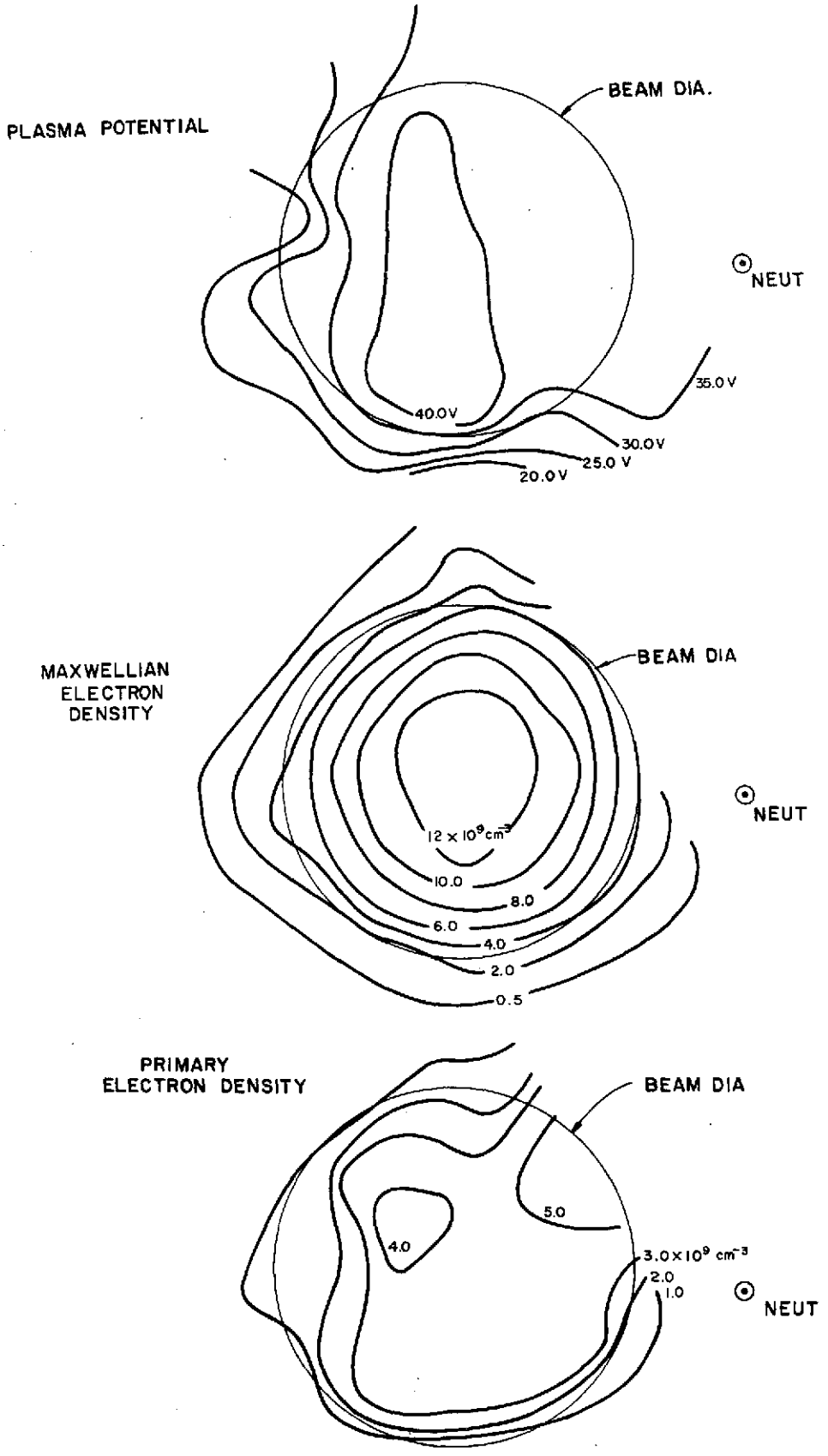


CONSTANT PROPERTY PROFILES IN AN ION BEAM - 3.2 cm DOWNSTREAM OF GRIDS
FIGURE 34

# APPENDIX A

## A NUMERICAL PROCEDURE FOR ANALYZING LANGMUIR PROBE DATA

John R. Beattie

### Nomenclature

$A$ = probe collection area, $m^2$

$B_1$ = primary electron current intercept, A

$B_2$ = primary electron current slope, $AV^{-1}$

$B_3$ = $I_{sat} \exp(-V_p/T_e)$, A

$B_4$ = $1/T_e$, $eV^{-1}$

$B_i^o$ = initial estimates of the parameters $B_i (i=1,4)$

$i_p$ = primary electron current at plasma potential, A

$I$ = probe electron current, A

$I_{sat}$ = Maxwellian electron saturation current, A

$m_e$ = electron mass, kg

$n_m$ = Maxwellian electron number density, $m^{-3}$

$n_p$ = primary electron number density, $m^{-3}$

$q$ = electronic charge, C

$T_e$ = Maxwellian electron temperature, eV

$V$ = probe potential relative to cathode potential, V

$V_p$ = plasma potential relative to cathode potential, V

$\delta B_i$ = corrections to the estimates of the parameters $B_i (i=1,4)$

$\xi_p$ = primary electron energy, eV

Introduction

The analysis of Langmuir probe data obtained in electron bombardment ion thrusters which use mercury as the propellant is complicated by the presence of two distinct groups of plasma electrons. One group has a Maxwellian energy distribution function with a temperature of approximately 5 eV, and the other group has an isotropic monoenergetic distribution function with an energy of approximately 30 eV. This latter group is sometimes referred to as a "primary" electron group. Although the two-group theory is only an approximation, it does have a physical basis and has been verified by experiment[20,21].

If the plasma contains only Maxwellian electrons the analysis of Langmuir probe data is straightforward since the current to an infinite planar probe varies exponentially with probe voltage in the retarding field region (probe voltage less than plasma potential), and remains constant in the accelerating field region (probe voltage greater than plasma potential). In reality there is a slight variation in probe current with probe voltage beyond the plasma potential and this phenomenon is attributed to an increase in the dimensions of the plasma sheath surrounding the probe. The graphical procedure used in analyzing probe data when only Maxwellian electrons are present in the plasma consists of plotting the logarithm of the probe current as a function of probe voltage. This results in a curve which can be approximated by two straight line segments which intersect at the plasma potential. The slope of the straight line approximation in the retarding field region determines the electron temperature and the current at the intersection of the two straight lines gives the electron number density.

If the plasma contains both primary and Maxwellian electrons, the logarithm of the probe current is no longer a linear function of the probe voltage and the analysis becomes much more difficult. A graphical method[20] for analyzing this type of trace has been devised and is based on the existence of a linear segment of the current-voltage curve in the retarding field region of the trace. However, the current-voltage curves are in some cases far from linear in the retarding field region and this nonlinearity is the major source of error when applying the graphical analysis technique. Figure A1 is a plot of electron current versus probe

voltage for a two-group plasma having properties typical of an ion thruster. The curve was generated using analytical expressions for the variation of primary and Maxwellian electron current as a function of probe potential and is presented to illustrate the absence of a well defined linear portion of the trace even when the two-group assumption is satisfied. Actual probe data exhibit a smooth region near the plasma potential (shown as a broken line in Figure A1) which is attributed to the existence of electrical noise in the discharge chamber.

Theory

The assumption that the plasma contains two distinct groups of electrons enables one to express the electron current to a Langmuir probe as the sum of two currents. The current due to primary electrons varies linearly with probe voltage for an infinite planar probe. The other current, due to Maxwellian plasma electrons, varies exponentially with probe voltage in the retarding field region. Hence, the current to the probe in the retarding field region of the trace can be written as

$$I = B_1 + B_2V + B_3 \exp(B_4V) \qquad (A1)$$

Given a set of data pairs (I,V) which have been measured using a Langmuir probe, the plasma properties can be calculated in a straightforward manner if the unknown coefficients $B_i(i=1,4)$ can be determined by a curve fitting technique. Note, however, that the functional relationship for the current is non-linear in the parameters $B_i$. In this type of problem the standard linear least squares method is not applicable and one must apply a non-linear method.

Procedure

The procedure used to determine the unknown coefficients $B_i$ is known as a least-squares differential-correction technique[22]. The method requires the user to provide reasonable initial estimates of the coefficients $B_i$. These estimates result in a set of linear algebraic equations the solution of which yields the first order corrections $\delta B_i$ to the initial estimates of the parameters $B_i$. If the absolute value of any of these corrections is larger than some specified value, the

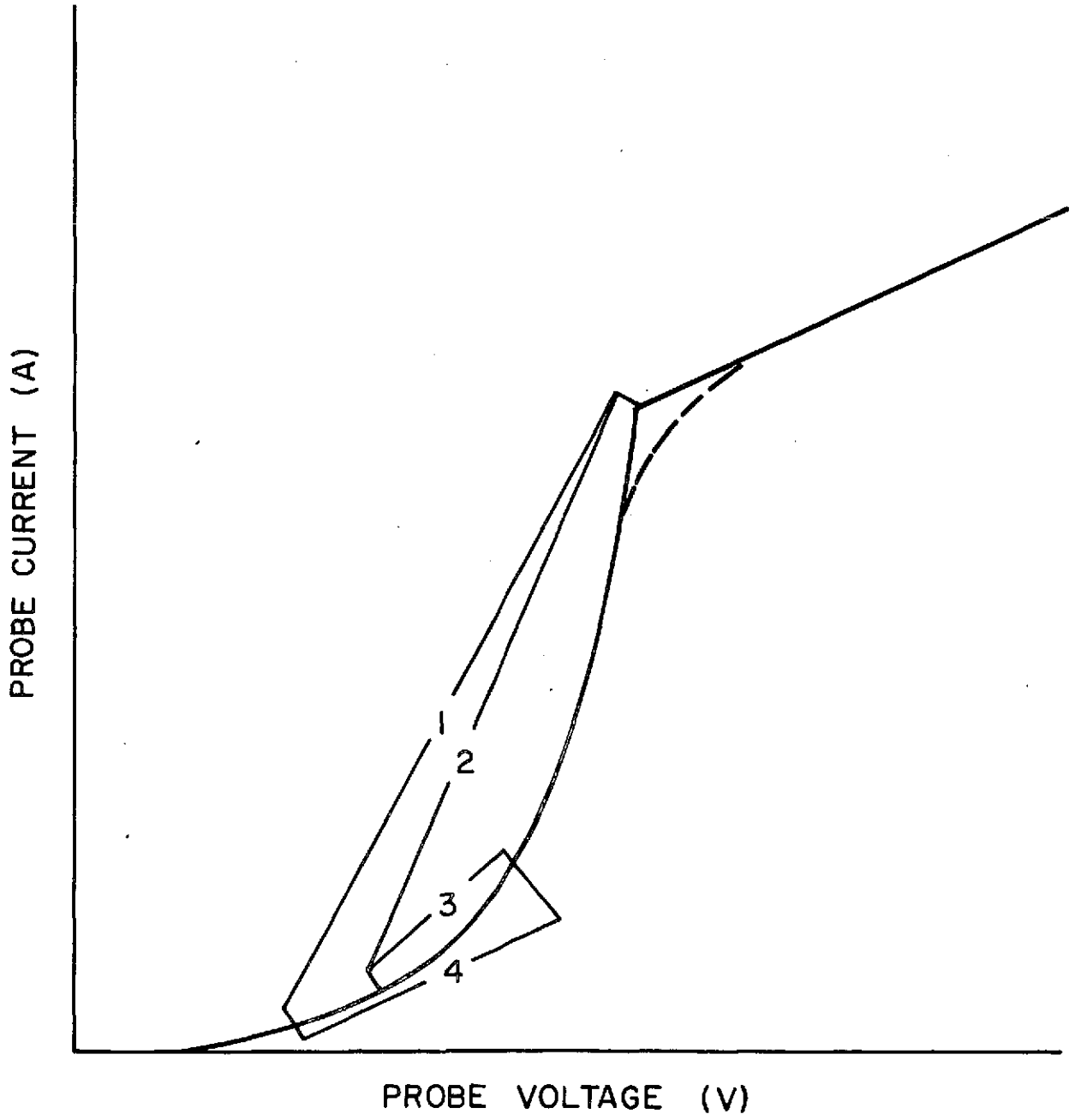


ANALYTICALLY GENERATED LANGMUIR PROBE TRACE ASSUMING A TWO-GROUP PLASMA

FIGURE A1

initial estimates $B_i^o$ are replaced by the quantity $B_i^o + \delta B_i$ and the procedure repeated.

As one might expect, convergence of the differential-correction technique depends on how closely the initial estimates $B_i^o$ approximate the actual values of the parameters $B_i$. Note, however, that for this particular problem if the parameter $B_4$ is known then the function becomes linear in the remaining unknown parameters $B_i(i=1,3)$ which can be determined by the method of linear least squares. This is important since one can provide a very reasonable estimate of the unknown parameter $B_4$ (the reciprocal of the Maxwellian electron temperature which for a mercury plasma would be expected to be around 5 eV). With this initial estimate the method of linear least squares can be used to find the remaining initial estimates of the parameters $B_i(i=1,3)$ for the differential-correction technique.

The procedure described above uses only the data in the retarding field region of the probe trace. Since the primary electron current must be positive, the minimum probe voltage for which Equation (A1) is valid is given by

$$V = -B_1/B_2 \quad . \tag{A2}$$

For each probe voltage which is greater than this value, the Maxwellian current is found by subtracting the quantity $B_1 + B_2V$ from the total current. The logarithm of this current (Maxwellian electron current) is a linear function of probe voltage, and a linear least squares fit of these data in both regions of the probe trace yields the equations of the straight line segments. Equating these expressions yields the plasma potential and electron saturation current. Finally, the number densities and primary electron energy are calculated from the expressions

$$n_m = \left(\frac{2\pi m_e}{qT_e}\right)^{1/2} \frac{I_{sat}}{Aq} \quad , \tag{A3}$$

$$n_p = \left(\frac{8m_e}{\xi_p q}\right)^{1/2} \frac{i_p}{Aq} \quad , \tag{A4}$$

$$\xi_p = V_p + B_1/B_2 \quad . \tag{A5}$$

Since the slope of the logarithm of the Maxwellian current in the retarding field region of the probe trace is the reciprocal of the electron temperature, this value can be compared to the parameter $B_4$ calculated by the differential-correction technique. These values should agree and the comparison can be used as an indication of the accuracy of the method.

With all the plasma properties determined, the probe current can be calculated as a function of probe voltage by use of Equation A1. These data can be compared to the measured values and an error computed. This error can then be used as an indication of how accurately the plasma properties have been determined and also how well the two-group assumption is satisfied.

Results

The procedure described above was programmed in the Fortran IV language. Data pairs were calculated by use of Equation (A1) and these data used as input to the computer routine. Based on these analytic input data the following results were obtained:

1. When the iteration technique converges, the results are exact, unique, and independent of the initial estimate of electron temperature.
2. Convergence appears to be fastest when the initial estimate of the electron temperature is high rather than low. However, an estimate which is greater than twice the actual electron temperature may not result in convergence.
3. The results are independent of the region of the curve used as input. Input data at one volt increments from each of the regions indicated in Figure A1 gave exact results.
4. Over a reasonable region of the curve the results are independent of the number of data pairs input. That is, the results for regions 1 and 2 in Figure A1 were exact when the voltage increment was increased to 5 volts.

Experimental Langmuir probe data are usually recorded by an x-y plotter and these graphical results must be digitized for subsequent

input to the computer routine. In order to estimate the error which can be expected as a result of the conversion from graphical to digital form, the curve of Figure A1 was generated by a digital computer and plotted by use of a digital incremental plotter. The curve was then digitized by use of an optical data digitizer and these data were used as input to the routine. The results of this investigation are presented in Table A1 which shows the percent error for each plasma property as a function of the region of the curve used for input and the probe voltage increment. Based on these results it appears that input data

TABLE A1. PLASMA PROPERTY ERRORS DUE TO CONVERSION OF CURRENT-VOLTAGE DATA FROM GRAPHICAL TO DIGITAL FORM

| Region | Voltage Increment (V) | Plasma Property Error (%) | | | | |
|---|---|---|---|---|---|---|
| | | $T_e$ | $V_p$ | $\xi_p$ - | $n_p$ | $n_m$ |
| 1 | 1 | 2.5 | 0.5 | 1.9 | 12.0 | 0.7 |
| 2 | 1 | 1.7 | 0.5 | 1.0 | 5.8 | 0.1 |
| 3 | 1 | 18.0 | 1.8 | 10.6 | 70.5 | 1.0 |
| 4 | 1 | 1.8 | 0.2 | 2.1 | 15.2 | 1.3 |
| 1 | 5 | 2.8 | 0.4 | 2.6 | 17.1 | 1.1 |

should be taken over a 20-25 V range (Region 1 or 2) and the voltage increment should be around 1 V. One can then expect the error in all the plasma properties except primary electron density to be less than 5%. The error in primary electron density can be expected to be around 10%. A more sophisticated data acquisition system which would perform the analog to digital conversion directly should almost completely eliminate the graphical conversion error discussed above.

Several Langmuir probe traces obtained from an operating ion thruster were analyzed by both the graphical procedure[20] and the numerical procedure outlined above. In the analysis the ion current to the probe was considered negligible and the probe current assumed to be electron current only. Comparison of the plasma properties determined by these methods indicated good agreement for the plasma potential and Maxwellian number density. Poor agreement was observed for the Maxwellian electron

temperature and primary electron energy and density. The numerical procedure determined electron temperatures and energies which are more consistent with expected values than those determined graphically. For example, on the thruster centerline the numerical procedure resulted in an average Maxwellian electron temperature and primary electron energy of 4.1 eV and 32 eV, respectively. The corresponding graphically determined averages were 2.4 eV and 16.2 eV. The Maxwellian electron temperature expected to exist in mercury bombardment thrusters is about 4-5 eV while the primary electrons would be expected to have an energy in the 30-35 eV range when operating at a 37 V anode potential.

# APPENDIX B

## THICK SHEATH LANGMUIR PROBE ANALYSIS

Gerald Isaacson

Nomenclature List

$S$ = slope ($A^2/V$)

$A$ = probe area ($m^2$)

$q$ = electronic charge (coulomb)

$m_e$ = electron mass (kg)

$n_e$ = total electron number density ($m^{-3}$)

$n_m$ = Maxwellian electron number density ($m^{-3}$)

$n_p$ = primary electron number density ($m^{-3}$)

$i_{sat}$ = Maxwellian electron saturation current (A)

$i_p$ = primary electron saturation current (A)

$\xi_p$ = primary electron energy (eV)

$T_e$ = electron temperature (eV)

$V$ = probe potential relative to tank ground (V)

$V_p$ = plasma potential relative to tank ground (V)

The method presently used to analyze data from a Langmuir probe, operating in the thick sheath mode, involves considering two regions of the current-voltage characteristic of the probe. In one region an electron encounters a retarding electric field (probe voltage < plasma potential) and in the other it encounters an accelerating electric field (probe voltage > plasma potential).

Retarding Field Portion of Curve

It has been determined that the current to a probe in a retarding field is independent of the dimensions of the sheath[23]. Therefore, this portion of the trace can be analyzed using thin sheath methods. These methods are explained in detail by Strickfaden and Geiler[20] and will only be described briefly here. The plasma property that can be obtained from this portion of the trace is the temperature of the Maxwellian electrons. Since the total current to the probe is the sum of both primary and Maxwellian electron currents, the primary contribution must be subtracted off before this property can be obtained. If the primary electrons are assumed to be monoenergetic their contribution to probe current will increase linearly with probe potential.

Figure B1 shows a typical Langmuir probe trace (dashed line). In order to aid in determining the location of the most nearly linear portion of the trace it is also recorded with the current sensitivity increased by a factor of ten (dotted line). Using this expanded trace, line A-B is drawn tangent to the most nearly linear portion and extended downward until it intersects the zero current axis at B. The second line, C-D, is then drawn through point B tangent to the original trace. The difference between line C-D and the probe trace at a given probe voltage represents the current due to the Maxwellian electrons at that voltage. The logarithm of this current due to Maxwellian electrons is plotted as a function of probe voltage as shown in Figure B2. Since only the Maxwellian electron temperature is to be obtained from this graph, the plot need only be extended to the point where it begins to deviate from a straight line. A line is then drawn through the linear portion of this plot, as indicated by line G-H in Figure B2, and the electron temperature is determined from its slope by using:[20]

$$T_e = \frac{V(10\ I) - V(I)}{2.3} \qquad (B1)$$

where the numerator represents the voltage change over a decade change in current.

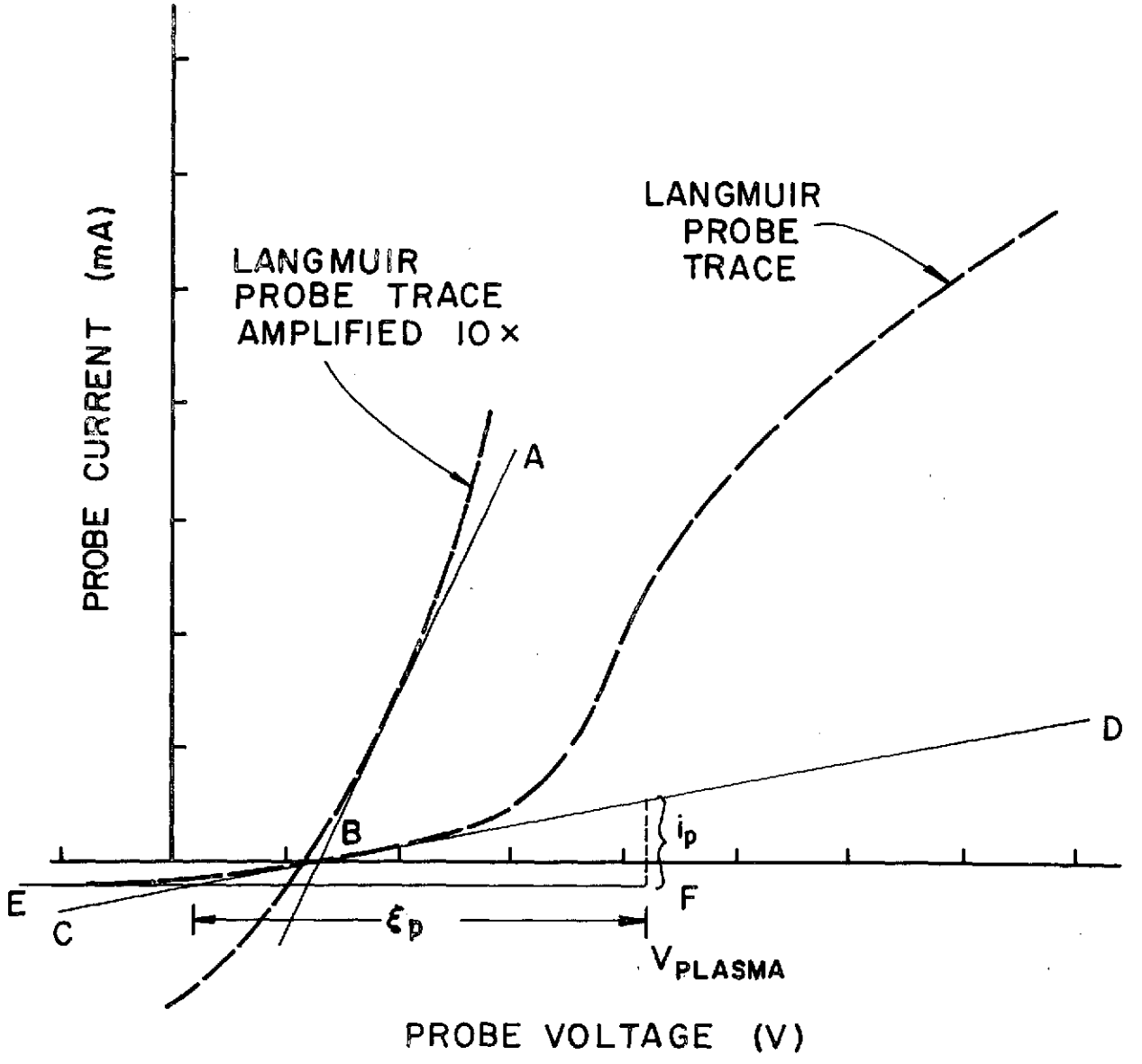


LANGMUIR PROBE TRACE WITH CONSTRUCTION LINES

FIGURE B1

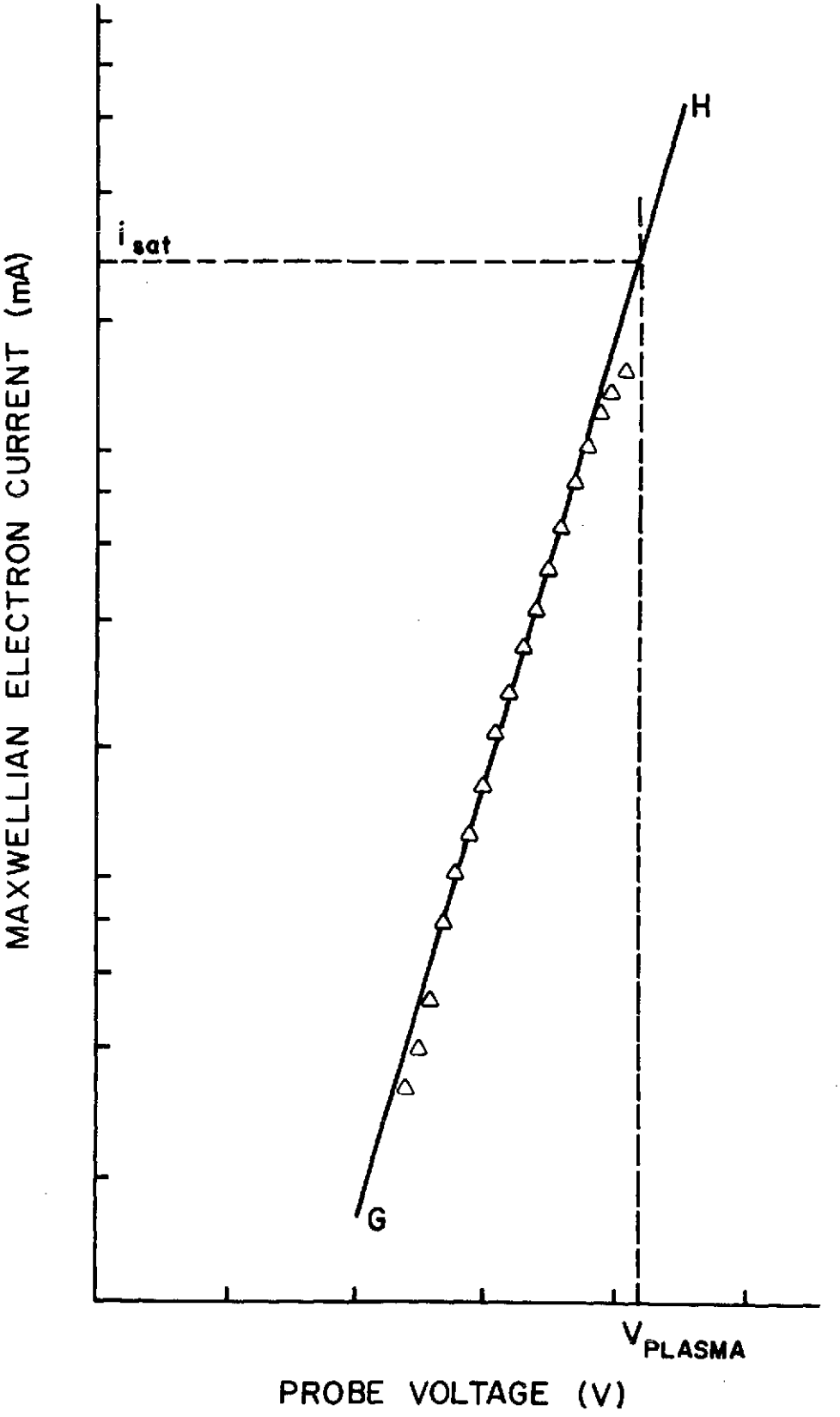


LOG OF MAXWELLIAN ELECTRON CURRENT VRS. PROBE VOLTAGE

FIGURE B2

Accelerating Field Portion of Curve

For the accelerating field portion of the Langmuir probe trace, the probe current is no longer independent of the sheath dimensions. However, Chen[24] points out that for cylindrical probes the current due to both primary and Maxwellian electrons varies as the square root of probe potential. Because of this similar variation with probe potential primary and Maxwellian electron densities cannot be separated in this region. In a plot of probe current squared vs probe voltage (Figure B3) there should be a linear segment that has a slope which is related to total electron density by the equation:[24]

$$n_e = \left( \frac{S\ \pi^2 m_e}{2\ A^2\ q^3} \right)^{1/2} . \qquad \text{(B2)}$$

Since this plot is valid only for the accelerating field region, points below a voltage estimated to be less than plasma potential may be omitted.

Concluding Analysis

Once the electron temperature and the total electron density are known, the remaining properties are determined by trial and error. This is done by first choosing a value for the plasma potential. The Maxwellian electron saturation current ($i_{sat}$) is then obtained from the semi-log plot (Figure B2) as the current at which line G-H intersects the assumed plasma potential. Knowing the Maxwellian electron saturation current and the Maxwellian electron temperature, the density of the Maxwellian electrons can now be found from:[20]

$$n_m = \frac{i_{sat}}{Aq\ (qT_e/2\pi m_e)^{1/2}} . \qquad \text{(B3)}$$

Returning to the Langmuir probe trace (Figure B1) line E-F is drawn tangent to the horizontal portion of the ion current trace, and is extended to the assumed plasma potential. The vertical displacement of this line corresponds to the value of the ion saturation current. The primary electron saturation current ($i_p$) is then equal to the difference

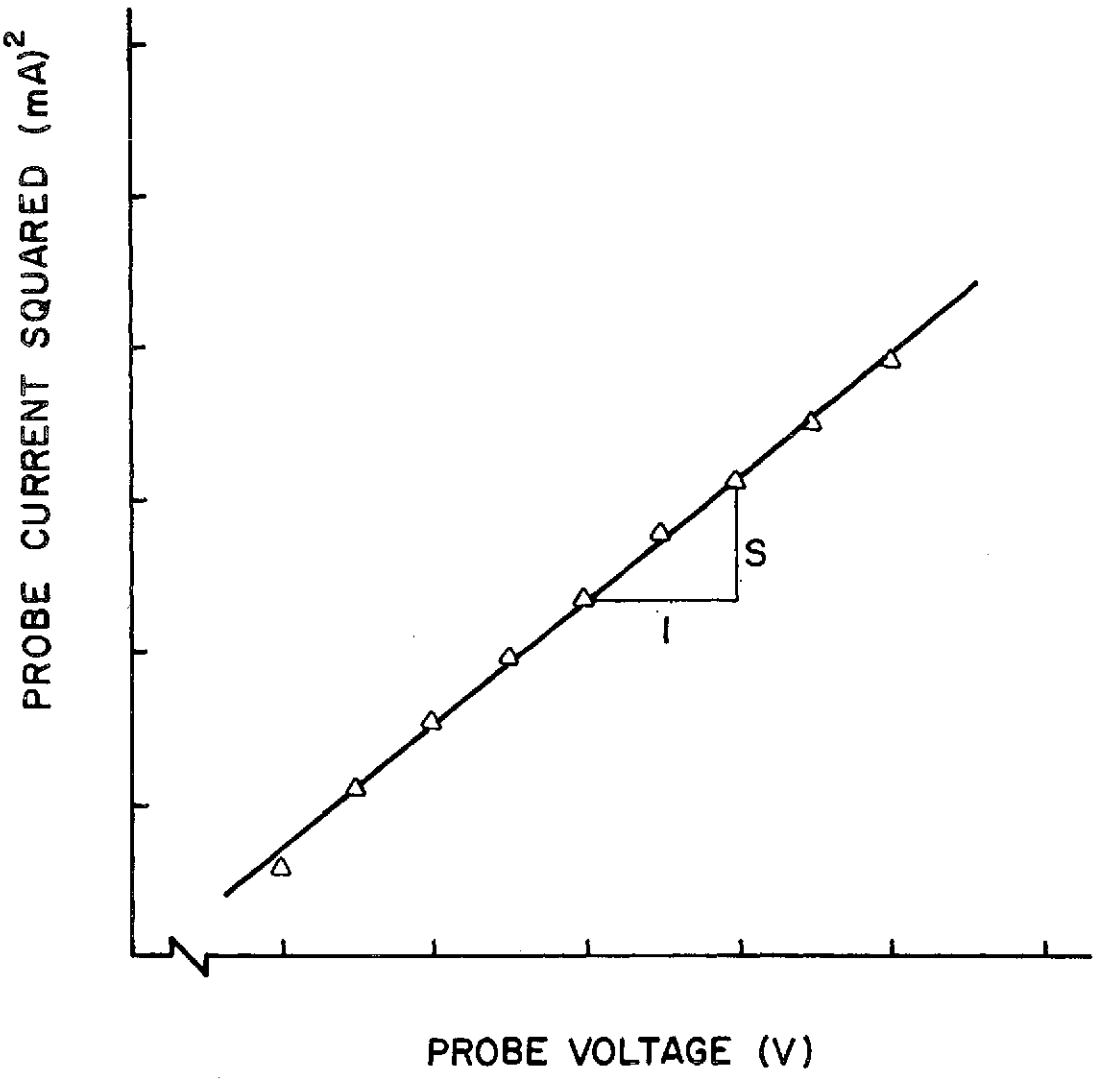


PROBE CURRENT SQUARED VRS. VOLTAGE (ACCELERATING FIELD REGION)
FIGURE B3

between the ion saturation current line and the primary electron current line at plasma potential. Also, the primary electron energy ($\xi_p$) is defined as the difference in voltage between the intersection of lines C-D and E-F and the plasma potential. The number density of the primary electrons is determined from[20]

$$n_p = \frac{4\, i_p}{Aq(2q\xi_p/m_e)^{1/2}} \qquad \text{(B4)}$$

The two electron densities ($n_p$ and $n_m$ which have just been calculated) are then added together and compared with the total electron density obtained previously. If the sum and the total densities are not in agreement, a new value for the plasma potential is selected and the procedure is repeated until they do agree. The values used in the final calculation, along with the electron temperature, are then taken to be the plasma properties.

## REFERENCES


1. Free, B. A., "Economic Tradeoff Studies for Electric Propulsion Missions on Communications Satellites," AIAA Paper No. 71-683, June 14-18, 1971.

2. Wintucky, E. G., "High Voltage Ignition of Mercury Discharge Hollow Cathodes," AIAA Paper No. 73-1140, Oct. 31 - Nov. 2, 1973.

3. Anon., "8-cm Mercury Ion Thruster System Technology," NASA TMX-71611, October 21-23, 1974.

4. Wilbur, P. J., "Hollow Cathode Restartable 15 cm Diameter Ion Thruster," NASA CR-134532, December 1973.

5. Kerslake, W. R. and R. C. Finke, "SERT II Hollow Cathode Multiple Restarts in Space," AIAA Paper No. 73-1136, Oct. 31 - Nov. 2, 1973.

6. Wilbur, P. J., "Correlation of Ion and Beam Current Densities in Kaufman Thrusters," Journal of Spacecraft and Rockets, Vol. 10, No. 9, September 1973, pp. 623-624.

7. Knauer, W., R. L. Poeschel, and J. W. Ward, "The Radial Field Kaufman Thruster," Journal of Spacecraft and Rockets, Vol. 7, No. 3, March 1970, pp. 248-251.

8. King, H. J., et al., "2 1/2 KW Low Specific Impulse, Hollow Cathode Mercury Thruster," AIAA Paper No. 69-300, March 3-5, 1969.

9. Poeschel, R. L. and W. Knauer, "A Variable Magnetic Baffle for Hollow Cathode Thrusters," AIAA Paper No. 70-175, Jan. 19-20, 1970.

10. Wilbur, P. J., "Experimental Investigation of a Throttlable 15 cm Hollow Cathode Ion Thruster," CR-121038, December 1972, NASA.

11. Kieffer, L. J., "Electron Impact Ionization Cross Section Data for Atoms, Atomic Ions, and Diatomic Molecules," Rev. Mod. Physics, Vol. 38, No. 1, pp. 15, 23, 1966.

12. McConnell, J. C., and Moiseiwitsch, B. L., "Excitation of Mercury by Electrons," J. Phys. B. Vol. 1, No. 3, pp. 409-412.

13. Gryzinski, Michal, "Classical Theory of Atomic Collisions. I. Theory of Inelastic Collision," Phys. Rev. Vol. 138, No. 2A, p. A341, April 19, 1965

14. Shpenik, O. B. and Azpesochnyi, I. P., "Excitation Cross Sections near the Threshold for Electron Atom Collisions," Optics and Spect. Vol. 23, pp. 7-10, 1967.

15. Masek, T. D., "Plasma Properties and Performance of Mercury Ion Thrusters," AIAA Paper No. 69-256, March 3-5, 1969.

16. Mitchell, A. C. G., "Resonance Radiation and Excited Atoms," Cambridge at the University Press, 1961.

17. Kupriyanov, S. E. and Z. Z. Latypov, "Ionization of Positive Ions by Electrons," Soviet Physics JETP, Vol. 19, No. 3, pp. 558-559, Sept. 1964.

18. Plumlee, R. H. and L. P. Smith, "Mass Spectroscopic Study of Solids I. Preliminary Study of Sublimation Characteristics of Oxide Cathode Materials," Journal of Applied Physics, Vol. 21, pp. 811-819, Aug. 1950.

19. Zuccaro, D., "Mercury Vapor Hollow Cathode Component Studies," AIAA Paper No. 73-1141, Oct. 31 - Nov 2, 1973.

20. Strickfaden, W. B. and K. L. Geiler, "Probe Measurements of Discharge in an Operating Electron Bombardment Engine," AIAA Journal, Vol. 1, No. 8, August, 1963, pp. 1815-1823.

21. Martin, A. R., "Electron Energy Distributions in an Ion Engine Discharge," Journal of Spacecraft and Rockets, Vol. 8, No. 5, May 1971, pp. 548-550.

22. McCalla, T. R., "Introduction to Numerical Methods and Fortran Programming," Wiley, New York, 1967, pp. 255-260.

23. Schott, L., Plasma Diagnostics, W. Lochte-Holtgreven, Editor, North-Holland Publishing Co., Amsterdam, 1968, Chapter 11.

24. Chen, F. F., Plasma Diagnostic Techniques, Huddlestone and Leonard, Editors, Academic Press, New York, 1965, Chapter 4.

DISTRIBUTION LIST

| | Number of Copies |
|---|---|
| National Aeronautics and Space Administration<br>Washington, D. C. 20546 | |
| Attn: RPE/Mr. James Lazar | 1 |
| Mr. Daniel H. Herman, Code SL | 1 |
| National Aeronautics and Space Administration<br>Lewis Research Center<br>21000 Brookpark Road<br>Cleveland, Ohio 44135 | |
| Attn: Research Support Procurement Section | |
| Ms. S. L. Boyer, MS 500-312 | 1 |
| Technology Utilization Office, MS 3-19 | 1 |
| Report Control Office, MS 5-5 | 1 |
| Library, MS 60-3 | 2 |
| N. T. Musial, MS 500-113 | 1 |
| Spacecraft Technology Division, MS 54-1 | |
| Mr. W. Plohr | 1 |
| Mr. E. Davison | 1 |
| Mr. R. Finke | 1 |
| Mr. D. Byers | 1 |
| Mr. B. Banks | 1 |
| Mr. P. Thollot | 1 |
| Mr. W. Kerslake | 10 |
| Physical Science Division, MS 301-1 | |
| Mr. W. E. Moeckel | 1 |
| National Aeronautics and Space Administration<br>Marshall Space Flight Center<br>Huntsville, Alabama 35812 | |
| Attn: Mr. Ernst Stuhlinger (M-RP-DIR) | 1 |
| Mr. C. H. Guttman | 1 |
| Research and Technology Division<br>Wright-Patterson AFB, Ohio 45433 | |
| Attn: (ADTN) Lt. David A. Fromme | 1 |
| National Aeronautics and Space Administration<br>Scientific and Technical Information Facility<br>P. O. Box 33<br>College Park, Maryland 20740 | |
| Attention: MASA Representative RQT-2448 | 40 |
| Case Western Reserve University<br>10900 Euclid Avenue<br>Cleveland, Ohio 44106 | |
| Attn: Dr. Eli Reshotko | 1 |

Grumman Aircraft Engineering Corporation
Bethpage, Long Island, New York 11101
Attn: Mr. L. Rothenberg 1

Royal Aircraft Establishment
Space Department
Farnborough, Hants, England
Attn: Dr. D. G. Fearn 1

United Kingdom Atomic Energy Authority
Culham Laboratory
Abingdon, Berkshire, England
Attn: Dr. P. J. Harbour 1
Dr. M. F. A. Harrison 1

National Aeronautics and Space Administration
Goddard Space Flight Center
Greenbelt, Maryland 20771
Attn: Mr. W. Isley, Code 734 1
Mr. R. Hunter 1
Mr. R. Callens, Code 734 1

SAMSO
Air Force Unit Post Office
Los Angeles, California 90045
Attn: Capt. D. Teal/SYAX 1

Comsat Laboratories
P. O. Box 115
Clarksburg, Maryland 20734
Attn: Mr. B. Free 1
Mr. O. Revesz 1

Rocket Propulsion Laboratory
Edwards AFB, California 93523
Attn: LKDA/Mr. Frank Mead 2

DFVLR - Institut für Plasmadynamik
Technische Universitat Stuttgart
7 Stuttgart-Vaihingen
Allmandstr 124
West Germany
Attn: Dr. G. F. Au 1
Mr. H. Bessling 1

Giessen University
1st Institute of Physics
Giessen, West Germany
Attn: Professor H. W. Loeb 1

Jet Propulsion Laboratory
4800 Oak Grove Drive
Pasadena, California 91102
Attn: Dr. Kenneth Atkins 1
Technical Library 1
Mr. James Graf 1

Electro-Optical Systems, Inc.
300 North Halstead
Pasadena, California 91107
Attn: Mr. R. Worlock 1
Mr. E. James 1

TRW Inc.
TRW Systems
One Space Park
Redondo Beach, California 90278
Attn: Mr. M. Huberman 1
Dr. J. M. Sellen 1

National Aeronautics and Space Administration
Ames Research Center
Moffett Field, California 94035
Attn: Technical Library 1

National Aeronautics and Space Administration
Langley Research Center
Langley Field Station
Hampton, Virginia 23365
Attn: Technical Library 1

Hughes Research Laboratories
3011 Malibu Canyon Road
Malibu, California 90265
Attn: Mr. J. H. Molitor 1
Mr. T. D. Masek 2
Dr. R. L. Poeschel 1
Mr. R. Vahrenkamp 1

United States Air Force
Office of Scientific Research
Washington, D. C. 20025
Attn: Mr. M. Slawsky 1

Air Force Academy, Colorado 80840
Attn: Major N. Roderick 1

Princeton University
Princeton, New Jersey 08540
Attn: Mr. W. F. Von Jaskowsky 1
Dean R. G. Jahn 1
Dr. K. E. Clark 1

The City University
Department of Aeronautics
St. John Street
London ECIV 4PB, England
Attn: Dr. Antony Martin 1

Communications Research Centre
Ottawa, Ontario, Canada
Attn: Dr. W. F. Payne 1

Joint Institute for Laboratory Astrophysics
University of Colorado
Boulder, Colorado 80302
Attn: Dr. Gordon H. Dunn 1

North American Rockwell
Advanced Prog. Div. of Space Division
12214 Lakewood Boulevard
Downey, California 90241
Attn: Dr. Robert H. Stivers 1

Advanced Rocket Technology
17821 Sky Park Circle, P. O. Box 4505
Irvine, California 92664
Attn: Mr. Russell J. Page 1

Department of Aeronautics and Astronautics
Stanford University
Stanford, California 94305
Attn: Professor Howard S. Seifert 1

McDonnell Douglas Corporation
St. Louis, Missouri 63166
Attn: Mr. Milton Goodman
Building 106, Level 3, Dept. 243 1

Boeing Aerospace Co.
P. O. Box 3999
Seattle, Washington 98124
Attn: Mr. Donald Grim 1

Intelcom Rad Tech
7650 Convoy Court
P. O. Box 80817
San Diego, California 92138
Attn: Dr. David Vroom 1

Lockheed Missiles and Space Co.
Sunnyvale, California 94088
Attn: Dr. William L. Owens
Propulsion Systems, Dept. 62-13 1

Fairchild Republic Co.
Farmingdale, New York 11735
Attn: Dr. William Guman 1

COMSAT Corporation
950 L'Enfant Plaza SW
Washington, D. C. 20024
Attn: Mr. Sidney O. Metzger 1

Electrotechnical Laboratory
Tanashi Branch
5-4-1 Mukodai-Machi, Tanashi-Shi
Tokyo, Japan
Attn: Dr. Katsuva Nakayama 1

Office of Assistant for Study Support
Kirtland Air Force Base
Albuquerque, New Mexico 87117
Attn: Dr. Calvin W. Thomas OAS GE 1
Dr. Gerhart Eber OAS GE 1